Interface Electronic State Characterization of Dielectrics on Diamond and C-BN

by

Yu Yang

A Dissertation Presented in Partial Fulfillment
of the Requirements for the Degree
Doctor of Philosophy

Approved April 2018 by the
Graduate Supervisory Committee:

Robert Nemanich, Chair
Martha McCartney
Fernando Ponce
Quan Qing

ARIZONA STATE UNIVERSITY

May 2018

ABSTRACT

Diamond and cubic boron nitride (c-BN) are ultra wide band gap semiconductors (Eg>3.4 eV) and share similar properties in various aspects, including being isoelectronic, a 1% lattice mismatch, large band gap, high thermal conductivity. Particularly, the negative electron affinity (NEA) of diamond and c-BN is an unusual property that has led to effects such as p-type surface conductivity, low temperature thermionic emission, and photon enhanced thermionic emission. In this dissertation, the interface chemistry and electronic structure of dielectrics on diamond and c-BN are investigated with X-ray and ultraviolet photoemission spectroscopy (XPS and UPS). The first study established that the surface conductive states could be established for thin Al_2O_3 on diamond using a post deposition H-plasma process. At each step of the atomic layer deposition (ALD) and plasma processing, the band alignment was characterized by *in situ* photoemission and related to interface charges. An interface layer between the diamond and dielectric layer was proposed to explain the surface conductivity. The second study further investigated the improvement of the hole mobility of surface conductive diamond. A thin layer of Al_2O_3 was employed as an interfacial layer between surface conductive hydrogen-terminated (H-terminated) diamond and MoO_3 to increase the distance between the hole accumulation layer in diamond and negatively charged states in acceptor layer. With an interfacial layer, the ionic scattering, which was considered to limit the hole mobility, was reduced. By combining two oxides (Al_2O_3 and MoO_3), the hole mobility and concentration were modulated by altering the thickness of the Al_2O_3 interfacial layer. The third study focused on the electronic structure of vanadium-oxide-terminated c-BN surfaces. The vanadium-oxide-termination was formed on c-BN by combining vanadium

deposition using molecular beam deposition (MBD) and oxygen plasma treatment. After thermal annealing, a thermally stable NEA was achieved on c-BN. A model was proposed based on the deduced interface charge distribution to explain the establishment of an NEA.

DEDICATION

This dissertation is dedicated to my family.

ACKNOWLEDGMENTS

I would like to first express my gratitude towards my advisor, Dr. Robert J. Nemanich, for offering me the opportunity to work in such an amazing group, and for his tireless support and encouragement during my graduate school study and research. His enthusiasm and invaluable knowledge made it possible for me to complete a doctorate of philosophy in physics. His advice and inspiration will no doubt benefit me for my whole life.

I would also like to thank my committee members, Dr. Martha McCartney, Dr. Fernando Ponce, and Dr. Quan Qing, for serving on my committee and contributing to the development of this work.

I would like to thank all of my group members that helped me in my Ph.D. study. I want to give my special thanks to Dr. Tianyin Sun, who gave me guidance on research when I first started, taught me the knowledge about material science, design of experiment, and paper writing. It is a pleasure for me to work with Xingye Wang. Thank you for your help on equipment, preparing the diamond samples and discussion on any research questions. It is so fortunate to have Franz Koeck who supports the lab with his expertise of vacuum techniques. I am grateful to the work of Dr. Jialing Yang and Dr. Brianna Eller on ALD and the work of Dr. Joeseph Shammas on c-BN. I certainly could not have completed this work as efficiently without their efforts. I would like to extend my appreciation to Dr. Anna Zaniewski, Dr. Manpuneet Kaur Benipal, and Mei Hao who help me with any questions I got. I am glad I got opportunities to assist Yichen Yao and Jesse Brown.

It was also very valuable experience to collaborate with other research groups. Thank Dr. Michael Geis, Dr. Mark Hollis and Dr. Travis Wade of MIT-Lincoln Laboratories and Dr. Timothy Grotjohn of Michigan State University for their thoughtful discussion over the years. Thank Dr. Srabanti Chowdhury, Dr. Maitreya Dutta, and Harshad Surdi, from whom I learn a lot about device fabrication and cleanroom. Thanks to Dr. Shariar Anwar for the help on the Hall effect measurement.

This research is supported by the Office of Naval Research under Grant # N00014-10-1-0540, the National Science Foundation under Grant # DMR-1206935 and grand form MIT Lincoln Laboratories.

Finally, I would like to thank my parents, other family members, and all the friends, for your lasting love and support.

TABLE OF CONTENTS

Page

LIST OF TABLES x

LIST OF FIGURES xi

CHAPTER

1 INTRODUCTION 1

1.1 Surface Conductivity of H-terminated Diamond 1

1.1.1 Background 1

1.1.2 Surface Transfer Doping on Diamond 2

1.1.3 Surface Conductivity of Diamond with Metal Oxides 4

1.1.4 Surface Conductivity Characterization 8

1.2 Electron Affinity of Cubic Boron Nitride 9

1.2.1 Background 9

1.2.2 Negative Electron Affinity Surface 11

1.2.3 Negative Electron Affinity Enabled by Metal Oxides 12

1.2.4 Electron Affinity Characterization 14

1.3 Thesis Approach 15

References 17

2 INSTRUMENTS AND ANALYSIS METHOD 21

2.1 Introduction 21

2.2 Remote Plasma Processing System 22

2.3 Remote Plasma-Enhanced Atomic Layer Deposition (PEALD) 24

2.3.1 Principle of Atomic Layer Deposition (ALD) 24

CHAPTER Page

2.3.2 PEALD Reactor Configuration....26

2.3.3 PEALD of Al_2O_3....28

2.4 Molecular Beam Deposition (MBD)....31

2.5 Photoemission Spectroscopy....33

2.5.1 Principle of Photoemission Electron Spectroscopy....31

2.5.2 X-ray Photoemission Spectroscopy (XPS)....35

2.5.3 Ultraviolet Photoemission Spectroscopy (UPS)....36

2.5.4 Calibration of XPS and UPS....37

2.6 Characterization with Photoelectron Spectroscopy....39

2.6.1 Film Composition....39

2.6.2 Band Bending....40

2.6.3 Band Alignment....41

2.6.4 Electron Affinity....42

2.7 Hall Effect Measurement....43

References....45

3 AL_2O_3 DIELECTRIC LAYERS ON H-TERMINATED DIAMOND: CONTROLLING SURFACE CONDUCTIVITY....46

3.1 Abstract....46

3.2 Introduction....47

3.3 Experiment....49

3.4 Results....51

3.4.1 PEALD Al_2O_3 Deposition and Hydrogen Plasma Treatment....51

CHAPTER Page

3.4.2 Correlation of Binding Energy and Surface Resistance 53

3.4.3 Plasma Effects 54

3.4.4 Oxide Charge States 57

3.5 Discussion 59

3.5.1 Interface Model 59

3.5.2 Band Alignment Schematics 60

3.6 Conclusion 63

References 64

4 SURFACE TRANSFER DOPING OF DIAMOND/MOO_3 WITH AN AL_2O_3 INTERFACE LAYER 66

4.1 Abstract 66

4.2 Introduction 66

4.3 Experiment 68

4.4 Results 70

4.4.1 Photoelectron Spectroscopy (PES) Characterization 70

4.4.2 Hall Electrical Characterization 72

4.5 Discussion 75

4.5.1 Band Alignment of H-terminated Diamond/Al_2O_3/MoO_3 75

4.5.2 Effect of the Al_2O_3 Interfacial Layer Thickness 76

4.6 Conclusion 78

References 78

CHAPTER Page

5 ELECTRON AFFINITY OF CUBIC BORON NITRIDE TERMINATED WITH VANADIUM OXIDE 81

5.1 Abstract 81

5.2 Introduction 82

5.3 Experiment 83

5.4 Results 86

5.4.1 Cubic BN with O-termination 86

5.4.2 BN-1 87

5.4.3 BN-2 90

5.4.4 BN-3 92

5.5 Discussion 94

5.5.1 Surface and Interface Composition 94

5.5.2 Plasma and Annealing Effects 96

5.5.3 Electronic Properties 97

5.6 Conclusion 101

References 102

6 SUMMARY AND FUTURE WORK 105

6.1 Summary 105

6.2 Future work 107

6.2.1 Surface Condition Enabling Surface Conductivity 107

6.2.2 Metal-oxide-semiconductor Field Effect Transistors (MOSFETs) Based on Surface Conductive Diamond 107

CHAPTER Page

6.2.3 Electron Affinity of N-type c-BN Surface 109

References 109

REFERENCES 111

LIST OF TABLES

Table Page

1.1 Band Gap (Eg), Dielectric Constant (k), Conduction Band Offsets (CBO), and Valence Band Offsets (VBO) Measured for Dielectrics on H-Terminated Diamond. 6

1.2 A Comparison of Properties Between C-BN and Diamond. 11

2.1 Al_2O_3 Thin Film Properties on Si Wafers Grown by Remote PEALD Using DMAI and Substrate Temperature of 25 °C and 200 °C. Reprinted from Yang *Et Al. J. Vac. Sci. Technol. A* **32**, 021514 (2014) [6]. Copyright 2014, American Vacuum Society. 30

2.2 The Oxygen Pressure and Deposition Temperature of MBD Deposition for Several Oxides Commonly Used. 33

3.1 XPS of C 1s, Al 2p and O 1s Core Levels Results for Boron-Doped Diamond. All Values Are in Units of Ev and Have an Uncertainty of ±0.1 eV. 53

4.1 Hall Measurement Sheet Resistance, Carrier Concentration and Carrier Mobility of Diamond Surface Using MoO_3 as Acceptor Layer with 0, 2, and 4 nm Al_2O_3 Interfacial Layer. 74

5.1 B 1s, N 1s, O 1s Core Levels, Effective Work Function (Φ_W) and VBM for O-Terminated C-BN Relative to the Fermi Level, in eV. 87

5.2 B 1s, N 1s O 1s, V $2p_{3/2}$ Core Levels, Effective Work Function (Φ_W) and VBM for BN-1 Relative to the Fermi Level, in eV. 89

5.3 B 1s, N 1s O 1s, V $2p_{3/2}$ Core Levels, Effective Work Function (Φ_W) and VBM for BN-2 Relative to the Fermi Level, in eV. 91

Table Page

5.4 B 1s, N 1s O 1s, V $2p_{3/2}$ Core Levels, Effective Work Function (Φ_W) and VBM for BN-3 Relative to the Fermi Level, in eV. 92

LIST OF FIGURES

Figure Page

1. 1 Band Diagrams of Diamond, Showing the Activation Energies of Common Dopants and Vacuum Levels of O-Terminated and H-Terminated Surfaces. 3

1.2 Schematic Diagrams of H-Terminated Diamond Surface (a) Without and (b) With Air-Induced Adsorbates. After Surface Transfer Doping, A Hole Accumulation Layer Forms on Diamond Surface with Associated Upward Band Bending. 5

1.3 Summary of Band Alignments of Dielectrics on H-Terminated Diamond, Showing the Values of CBO and VBO. 6

1.4 Band Diagrams of Surface Transfer Doping n H-Terminated Diamond Surface Enabled by Materials with A High Electron Affinity (χ>4.2 eV). 8

1.5 Crystal Structure of C-BN. Boron and Nitrogen Atoms Are in Black and White, Respectively. 10

1.6 Schematic Diagrams of UPS Spectra for an NEA Surface (Blue Line) And a PEA Surface (Red Line). 14

2.1 Photograph and Schematic Graph of The UHV Transfer Line and Integrated UHV System. 22

2.2 Schematic Illustration of the Remote Plasma Processing System.....24

2.3 Schematic Illustration of Typical ALD Process, Showing a 4-Step Process for One Deposition Cycle. 25

2.4 Schematic Illustration of PEALD System. 28

Figure Page

2.5 Schematic Illustration of the Relation Between the PEALD Growth Rate and Substrate Temperature. The Region of Constant Growth Is Called the "ALD Growth Window." 30

2.6 Schematic Illustration of MBD System, Showing the Side View of Sample, Heater, Crucible, Electron Emitter and E-Beam Path. 32

2.7 The "Universal Curve" of Electron Mean Free Path of Various Metals as A Function of Kinetic Energy. 35

2.8 Schematic Illustration of UPS System, Showing the Relative Positions of The UV Lamp, the Sample and the Electron Analyzer. The Dashed Line Indicates the Path Along That the Respective Part Can Move or Rotate. 37

2.9 XPS Scan of a Standard Au Foil, Showing the 4f Peaks that Are Used for XPS Calibration. 38

2.10 UPS Scan of A Standard Au Foil with -2V Bias. The High Energy Cut-Off at 19.7 eV Is Referred to the Fermi Level for UPS Calibration. 39

2.11 Demonstration of How (a) The Band Bending and (b) The VBO at an Interface Between the Substrate (Red Line) and the Dielectric (Blue Line) Are Calculated from Core Level and VBM Measurements. 41

2.12 Photograph of A 5×5 mm^2 Diamond Mounted on Clip Board for Sheet Resistance and Hall Effect Measurement. 44

3.1 The Respective XPS Scans of the O 1s, C 1s and Al 2p Core Levels of (i) H-Terminated Diamond Surface with Air Exposure, (ii) after 1 nm Al_2O_3 Deposition, (iii) 500 °C H-Plasma Treatment, (iv) after 2 nm Al_2O_3 Deposition,

Figure Page

(v) after 20 nm Al_2O_3 Deposition, and (vi) 500 °C H-Plasma Treatment. (For Different Elements, the Intensity Scales Are Adjusted for Better Visibility.) 52

3.2 The C 1s Binding Energy And Resistance Of The Diamond Surface For The Different Process Steps. 55

3.3 XPS Scans for O 1s And C 1s Core Levels of (i) H-Terminated Diamond Surface with Air Exposure, (ii) after Oxygen Plasma Treatment, (iii) after Hydrogen Plasma Treatment and (iv) Air Exposure. (For Different Elements, the Intensity Scales Are Adjusted for Better Visibility.) 56

3.4 XPS Scans of a Diamond Surface with a 2 nm Layer of Al_2O_3 and Hydrogen Plasma Treatment, Showing the O1s, C 1s and Al 2p Core Levels after (i) an Additional 2 nm PEALD Al_2O_3 Deposition (This Surface Is Essentially the Same as Scan (iv) In Fig. 1), (ii) 500 °C Vacuum Anneal, and (iii) 500 °C Hydrogen Plasma Process. (For Different Elements, the Intensity Scales Are Adjusted for Better Visibility.) 58

3.5 XPS Scans of a Diamond Surface with a Thin Layer of Al_2O_3 ~8 nm And Hydrogen Plasma Treatment, Showing the O1s, C 1s and Al 2p Core Levels (i) before and (ii) after Thermal Anneal at 500 °C. (For Different Elements, the Intensity Scales Are Adjusted for Better Visibility.) 58

3.6 Interface Band Diagrams of Al_2O_3 on Diamond Showing Band Bending and Possible Charged States Distributions after Each Process: (i) Hydrogen Terminated Diamond with Air Exposure, (ii) 1st PEALD Al_2O_3 Deposition ~1 nm, (iii) Hydrogen Plasma Treatment at 500 °C and (iv) 2nd PEALD Al_2O_3

Deposition ~2 nm. The Charges in the Schematic Diagram Indicate Their Spatial Position, Not Their Energy Relative to the Band Gap. 62

4.1 XPS Scans of Diamond/0 nm Al_2O_3/MoO_3 after Each Process, Showing the (a) O 1s, (b) C 1s, and (c) Mo 3d Core Level Peaks. 71

4.2 XPS Scans of Diamond/2 nm Al_2O_3/MoO_3 after Each Process, Showing the (a) O 1s, (b) C 1s, (c) Mo 3d, and (d) Al 2p Core Level Peaks. 72

4.3 XPS Scans of Diamond/4 nm Al_2O_3/MoO_3 after Each Process, Showing the (a) O 1s, (b) C 1s, (c) Mo 3d, and (d) Al 2p Core Level Peaks. 73

4.4 (a) The Change of Sheet Resistance, Hole Concentration and Hole Mobility with Processes for Diamond/MoO_3 with 0/2/4 nm Al_2O_3 Interfacial Layers. (b) The Hole Concentration and Mobility of Different Structures. 76

4.5 The Band Diagrams of Diamond/MoO_3 and Diamond/Al_2O_3/MoO_3 before and after MoO_3 Deposition. 77

5.1 (Color Online) XPS Scans of The O-Terminated C-BN Sample, Showing the (a) B 1s, (b) N 1s, (c) O 1s Core Level Peaks, and (D) the UPS Scans. The Work Function Variations Are Indicated in the UPS Scans. 87

5.2 (Color Online) XPS Scans of the BN-1 Sample, Showing the (a) B 1s, (b) N 1s, (c) O 1s Core Level Peaks, and (d) the UPS Scans. 89

5.3 (Color Online) XPS Scans of BN-2, Showing the (a) B 1s, (b) N 1s, (c) O 1s and V $2p_{3/2}$ Core Level Peaks, and (d) the UPS Scans. 91

5.4 (Color Online) XPS Scans of BN-3, Showing the (a) B 1s, (b) N 1s, (c) O 1s and V $2p_{3/2}$ Core Level Peaks, and (d) the UPS Scans. 93

Figure Page

5.5 Band Schematics of the Two Models: (a) Interface Barrier Model, and (b) Surface Dipole Model. 98

5.6 (Color Online) Schematic Diagrams of Surface Dipoles and Corresponding Band Diagrams for (a) H-Terminated C-BN, (b) O-Terminated C-BN and (c) Vanadium-Oxide-Terminated C-BN. The Changes of the Vacuum Level Due to Surface Dipoles Are Profiled. 100

5.7 Band Schematics near the C-BN Surface of (a) O-Terminated C-BN, (b) BN-1, and (c) BN-2. 100

6.1 Schematic of H-Terminated Diamond Circular Surface-Channel FET. 108

CHAPTER 1

INTRODUCTION

Diamond and cubic boron nitride (c-BN) are ultra-wide bandgap (UWBG) semiconductors, with bandgap significantly wider than the 3.4 eV of GaN. UWBG semiconductors have the potential for performance far superior to that of conventional wide bandgap (WBG) semiconductors, because many of the figures-of-merit for device performance scale with increasing bandgap in a highly non-linear manner. The device characteristics depend critically on the electronic states at semiconductor interfaces. Understanding the interfaces is important to improve the performance of UWBG semiconductor devices. This dissertation investigated two unique properties derived from the UWBG of diamond and c-BN, the surface conductivity of diamond, and the negative electron affinity of c-BN.

1.1 Surface Conductivity of H-terminated Diamond

1.1.1 Background

The diamond crystal structure can be descried as two identical interpenetrating face-centered-cubic (FCC) sublattices, where each carbon atom is tetrahedrally bonded to four nearest neighbor atoms of the opposite FCC sublattice. The strong sp^3 bonding between atoms in diamond makes diamond a unique material that exhibits extraordinary mechanical, chemical and electronic properties. For applications in electronic devices, diamond has advantageous properties, including a wide band gap (5.47 eV) sustaining a high breakdown field >10 MV/cm, a high electron mobility (4500 $cm^2/(V•s)$) and hole

mobility (3800 $cm^2/(V•s)$), high saturated drift velocity (1×10^7 cm/s), and high thermal conductivity (22 W/(cm•K)). [1] Particularly, two features of diamond make it unique among all semiconductors: one is the negative electron affinity (NEA) property of diamond and the other is the high p-type surface conductivity of the hydrogen-terminated (H-terminated) diamond surface, which is closely related to the NEA feature. From these components, diamond is promising for applications such as electron emitters, thermionic energy conversion devices, photocathodes, high power and high frequency electronics, etc. [2]

1.1.2 Surface Transfer Doping on Diamond

As a WBG material, the carrier density of undoped diamond is extremely low ($n_i=p_i\sim10^{-27}$ cm^{-3}) at room temperature, so that undoped diamond is a bona fide insulator. Therefore, doped diamond with desirable conductivities is essential for electronic applications. Even though doping diamond with both acceptor and donor impurities has been demonstrated, achieving appropriate conductivity through doping s still a challenge. The rigid and compact nature of the diamond lattice results in very low solubility for dopant atoms larger than carbon and restricts the commonly used doping process, such as ion-implantation followed by thermal diffusion. [3] The activation energies of common dopants in diamond are high, as summarized in Fig. 1.1. Consequently, the activation rates of dopants in diamond are low at room temperature. Specifically, for p-type doping with boron, the activation fraction of boron in diamond is less than $1/10^4$ at room temperature. [4]

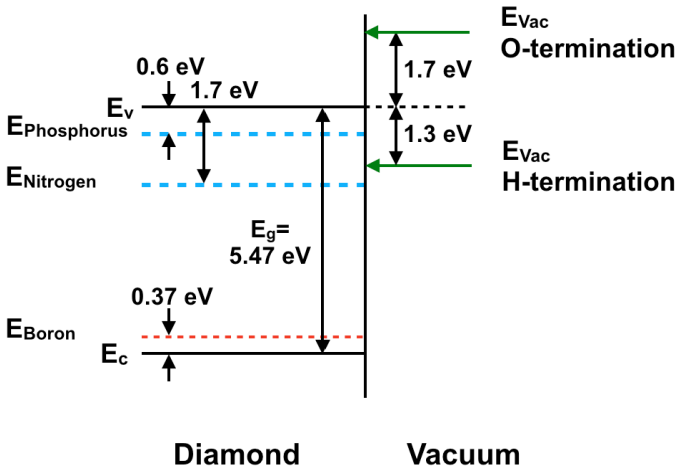

Figure 1.1 Band diagrams of diamond, showing the activation energies of common dopants and vacuum levels of O-terminated and H-terminated surfaces.

In 1989, Landstrass and Ravi first reported the low electrical resistivity of H-terminated chemical vapor deposition (CVD) diamond surfaces. [5] The surface conductivity with a sheet resistance 10^3-10^4 Ω/sq has been ascribed to p-type carriers with a sheet hole concentration around 10^{13} cm^{-2} and a hole mobility between 10 and 100 $cm^2/(V \bullet s)$. Several models have been proposed to explain the formation of p-type surface conductivity on H-terminated diamond. These models explain the mechanism in terms of the passivation of deep levels due to subsurface hydrogen, [5,6] the presence of shallow acceptor states induced by incorporated hydrogen, [7-9] surface oxidation caused by adsorbate molecules, [10,11] a charge transfer redox reaction in an adsorbed water layer, [12,13] and the spontaneous polarization model. [14] The electrochemical surface transfer doping model is now well accepted over the other competing models. [15]

In this model, the energy difference between the Fermi level diamond and the electronic empty acceptor states of surface adsorbates, such as lowest unoccupied molecular orbitals (LUMOs) of molecular adsobates, prompts electrons to transfer from the valence band of diamond to surface adsorbates, resulting in a layer of accumulated holes on the diamond surface and an equal density of negative charges in surface adsorbates. The accumulated holes and negatively charged adsobates form a space-charge layer with associated upward band bending toward the diamond surface. Under thermodynamic equilibrium, the Fermi levels of the diamond and the LUMOs of the surface adsobate layer are aligned, and the Fermi level of diamond is below the valence band maximum (VBM) of diamond. A schematic of the energy band diagrams showing surface transfer doping process on H-terminated diamond is presented in Fig. 1.2. The activation energy of the two-dimensional hole gas can be very low compared to common dopants in diamond. For example, the activation energy of holes induced by NO_2 adsorbed on H-terminated diamond surface was reported as low as 6.2 meV, so that holes were fully activated at room temperature. [16]

1.1.3 Surface Conductivity of Diamond with Metal Oxides

Although p-type surface conductivity can be readily achieved on H-terminated diamond by charge transfer doping with air-induced adsorbates, the air-induced surface conductivity on H-terminated diamond is not thermally stable above ~190 °C in vacuum. [17] The air-induced adsorbates desorb from the surface during heating above room temperature, resulting in a decrease of the hole concentration. [18] Moreover, an oxidation process that modifies the surface termination can result in an irreversible degradation of

the surface conductivity. For electronic device applications, the thermal and chemical stability of surface conductivity of diamond should be improved. There is a need to develop new passivation layers that can either stabilize or replace the adsorbates. In previous studies, various dielectric layers including Al_2O_3, [19] SiO_2, [20] HfO_2, [21] $LaAlO_3$, [22] AlN, [23] MoO_3, [24] and V_2O_5, [25] which have been used as passivation layers on the H-terminated diamond surfaces, have been deposited by thermal evaporation, thermal atomic layer deposition (ALD), or metal organic chemical vapor deposition (MOCVD).

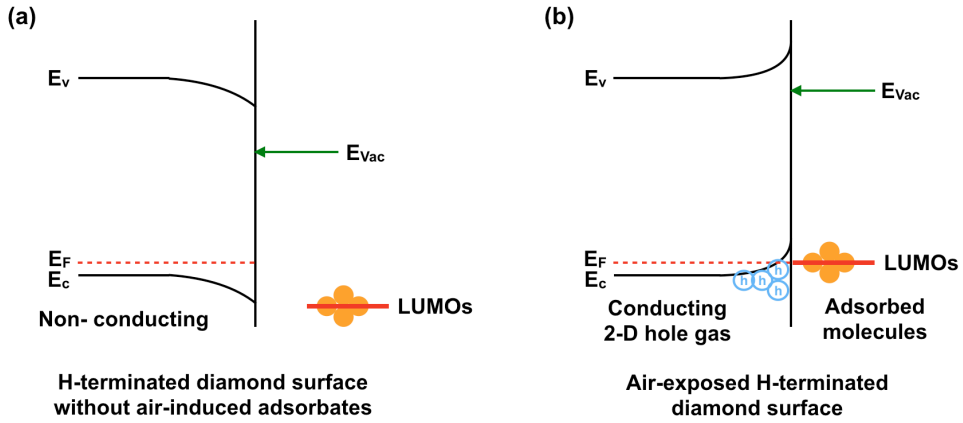

Figure 1.2 Schematic diagrams of H-terminated diamond surface (a) without and (b) with air-induced adsorbates. After surface transfer doping, a hole accumulation layer forms on diamond surface with associated upward band bending.

The device characteristics depend critically on the dielectric properties. The two most important factors are the band gap and the dielectric constant. The band gap relates to the ability of dielectrics to confine carriers. The dielectric constant determines the electric field across the dielectric. The band gaps, dielectric constant sand band offsets for commonly used dielectrics on H-terminated diamond are summarized in Table 1.1. The band alignments are plotted in Fig. 1.3.

Table 1.1. Band gap (Eg), dielectric constant (k), conduction band offsets (CBO), and valence band offsets (VBO) measured for dielectrics on H-terminated diamond.

	Al_2O_3	SiO_2	$LaAlO_3$	HfO_2	TiO_2	ZrO_2	MoO_3	V_2O_5	ZnO
Eg	7.2	9.0	6.7	5.4	3.2	5.6	3.1	2.3	3.37
K	9	3.9	30	25	80	25	18	20	8
CBO	-1.2	1.4	-2.8	-2.7	-4.9	-2.2	-6.2	-5.65	-3.85
VBO	2.9	2.1	4.0	2.6	2.6	2.3	3.8	2.45	1.75

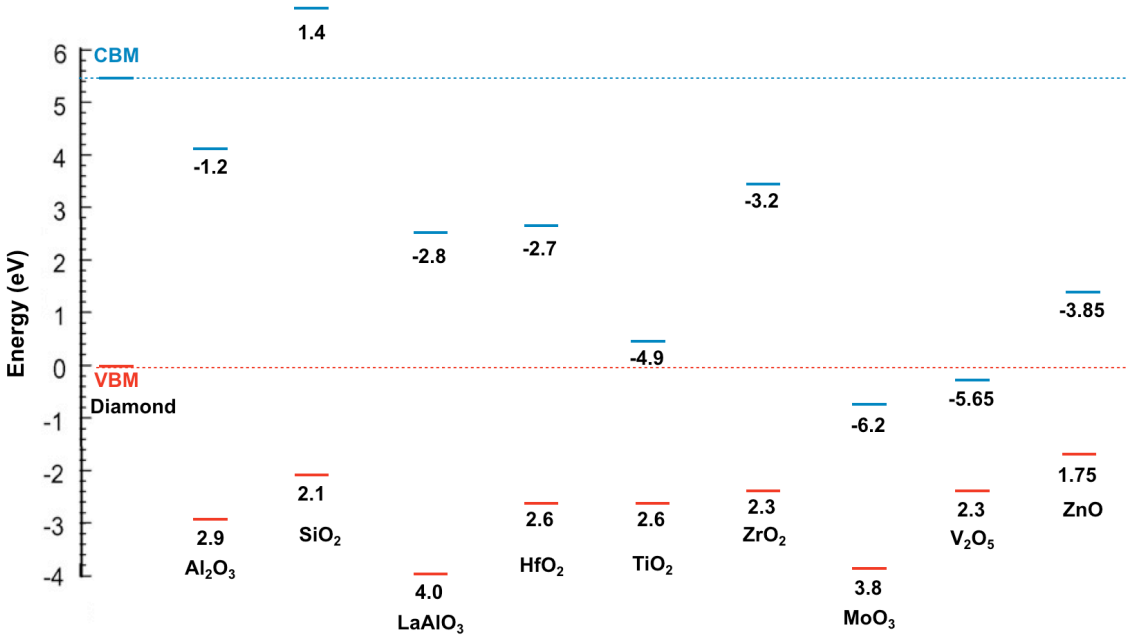

Figure 1.3 Summary of band alignments of dielectrics on H-terminated diamond, showing the values of CBO and VBO.

Among these dielectrics, Al_2O_3 is a promising material to achieve surface conductivity on diamond. Al_2O_3 is employed as a dielectric layer in field effect transistors (FETs) because of its good thermal and chemical stability, large band gap (~7 eV), and sufficient dielectric constant (~10). Kawarada *et al.* have reported the formation of a surface hole accumulation on H-terminated diamond surface after Al_2O_3 deposition by ALD with H_2O as an oxidant. [26] Compared to the air-induced surface conductivity, the dielectric/diamond interface is retained at high temperature (>400 °C).

With sufficiently high electron affinities (χ>4.2 eV), oxides like niobium pentoxide (Nb_2O_5), tungsten trioxide (WO_3), vanadium pentoxide (V_2O_5) and molybdenum trioxide (MoO_3), align such that their LUMOs levels are below the H-terminated diamond VBM ($E_{VBM}=E_{gap}+\chi_{H\text{-termianted diamond}}\approx4.2$ eV). This alignment enables electron transfer from the diamond to the oxides, as shown in Fig.1.4. The amount of electron transfer, that is hole sheet concentration, is correlated to the work function of the oxides. A higher work function of the oxides results in a higher hole sheet concentration. [27] The challenge of using high electron affinity material as the acceptor layer is that the hole mobility decreases with an increase in the hole concentration. It is due to that in the case of charge transfer doping, the density of the ions is not distributed homogenously in the oxide, but accumulate in a layer adjacent to the hole accumulation layer in the diamond. [28] Those ions give rise in Comlomb scattering in the hole accumulation layer. It is well-established that the ionized impurity scattering is proportional to the density of ionized impurities. In the case of charge transfer doping, the density of ions in the adsorbate layer is equal to the hole sheet concentration in the diamond. Therefore, an increase in the hole sheet concentration is associated with a decrease in the hole mobility

due to the ionized impurity scattering. Furthermore, the scattering by the ions in the adsorbate layer limits the performance of electronic devices based on surface conductivity of H-terminated diamond.

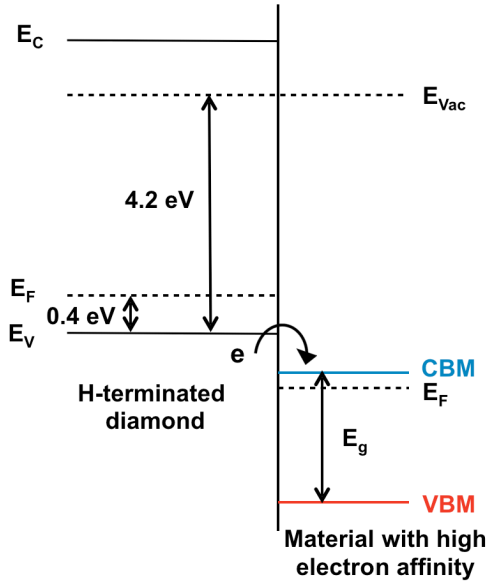

Figure 1.4 Band diagrams of surface transfer doping on H-terminated diamond surface enabled by materials with a high electron affinity (χ>4.2 eV).

1.1.4 Surface Conductivity Characterization

Hall effect measurements are commonly used to characterize the surface conductivity of H-terminated diamond. The hole mobility, hole concentration and sheet resistance of two-dimensional hole accumulation layer can be measured by Hall effect. For surface conductive H-terminated diamond, the sheet resistance is usually within the range of 5-20 kΩ/sq. The hole density ranges from 10^{12} to 10^{13} cm^{-2}, with a hole mobility between 50-150 $cm^2/(V•s)$. [29,30]

Besides Hall effect measurements, the two-dimensional hole gas of surface conductive diamond can be characterized using X-ray photoemission spectroscopy (XPS). [31] In the case of surface transfer doping, the two-dimensional hole gas and negatively charged ions in acceptor layer result in upward band bending toward the diamond surface. The Fermi level of diamond is near the VBM at the diamond surface, which results in two-dimensional hole gas. Thus, the surface band bending is correlated to the surface transfer doping. Furthermore, the energy difference between VBM and C 1s core level of diamond is constant and virtually independent of band bending. The changes in the surface hole density can be monitored by the relative position of the C 1s core level using XPS.

Overall, surface transfer doping provides an effective, high density doping method that could enable field effect device. The major challenges are achieving stability and increased mobility.

1.2 Electron Affinity of Cubic Boron Nitride

1.2.1 Background

The cubic phase of boron nitride has the zinc-blende lattice structure with sp^3-hybrideized bonds as shown in Fig. 1.5, and is isoelectronic to diamond with similar properties to various aspects of diamond. Zinc-blende c-BN is a III-V compound with ionic banding and polar characters.

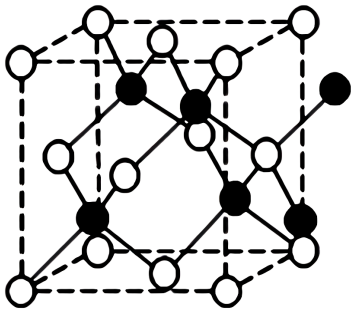

Figure 1.5. Crystal structure of c-BN. Boron and nitrogen atoms are in black and white, respectively.

Cubic boron nitride (c-BN) has a wide band gap of 6.1-6.4 eV, a breakdown field expected to be greater than 15 MV/cm, [32, 33] the second highest thermally conductivity (13 W/cm K) next to diamond. [34] The 1.36 % lattice mismatch with diamond, which enables the direct and epitaxial growth of c-BN on diamond and c-BN. Therefore, c-BN may work as an intermediary layer between diamond and other III-V semiconductors. [35] The properties of c-BN that are superior to diamond include the oxidation (1200 °C) and sp^3 to sp^2 phase transformation temperatures (1500 °C) of c-BN are much higher than those of diamond (600 °C and 1400 °C) [36] and both n- and p-type conductivity can be achieved on c-BN [37] while n-type conductivity of diamond is still challenging. [2] A comparison of properties between c-BN and diamond are summarized in Table 1.2. The excellent properties of c-BN make it promising for tooling, hard coatings, and electronic and optoelectronic device applications.

Table 1.2 A comparison of properties between c-BN and diamond. [35]

Properties	c-BN	Diamond
Structure	CubF43m	CubFd3m
Lattice constant (Å)	3.615	3.567
Interatomic distance (Å)	1.57	1.54
Density (g/cm)	3.48	3.51
Hardness (GPa)	60-75	100
Thermal Conductivity (W/(cm•K))	13	20
Band gap (eV)	6.1-6.4	5.47
Breakdown voltage (V/cm)	8.0×10^{6}	10^{7}
Dielectric constant at 300 K	5.8 (7.1)	5.7

1.2.1 Negative Electron Affinity Surface

The electron affinity of a semiconductor is the energy difference between the conduction band minimum (CBM) and the vacuum level. An NEA surface is when the position of vacuum level is below the CBM. The electrons in the conduction band can leave an NEA surface without encountering an energy barrier, resulting in a strong emissivity.

A material with a large band gap has the potential to exhibit an NEA, since its CBM may be positioned near the vacuum level. The surface terminating atoms and the

bonded atoms with different electronegatives can induce dipoles across the surface due to charge transfer. These dipoles result in a potential step perpendicular to the surface and affect the position of the vacuum level relative to the CBM.

By using a point charge approximation for a diatomic molecule, the surface dipole moment can be estimated by

$p = d\Delta q$, (1.1)

where d is the bond length and the Δq is the charge transfer between two atoms. In a diatomic molecule, the Δq is determined by [38]

$\Delta q = 0.16|X_A - X_B| + 0.035|X_A - X_B|^2$, (1.2)

where X_A and X_B are the electronegativities of the two atoms. The surface dipoles decrease the electron affinity when the electronegativity of the surface terminating atoms is larger than the electronegativity of the bonded atoms, or vice versa. When there are multiple sorts of surface dipoles on one surface, the change of the position of the vacuum level can be estimated by a weighted summation of all surface dipole moments on the surface.

Like H-terminated diamond, H-terminated c-BN has ben shown to exhibits an NEA. [39,40] The H-terminated c-BN surface is dominated by N-H bonds, which create dipoles due to charge transfer between the H adatoms (X_H=2.2) and the topmost layer of N atoms (X_N=3.04). The resulting dipole layer shifts the relative position of the vacuum level below the CBM of c-BN, and the H-terminated c-BN exhibits an NEA. [41]

1.2.3 Negative Electron Affinity Enabled by Metal Oxides

The ability to exhibit NEA makes c-BN a promising candidate as an electron source for applications including photocathodes, photo-electrochemistry substrates and thermionic energy conversion application. For thermionic emission applications, high temperature operation is desired to achieve a high conversion efficiency. Although the H-terminated surface is easily achieved on diamond and c-BN to obtain NEA, hydrogen desorbs from the diamond and c-BN surfaces at temperatures above 800 °C. [40, 42, 43] The NEA is easily destroyed by thermal annealing in air or with an oxygen plasma or other oxidation processes, [5, 44, 45] which limits the ability of these NEA materials in thermionic emission applications. It is necessary to investigate alternative surface terminations that sustain an NEA and provide improved thermal stability.

P-type vacuum cleaved GaAs (110) surfaces terminated with Cs has been reported to exhibit an NEA. [46] However, by alternately applying Cs and O, an even lower vacuum level for the GaAs (110) surface can be obtained. [47] Here the oxidized Cs forms the dipole layer and lowers the vacuum level. Recent theoretical and experimental studies have shown that transition metal oxides, such as Cu, [48] Ni, [49] Ti, [50-52] Co and Zr [53] on oxygen terminated diamond surface, are stable and can significantly influence the electronic properties of diamond. By forming a metal-oxygen dipole layer at the surface, a few monolayers of transition metal oxides can significantly reduce the electron affinity. Furthermore, transition metal oxides show advantages over other terminations in compatibility with both Schottky and Ohmic contacts fabrication processes. [54, 55] Therefore, it is worthwhile to examine the electron affinity of c-BN terminated with transition metal oxides.

1.2.4 Electron Affinity Characterization

The electron affinity of a surface can be characterized with ultraviolet photoelectron spectroscopy (UPS). As shown in Fig.1.6, an NEA surface is indicated in two aspects of a UPS spectrum. For an NEA surface, there is a sharp peak at low kinetic energy, which is attributed to secondary electrons thermalized to the CBM. While for a PEA surface, these electrons would be bound in the conduction band. The other difference is the spectrum width, which in the case of NEA is larger than $h\nu$-E_g and in the case of PEA is equal to $h\nu$-E_g-χ, where $h\nu$ is the incident photon energy, Eg is the material band gap and is χ is the electron affinity.

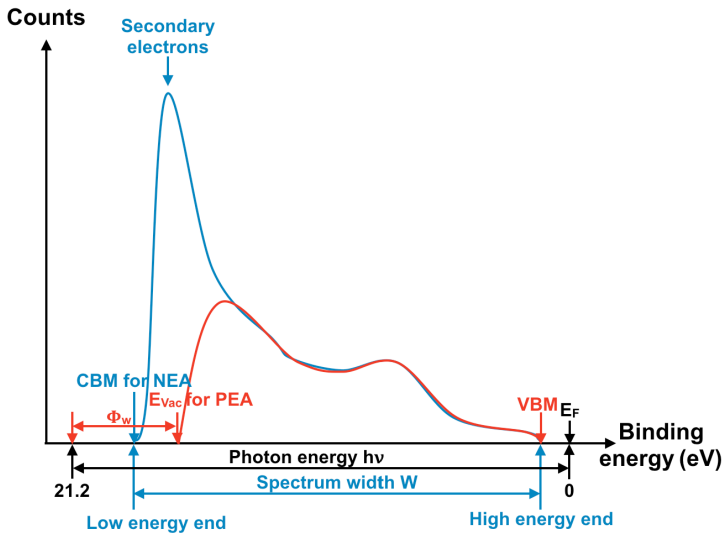

Figure 1.6 Schematic diagrams of UPS spectra for an NEA surface (blue line) and a PEA surface (red line).

Overall, the wide gap of c-BN suggests that the material may exhibit a robust NEA, which may lead to applications in new electron sources for high-temperature devices. Metal oxide terminated surfaces promise improved thermal stability compared to

previous reported H-terminated surfaces, and is able to enhance the thermionic emission by forming highly polarized surface dipoles.

1.3 Thesis approach

This dissertation is focused on using *in situ* photoelectron spectroscopy (PES) to characterize interface electronic states of dielectrics on diamond and c-BN. The unique properties of dielectrics on diamond and c-BN are related to the interface electronic states.

In chapter 2, the instruments and analysis method used in this thesis are introduced, including: remote plasma system for surface process, plasma-enhanced atomic layer deposition (PEALD) and molecular beam deposition (MBD) for dielectric layer deposition, XPS and UPS for surface characterization, Hall effect system for electric characterization and band alignment analysis method.

In chapter 3, surface conductive diamond has been achieved with Al_2O_3 employed as a dielectric layer deposited by PEALD with a post-deposition hydrogen plasma treatment. The changes of the hole accumulation layer were monitored by correlating the binding energy of the diamond C 1s core level with electrical measurements. The presence of interface charges is related to the band diagram and to the processing steps. The hydrogen termination is considered important to lower the molecular levels below the diamond valence band. An interface layer between the diamond and dielectric layer is proposed to explain the surface conductivity.

In chapter 4, the surface conductivity of diamond was further investigated. To obtain two-dimensional hole gas with high hole mobility, a thin layer of Al_2O_3 has been employed as an interfacial layer between H-terminated diamond and MoO_3 with an

electron affinity of 6.7 eV. The Al_2O_3 interfacial layer increases the distance between hole accumulation layer and acceptor layer to reduce ionic scattering caused by negative charged ions in acceptor layer. The sheet resistance, hole concentration and hole mobility of different structures were characterized. The hole mobility was found to be improved significantly with an Al_2O_3 interfacial layer.

In chapter 5, a study is presented of the electron affinity of vanadium-oxide-terminated c-BN. The vanadium oxide films of monolayer thickness were deposited on c-BN surface with MBD and oxygen plasma process in different sequences, in order to investigate the different electron affinity resulted from different surface dipoles. The band diagrams of diamond with different termination are presented. The transition metal oxides were found to be able to significantly influence the electronic properties of c-BN and enable NEA on c-BN.

In chapter 6, the most crucial results in this thesis are summarized, and future studies based on current work are proposed.

References

[1] J.Y. Tsao, S. Chowdhury, M.A. Hollis, D. Jena, N.M. Johnson, K.A. Jones, R.J. Kaplar, S. Rajan, C.G. Van de Walle, E. Bellotti, C.L. Chua, R. Collazo, M.E. Coltrin, J.A. Cooper, K.R. Evans, S. Graham, T.A. Grotjohn, E.R. Heller, M. Higashiwaki, M.S. Islam, P.W. Juodawlkis, M.A. Khan, A.D. Koehler, J.H. Leach, U.K. Mishra, R.J. Nemanich, R.C.N. Pilawa-Podgurski, J.B. Shealy, Z. Sitar, M.J. Tadjer, A.F.Witulski, M. Wraback, and J.A. Simmons, Advanced Electronic Materials, in press.

[2] Robert J. Nemanich, John A. Carlisle, Atsushi Hirata, and Ken Haenen, MRS Bulletin **39**, 490 (2014).

[3] L.G. Wang, A. Zunger, Physics Review B **66**, 161202 (2002).

[4] N. Fujimori, H. Nakahata, and T. Imai, Japanese Journal of Applied Physics **29**, 824 (1990).

[5] M.I. Landstrass, K.V. Ravi, Applied Physics Letters **55**, 975 (1989).

[6] M.I. Landstrass, K.V. Ravi, Applied Physics Letters **55**, 1391 (1989).

[7] T. Maki, S. Shikama, M. Komori, Y. Sakaguchi, K. Sakuta, T. Kobayashi, Japanese Journal of Applied Physics **31**, 1446 (1992).

[8] K. Hayashi, S. Yamanaka, H. Okushi, K. Kajimura, Applied Physics Letters **68**, 376 (1996).

[9] K. Hayashi, S. Yamanaka, H. Watanabe, T. Sekiguchi, H. Okushi, K. Kajimura, Journal of Applied Physics **81**, 744 (1997).

[10] R.S. Gi, T. Mizumasa, Y. Akiba, Y. Hirose, T. Kurosu, M. Iida, Japanese Journal of Applied Physics **34**, 5550 (1995).

[11] R.S. Gi, T. Ishikawa, S. Tanaka, T. Kimura, Y. Akiba, M. Iida, Japanese Journal of Applied Physics **35**, 2057 (1997).

[12] F. Maier, M. Riedel, B. Mantel, J. Ristein, L. Ley, Physics Review Letters **85**, 3472 (2000).

[13] K. Larsson, J. Ristein, Journal of Physical Chemistry B **109**, 10304 (2005).

[14] K. Hirama, H. Takayanagi, S. Yamauchi, J.H. Yang, H. Kawarada, H. Umezawa, Applied Physics Letters **92**, 112107 (2008).

[15] D. Takeuchi, M. Riedel, J. Ristein, and L. Ley, Physical Review B **68**, 41304 (2003).

[16] M. Kasu, H. Sato, and K. Hirama, Appled Physics Express **5**, 025701 (2012).

[17] M. Riedel, J. Ristein, and L. Ley, Physical Review B **69**, 125338 (2004).

[18] M. Kasu, M. Kubovic, A. Aleksov, N. Teofilov, Y. Taniyasu, R. Sauer, E. Kohn, T. Makimoto, and N. Kobayashi, Diamond and Related Materials **13**, 226 (2004).

[19] K. Hirama, H. Sato, Y. Harada, H. Yamamoto, and M. Kasu, IEEE Electron Device Letters **33**, 1111 (2012).

[20] M.W. Geis, Proceedings of the IEEE **79**, 669 (1991).

[21] J.W. Liu, M.Y. Liao, M. Imura, H. Oosato, E. Watanabe, and Y. Koide, Applied Physics Letters **102**, 112910 (2013).

[22] J.W. Liu, M.Y. Liao, M. Imura, H. Oosato, E. Watanabe, A. Tanaka, H. Iwai, and Y. Koide, Journal of Applied Physics **114**, 84108 (2013).

[23] D. Kueck, P. Leber, A. Schmidt, G. Speranza, and E. Kohn, Diamond and Related Materials **19**, 932 (2010).

[24] S.A.O. Russell, L. Cao, D. Qi, A. Tallaire, K.G. Crawford, A.T.S. Wee, and D.A.J. Moran, Applied Physics Letters **103**, 202112 (2013).

[25] K.G. Crawford, L. Cao, D. Qi, A. Tallaire, E. Limiti, C. Verona, A.T.S. Wee, and D.A.J. Moran, Applied Physics Letters **108**, 42103 (2016).

[26] A. Daicho, T. Saito, S. Kurihara, A. Hiraiwa, and H. Kawarada, Journal of Applied Physics **115**, 223711 (2014).

[27] C. Verona, W. Ciccognani, S. Colangeli, E. Limiti, M. Marinelli, and G. Verona-Rinati, Journal of Applied Physics **120**, 025104 (2016).

[28] C.E. Nebel, New Diamond and Frontier Carbon Technology **15**, 5 (2005).

[29] B. Rezek, H. Watanabe, and C. E. Nebel, Applied Physics Letters **88**, 042110 (2006).
[30] K. Hirama, K. Tsuge, S. Sato, T. Tsuno, Y. Jingu, S. Yamauchi, and H. Kawarada, Applied Physics Express **3**, 044001 (2010).

[31] M.T. Edmonds, C.I. Pakes, S. Mammadov, W. Zhang, A. Tadich, J. Ristein, and L. Ley, Applied Physics Letters **98**, 102101 (2011).

[32] C.B. Samantaray, and R.N. Singh, International Materials Reviews 50, 313 (2005).

[33] R.M. Chrenko, Solid State Communications **14**, 511 (1974).

[34] G. A. Slack, Journal of Physics and Chemistry of Solids **34**, 321 (1973).

[35] W. Zhang, Y.M. Chong, B. He, I. Bello, and S.T. Lee, "3.24 – Cubic Boron Nitride Films: Properties and Applications", In "Comprehensive Hard Materials", edited by V. K. Sarin, Elsevier, Oxford, 2014, Pages 607-639.

[36] V.L. Solozhenko, V.Z. Turkevich, and W.B. Holzapfel, Journal of Physical Chemistry B **103**, 2904 (1999).

[37] O. Mishima, J. Tanaka, S. Yamaoka, and O. Fukunaga, Science **238**, 181 (1987).

[38] W. Mönch, Semiconductor Surfaces and Interfaces, 3rd ed. (Springer, Heidelberg, 2001).

[39] M.J. Powers, M.C. Benhamin, L.M. Porter, R.J. Nemanich, R.F. Davis, J.J Cuomo, G.L. Doll, and S. J. Harris, Applied Physics Letters **67**, 3912 (1995).

[40] K.P. Loh, K. Nishitani-Gamo, I. Sakaguchi, T. Taniguchi, and T. Ando, Applied Physics Letters **72**, 3023 (1998).

[41] J. Shammas, T. Sun, F.A.M. Koeck, A. Rezikyan, and R.J. Nemanich, Diamond and Related Materials **56**, 13 (2015).

[42] J. van der Weide, Z. Zhang, P.K. Baumann, M.G. Wensell, J. Bernholc, and R.J. Nemanich, Physics Review B **50**, 5803 (1994).

[43] K.P. Loh, I. Sakaguchi, M. Nishitani-Gamo, T. Taniguchi, and T. Ando, Diamond and Related Materials **8**, 781 (1999).

[44] H. Nakahata, T. Imai, and N. Fujimori, Proceedings of the 2nd International Symppsium on Diamond Materials 487 (1991).

[45] S. Ri, C.E. Nebel, D. Takeuchi, B.Rezek, N. Tokuda, S. Yamasaki, and H. Okushi, Diamond and Related Materials **15**, 692(2006).

[46] J. J. Sheer and J. van Laar, Solid State Communications **3**, 189 (1965).

[47] A. A. Turnbull and G. B. Evans, Br. Journal of Applied Physics **1**, 155 (1968).

[48] H. Guo, Y. Qi, and X. Li, Journal of Applied Physics **107**, 033722 (2010).

[49] J. van der Weide and R.J. Nemanich, Physics Review B **49**, 13629 (1994).

[50] C. Bandis, D. Haggerty and B. B. Pate, Material Research Society Symposium Proceedings (2nd edn.), 339, 75 (1994).

[51] J. van der Weide and R.J. Nemanich, Journal of Vacuum Science & Technology B **10**, 1940(1992).

[52] Y. Jia, W. Zhu, E.G. Wang, Y. Huo, and Z. Zhang, Physics Review Letters **94**, 086101 (2015).

[53] P.K. Baumann and R.J. Nemanich, Journal of Applied Physics **83**, 2072 (1998).

[54] T. Tachibana, B.E. Williams, and J.T. Glass, Physics Review B **45**, 11968(1992).

[55] T. Teraji, S. Koizumi, and Y. Koide, Journal of Applied Physics **104**, 016104 (2008).

CHAPTER 2

INSTRUMENTS AND ANALYSIS METHOD

2.1 Introduction

Experiments in this thesis are mainly accomplished *in situ* with an integrated ultra-high vacuum (UHV) system, in which various processing and characterization chambers are connected by a linear UHV transfer line and isolated by gate valves, as shown in Fig. 2.1. The UHV transfer chamber is ~20 m long and is maintained at a base pressure of $\sim 5\times10^{-10}$ Torr. The samples are loaded into the transfer line via load lock chamber at each end of the transfer line, and then transported *in situ* to the processing or characterization chamber. The following instruments are employed in this research: a remote H_2 plasma chamber for vacuum annealing and post deposition treatment, a remote plasma-enhanced atomic layer deposition (PEALD) system for dielectric deposition and also served as a remote oxygen plasma chamber for oxidation processes, a reactive molecular electron beam deposition (MBD) system for metal oxide deposition, an X-ray and ultra-violet photoemission spectroscopy (XPS and UPS) system for electronic structure characterization, and an electron cyclotron resonance microwave plasma chemical vapor deposition (ECR MPCVD) system for cubic boron nitride (c-BN) deposition.

Other facilities utilized in this research includes a chemical room for sample preparation and cleaning, an electron beam evaporation system for contact deposition, an MPCVD system for the formation of hydrogen termination on diamond and boron doped diamond epitaxial layer growth, a probe station for semiconductor current voltage (I-V)

measurements, and a hall effect system for the characterization of sheet resistance, carrier concentration and mobility of diamond surfaces.

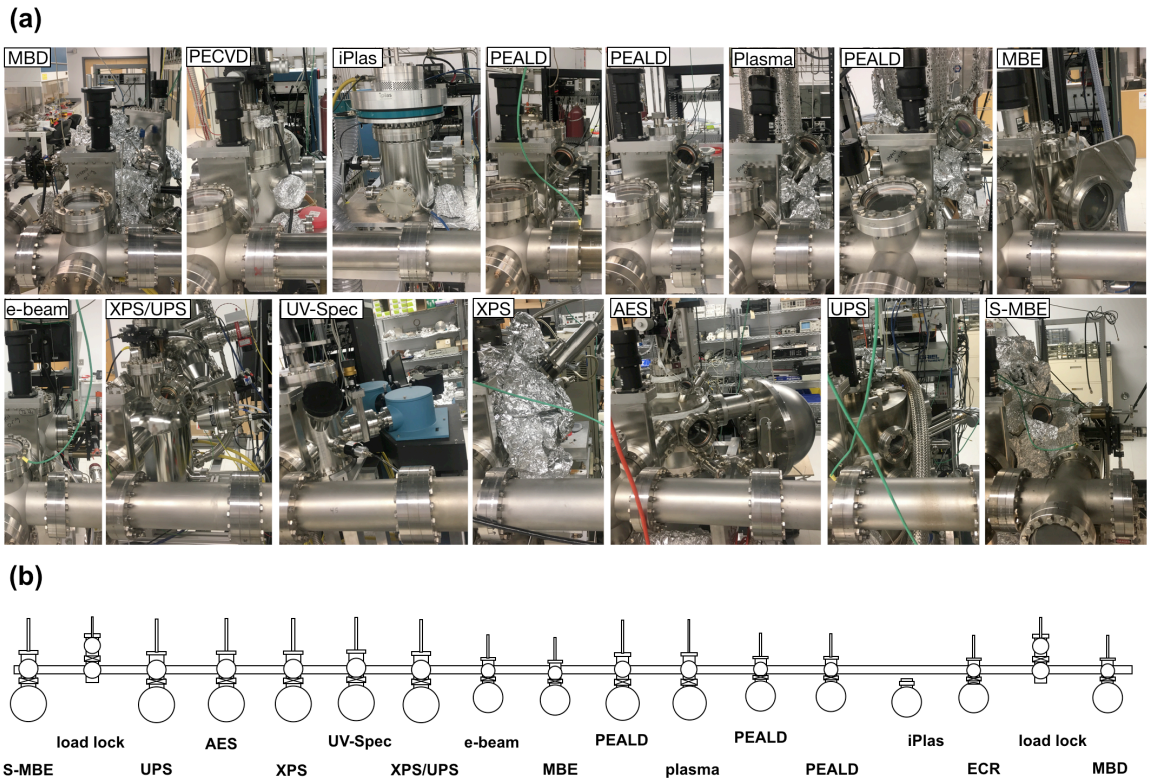

Figure 2.1 Photograph and schematic graph of the UHV transfer line and integrated UHV system.

2.2 Remote Plasma Processing System

A plasma is an electrically neutral collection of unbound positive and negative particles. In the laboratory, plasma is usually generated by the application of electric and/or magnetic fields to a gas. Compared to a direct plasma, for a remote plasma the sample stage is not involved in plasma generation, and the sample and plasma conditions can vary independently.

A schematic diagram of the remote plasma processing chamber, which is designed for the application of various gases, is shown in Fig. 2.2. The plasma is generated by a radio frequency (rf) source (100W, 13.56 MHz) applied to a helical copper coil around the ~32 mm diameter quartz tube. The electrical field between the coils and the top flange of the chamber accomplishes the initial ionization, then the collisions between electrons and the neutral gas atoms dissociate the reactant gas into radicals and ions, and finally the excited molecular radicals and species are delivered onto sample surface. In the sample region, the ion density is determined to be ~10^{8} cm^{-3} and ~10^{6} cm^{-3} at 15 and 300 mTorr respectively by using a double Langmuir probe, and the atomic H density is determined ~10^{11} cm^{-3} and independent of pressure in the range of 10-300 mTorr, by using a catalytic probe system. [1] The sample is held at the center of the chamber, facing up, and ~25 cm below the quartz plasma tube. This distance ensures the remote plasma supplies a sufficient flux of excited molecular radicals and species, and reduces the plasma damage caused by plasma radiation and ion bombardment. The chamber base pressure is ~5.0×10^{-9} Torr. For the H_2 plasma process in this research, the H_2 gas is delivered at a flow rate of 20 standard cubic centimeters per minute (sccm) using mass flow controller, and the chamber pressure is maintained at 100 mTorr controlled by a throttle valve in front of the turbo pump. The sample is heated with a tungsten irradiation filament heater coil beneath the sample holder. The temperature of the sample is controlled by a thermocouple placed behind the center of the sample, and calibrated with a Mikron M90Q infrared pyrometer.

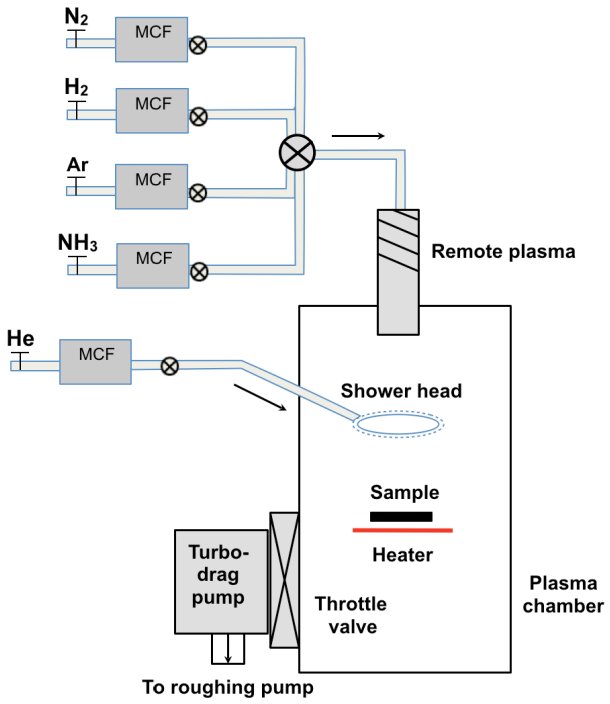

Figure 2.2 Schematic illustration of the remote plasma processing system.

2.3 Remote Plasma-Enhanced Atomic Layer Deposition (PEALD)

2.3.1 Principle of Atomic Layer Deposition (ALD)

Atomic layer deposition (ALD) is a self-limiting vapor-phase thin film deposition technique based on the sequential non-overlapping use of a gas phase chemical process. A typical ALD process is shown in Fig. 2.3.

There are 4 steps in an ALD cycle: in the first step, the metal compound (typically referred to precursor) is delivered to the chamber by a carrier gas (typically Ar or N_2) and reacts with the substrate surface to form submonolayer to monolayer chemisorption; in the second step, the excess precursor and gaseous by-products are purged with a non-reactive gas (typically Ar or N_2 gas); in the third step, another precursor or oxidant is

delivered into the chamber that reacts with the previous precursor at the substrate surface; in the forth step, a second purge step using non-reactive gas is processed to remove the excess oxidant and gaseous by-products and prepares the sample surface for the next ALD cycle.

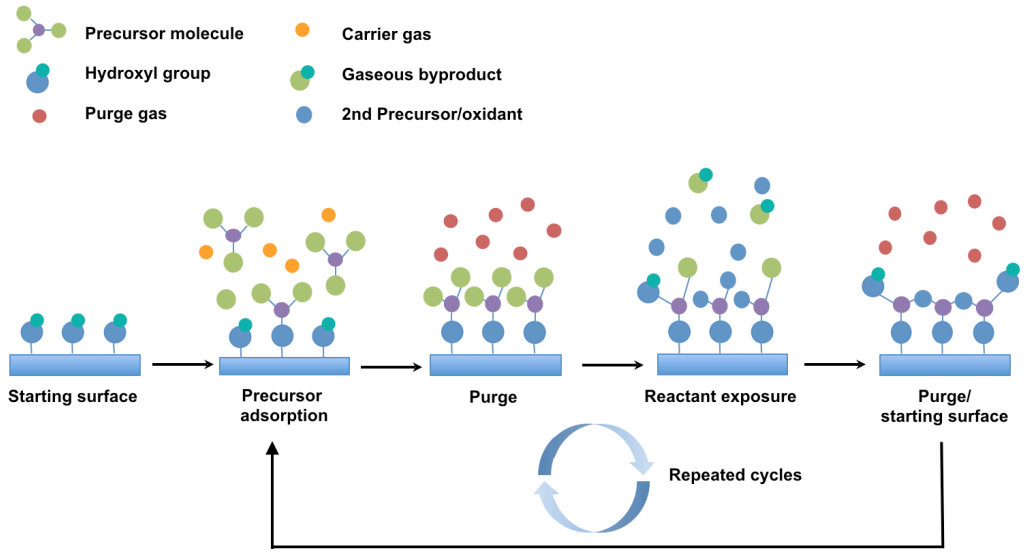

Figure 2.3 Schematic illustration of typical ALD process, showing a 4-step process for one deposition cycle.

By repeating these 4 steps, materials are deposited layer-by-layer. Instead of using the growth rate thickness/time, ALD processes are usually described in terms of growth rate per cycle (GPC). Ideally ALD GPC should remain as a constant in the ALD process window, and the thickness of the deposited films is the GPC multiplied by the number of ALD cycles. However, the GPC can be higher or lower before the GPC becomes a constant because the ALD initial growth may be affected by the conditions of the substrate surface. [2]

The precursor molecule is usually a metal atom bonded with ligand groups. In the first step, the precursor molecule is bonded to a surface reactive site and releases a ligand and adsorption site species as by-products. The number of reactive sites on the substrate is finite. Once all the reactive sites have been occupied, the reaction terminates, resulting in a self-limiting process. The maximum amount of material deposited in one single ALD cycle is determined by the nature of the precursor-surface interaction, such as adsorption sites, precursor molecule size, precursor reactivity etc. [2] Consequently, the ALD mechanism enables flux-independent, layer-by-layer, self-limiting deposition with precise atomic-scale thickness control of conformal and uniform films on large diameter substrates.

Conventional oxide ALD, termed as thermal ALD, usually uses water as the oxidant and the surface reactions are driven by thermal energy. The deposition temperature of thermal ALD is usually between 100 ~ 600 °C. [3-5] Plasma enhanced ALD (PEALD) is an energy enhanced ALD. By using activated oxygen species, such as O_2^* and O^*, generated by a plasma, PEALD enables a wider range of precursors, a decreased deposition temperature and impurity density, and also an increase of the growth rate and film density. [6,7]

2.3.2 PEALD Reactor Configuration

A schematic diagram of the remote PEALD system used in this research is shown in Fig. 2.4. The chamber is pumped by a turbo-drag pump backed by a roughing pump to achieve a base pressure ~6.0×10^{-9} Torr. During deposition, the roughing pump is switched to a dry pump to avoid purged oxides accumulating in the roughing pump. The

pressure of the chamber during deposition is controlled by a throttle valve in front of the turbo-drag pump. All gases, Ar, N_2, and O_2, are delivered using mass flow controllers. Research grade N_2 is used as the purge gas. Research grade O_2 is used as the oxidant source. The oxygen plasma is generated by a radio frequency (rf) source (13.56 MHz) applied to a helical copper coil around the ~32 mm diameter quartz tube that is ~25 cm above the sample. The forward plasma power varies from 20 to 200 W, with a reverse power < 30 W. The precursors are stored in different bubblers, which are maintained at different temperatures to provide a proper vapor pressure for the PEALD process. The precursor is delivered into the chamber using Ar as carrier gas. There are two ways, in which the Ar gas is mixed with the precursor: Ar gas is delivered through a bypass to reduce the amount of precursor delivered, when the precursor vapor pressure is high; Ar gas is delivered through the bubbler to increase the delivery of the precursor, when the precursor vapor pressure is low. During deposition, the pipelines between the bubblers and chamber are maintained at ~20 °C higher than the temperature of the corresponding bubbler, and the chamber is maintained at ~70 °C to prevent chemical condensation. The temperature of the sample is controlled by a thermocouple located at the center of a tungsten irradiation filament heater coil, and calibrated by a Mikron M90Q infrared pyrometer. The deposition process is controlled by a LabVIEW program.

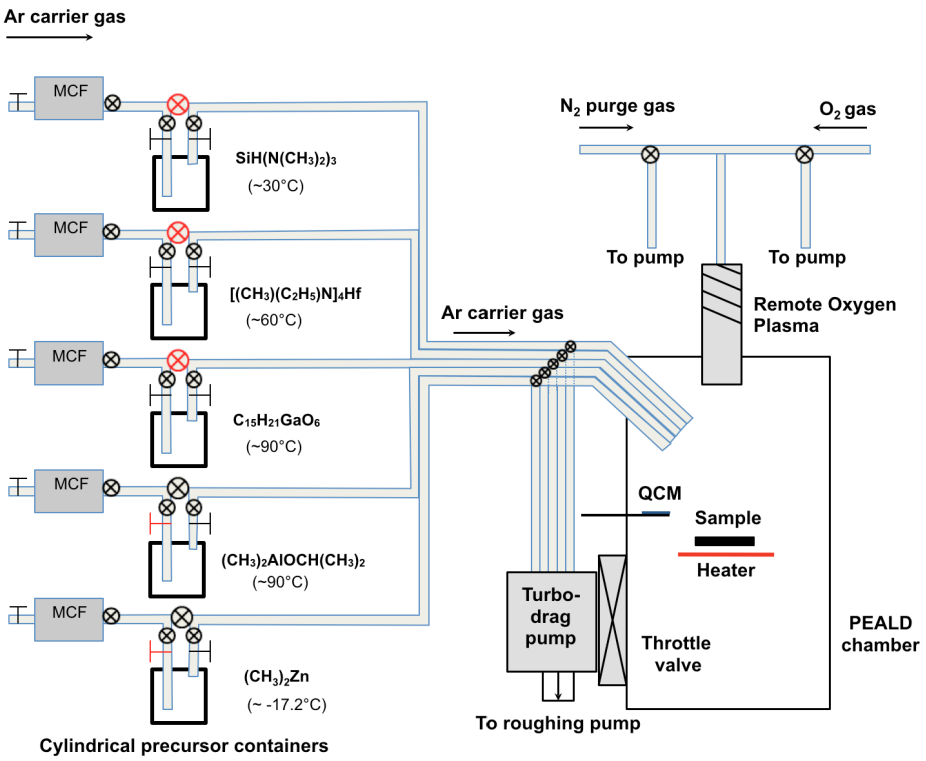

Figure 2.4 Schematic illustration of PEALD system.

2.3.3 PEALD of Al_2O_3

In this research, Al_2O_3 is deposited by PEALD to obtain surface conductivity on H-terminated diamond (Chapter 3) and is employed as an interface layer between H-terminated diamond and MoO_3 (Chapter 4). The PEALD Al_2O_3 growth method used in this research is fully investigated and reported in the previous work of our group. [6] Trimethyl (aluminum) (TMA) is commonly used as precursor for thermal ALD of Al_2O_3. However, TMA is pyrophoric and highly reactive with H_2O, requiring additional safety control. Dimethylaluminum isopropoxide (DMAI, $[(CH_3)_2AlOCH(CH_3)_2]_2$) is used as the Al_2O_3 precursor in our PEALD process. DMAI is not pyrophoric and has an appropriate

vapor pressure for the ALD process. Langereis and Potts *et. al.* have reported possible DMAI surface adsorption and reaction with O_2 plasma as following: [8,9]

$$\text{II} - OH_{(ads)} + \frac{1}{2}[(CH_3)_2AlOCH(CH_3)_2]_{2(g)}$$

$$\rightarrow \text{II} - OAl(CH_3)_2OCH(CH_3)_{2(ads)} + CH_{4(g)}$$

$$\text{II} - AlOCH(CH_3)_{2(ads)} + 9O^*_{(g)} \rightarrow \text{II} - Al(OH)_{(ads)} + 3H_2O_{(g)} + 3CO_{2(g)}, \quad (2.1)$$

and/or

$$\text{II} - OH_{(ads)} + \frac{1}{2}[(CH_3)_2AlOCH(CH_3)_2]_{2(g)}$$

$$\rightarrow \text{II} - OAl(CH_3)_{2(ads)} + HOCH(CH_3)_{2(g)}$$

$$\text{II} - Al(CH_3)_{(ads)} + 4O^*_{(g)} \rightarrow \text{II} - Al(OH)_{(ads)} + H_2O_{(g)} + CO_{2(g)}. \quad (2.2)$$

To achieve saturated and self-limiting growth, the precursor dose time, purge time, O_2 plasma dose time, and substrate temperature need to be optimized. Conventionally, the precursor dose time is increased until the GPC saturates. The O_2 plasma dose time is increased until the GPC is a constant, indicating the chemisorbed precursor is fully oxidized. The purge time is increased until the GPC is minimized, indicating the excess precursor is fully purged. The substrate temperature is a key parameter of ALD growth. The temperature window, T_1 to T_2, in which the growth is self-limiting and the GPC is a constant, is called the ALD growth window, as shown in Fig. 2.5. When the substrate temperature is below T_1, the GPC may increase due to precursor condensation on the surface or decrease due to incomplete reactions; when the substrate temperature is above T_2, the GPC may increase due to precursor decomposition or decrease due to precursor desorption. In this research, the precursor pulse time is 1.2 s followed by a 40 s N_2 purge. After chamber pressure reaching 100 mTorr with a 6 s O_2 purge, the O_2 plasma pulse

time is 8 s followed by a 40 s N_2 purge to prepare for the next ALD cycle. With a growth window of 25~220 °C, a constant growth rate ~1.5 Å/cycle is obtained. The composition of Al_2O_3 films is determined using RBS and XRR. The properties the Al_2O_3 film on Si substrates deposited by remote PEALD with DMAI as precursor at 25 °C and 200 °C are summarized in Table 2.1.

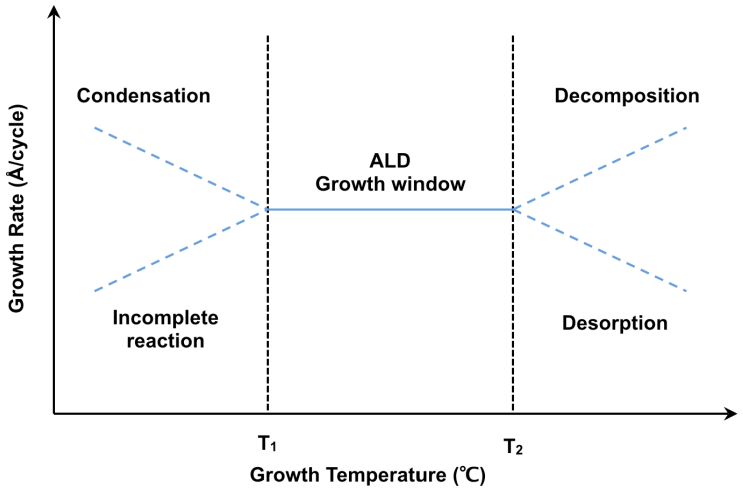

Figure 2.5 Schematic illustration of the relation between the PEALD growth rate and substrate temperature. The region of constant growth is called the "ALD growth window."

TABLE 2.1 Al_2O_3 thin film properties on Si wafers grown by remote PEALD using DMAI and substrate temperature of 25 °C and 200 °C. Reprinted from Yang *et al. J. Vac. Sci. Technol. A* **32**, 021514 (2014) [6]. Copyright 2014, American Vacuum Society.

PEALD growth temperature	25 °C	200 °C
Growth per cycle	1.5 Å/cycle	1.5 Å/cycle
Al atoms per cycle	3.9±0.3 at. $nm^{-2}cycle^{-1}$	5.3±0.3 at. $nm^{-2}cycle^{-1}$
Mass density	2.69±0.04 g/cm^3	2.96±0.02 g/cm^3

[O]/[Al] ratio	2.1±0.1	1.6±0.1
Refractive index (630 nm)	1.6±0.01	1.63±0.02
Band gap	--	6.7±0.1 eV
Electron affinity	--	2.2±0.1 eV

2.4 Molecular Beam Deposition (MBD)

An MBD system is employed for metal oxide films deposition, by using electron beam deposition source cooperated with an oxygen gas delivery system. A schematic diagrams of the MBD is shown in Fig. 2.6. The chamber base pressure is ~5.0×10^{-9} Torr. During deposition, the cryopump is isolated from the chamber by a gate valve, and the chamber is only pumped by the turbo-molecular pump. Research grade oxygen gas is delivered into the chamber through a Varian precision leak valve. The MBD system has three independent electron beam sources, installed with three different metals: titanium, vanadium, and molybdenum, with 99.99%, 99.999% and 99.99% purity, respectively. The electron beam deposition source was purchased from MDC, and equipped with an e-Vap CVS emission current source controller, an MDC e-Vap CVS 10, 10 kW power supply, and an SYCON sweep controller. The electron beam is generated by the thermionic emission effect of a filament current passing through tungsten emitter. Then the emitted electrons are accelerated by an electric field. The electrical field is established by a high voltage of 4.5-5.3 kV applied between the electron gun filament and the metal source. The accelerated electrons are confined and focused at the center of the metal source by a magnetic field. The magnetic field is generated by the magnets installed on

both sides of the emitter and crucible. The electron beam position can be adjusted by changing the high voltage and magnetic field. The electrons with high kinetic energy strike and heat up the metal source to evaporate. The sample is heated with a tungsten irradiation heater coil beneath the sample holder. The sample temperature is controlled by a thermocouple placed behind the center of the sample, and calibrated by a Mikron M90Q infrared pyrometer. The growth rate is controlled by adjusting the emission current, which is typically 50-300 mA, and monitored by a quartz crystal microbalance (QCM). A typical growth rate used in this research is ~0.01 nm/s.

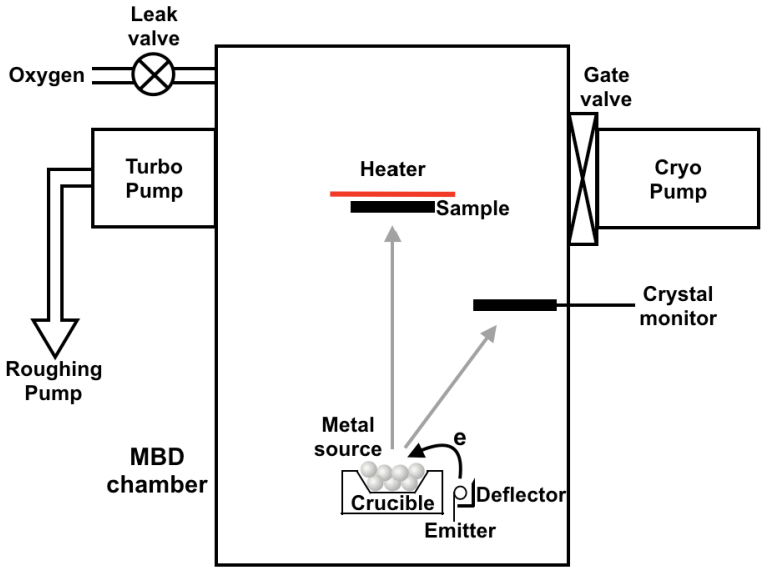

Figure 2.6 Schematic illustration of MBD system, showing the side view of sample, heater, crucible, electron emitter and e-beam path.

For transition metals oxides, such as Ti, V, and Mo, various oxidization states can be altered. For metal oxide deposition using MBD, the composition of the metal oxide is mainly determined by the oxygen pressure and deposition temperature. The high voltages

used for titanium, vanadium, and molybdenum metal sources are 5.2 kV, 4.5 kV, and 5.3 kV, respectively. The emission current is adjusted to obtain a growth rate of ~0.01 nm/s for all oxides. The rate may vary with time due to the degradation of the filament, which is caused by oxidation and evaporation of the oxide. The oxygen pressure and deposition temperature for several oxides commonly used are summarized in Table 2.2. The deposition of oxides in a high oxidation state, such as V_2O_5 and MoO_3, requires oxygen pressure in the rage of mTorr where arcing is often detected. There are two approaches to avoid the arcing problem. One is to reduce the value of the high voltage, and the other is to heat the emitter before deposition to reduce the adsorbed molecules on the emitter. If only a thin layer of oxides (< 2 nm) is needed, one optional method is to deposit a thin metal layer by MBD and then use an oxygen plasma to obtain oxides in a high oxidization state, which is used in Chapter 4.

Table 2.2 The oxygen pressure and deposition temperature of MBD deposition for several oxides commonly used.

	TiO_2	V_2O_3	VO_2	V2O5	MoO_x
Oxygen pressure (Torr)	5×10^{-5}	1×10^{-5}	7×10^{-4}	1×10^{-3}	4×10^{-4}
Temperature (°C)	250	650	450-550	650	25-250

2.5 Photoemission Spectroscopy

2.5.1 Principle of Photoemission Electron Spectroscopy

Photoemission spectroscopy is a surface-sensitive quantitative spectroscopic technique providing sample information, such as chemical composition, chemical state,

electronic state, etc. The photoelectron emission process has been described by the Spicer three-step model where the three successive steps include: optical absorption, electron transport, and escape across the surface. [10] The electrons inside the sample are excited to elevated energy states by the incident photons, and then transport to the sample surface. Most of electrons excited deep inside the sample cannot escape from the surface due to the energy losses caused by scattering and/or recombination. Only electrons excited near the surface can escape from the sample. The sampling depth is related to the electron mean free path, which varies for different elements and different electron kinetic energies, as shown in Fig. 2.7. The emitted electrons are collected by an electron spectrometer, in which the intensity of the electrons is recorded as a function of their kinetic energy. The energies of the emitted photoelectrons are characteristic of their original electronic states. Quantitatively, the binding energy of an electron in a solid is related to its emitted kinetic energy by the following equation:

$$BE = h\nu - KE - \Phi_W, \text{ (2.3)}$$

where BE is the electron binding energy referred to the Fermi level, hν is the incident photon energy, KE is the electron kinetic energy after excitation, and Φ_W is the work function of the material. In the measurement, the kinetic energy of the electron is referred to the vacuum level of the spectrometer. The binding energy is given by:

$$BE = h\nu - KE - \Phi_A + qV, \text{ (2.4)}$$

where Φ_A is the work function of the spectrometer, q is the elementary charge, and V is the bias applied between the sample and analyzer to provide electrons sufficient energy to overcome Φ_A and maximize the collection of electrons with low kinetic energies. Some scattered electrons with sufficient kinetic energies can also escape from the surface as

secondary electrons, forming a spectrum background signal with increasing intensity toward the low energy threshold.

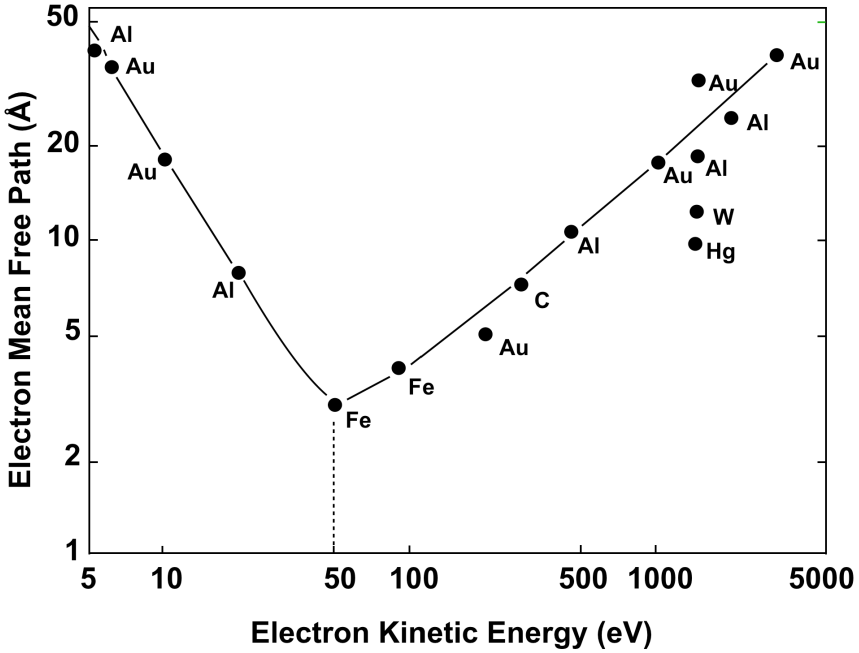

Figure 2.7 The "universal curve" of electron mean free path of various metals as a function of kinetic energy. [10]

2.5.2 X-ray Photoemission Spectroscopy (XPS)

The XPS system consists of a high intensity monochromatized Al K_α X-ray source, which is operated at 15 kV and 30 mA with a photon energy of 1486.7 eV and a bandwidth of 0.2 eV, and a Scienta R3000 high resolution electron energy analyzer, which includes high voltage electronics and a SCIENTA R3000 electron spectrometer with a resolution of 0.1 eV. The binding energy is recorded with a step of 0.05 eV. The core level position could be further resolved to ~0.05 eV by curve fitting. The sampling depth is around 5-10 nm. The spectrometer work function is ~4.25 eV. The chamber pressure is maintained ~1.5×10^{-9} Torr by dry pumps purchase from Pfeiffer Vacuum. A

UPS system is also integrated in this chamber, using He I radiation at 21.2 eV and the R3000 analyzer operating at a 2 eV pass energy with a resolution of 3 meV. The X-ray and UV light sources are focused at the same position of the sample.

2.5.3 Ultraviolet Photoemission Spectroscopy (UPS)

Compared to XPS, the major difference is that UPS operates with an ultraviolet light source to excite the electrons in the valence band of the sample. The sampling depth is usually less than 1 nm from the surface. The configuration of the UPS used in this research is shown in Fig. 2.8. The chamber is pumped by a cryopump and the base pressure is maintained at ~3×10^{-9} Torr. The UPS system is equipped with a VSW 50 mm hemispherical analyzer operated at fixed analyzer transmission (FAT) mode and a VSW HAC300 lens controller. The spectrometer records the number of electrons with kinetic energies in a range of 0~50 eV. The resolution varies from 20 meV to 500 meV by selecting the specific pass energy, while a pass energy of 15 eV is used in this research for a balance between spectral intensity and signal-to-noise ratio. The ultraviolet photons are generated by a gas discharge lamp, operated at a high voltage of 1 kV and a discharge current of 200 mA. The noble gases used are research grade purity (99.9999%) helium and UHP purity (99.9995%) argon. The gases are delivered to the lamp with a Varian precision leak valve. The lamp pressure is maintained by two turbo-pumps in a differential pumping configuration. The ultraviolet photons with photon energies of 21.22 eV, 40.82 eV, and 11.83 eV are obtained from He I, He II, and Ar I radiation, respectively. A tungsten irradiation heater coil is placed behind the sample holder to heat the sample. The sample temperature is controller by a thermocouple located at the center

of the coil, and calibrated by a Mikron M90Q infrared pyrometer. An -8.0 V bias is typically applied to the substrate to overcome the work function of the analyzer.

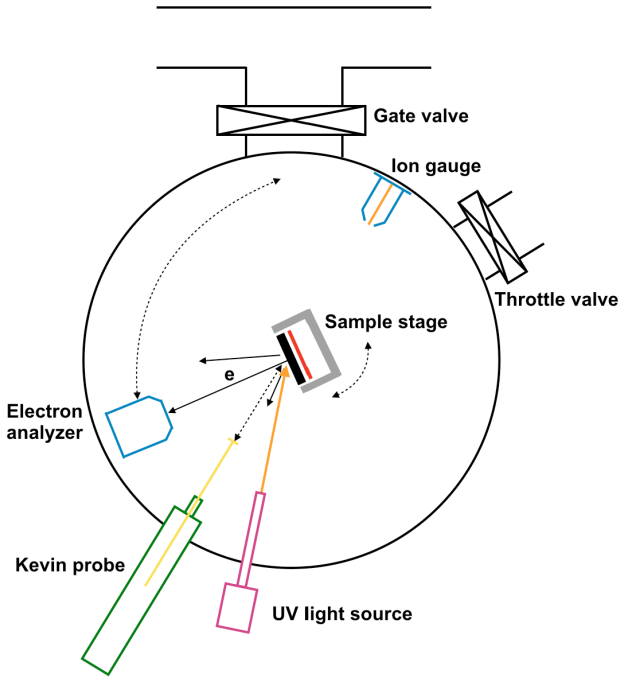

Figure 2.8 Schematic illustration of UPS system, showing the relative positions of the UV lamp, the sample and the electron analyzer. The dashed line indicates the path along that the respective part can move or rotate.

2.5.4 Calibration of XPS and UPS

To convert the kinetic energy of electrons into binding energy using equation (2.4), it is necessary to calibrate the spectrometer. A gold foil with a purity of 99.95% is used as a standard sample. Before calibration, the gold foil is cleaned *in situ* with a 15 min plasma process at room temperature, 5×10^{-5} Torr with a mix of Ar and H_2 at gas flow rates of 2.5 sccm and 20 sccm, repectively, to remove air-induced adsorbates and oxides.

For XPS calibration, the core levels of the standard sample are measured, as shown in Fig. 2.9, and then aligned to their standard positions in the literature. The standard binding energy position for Au $4f_{7/2}$ core level should be at 84.0 eV. The calibration is suggested to be 0 eV.

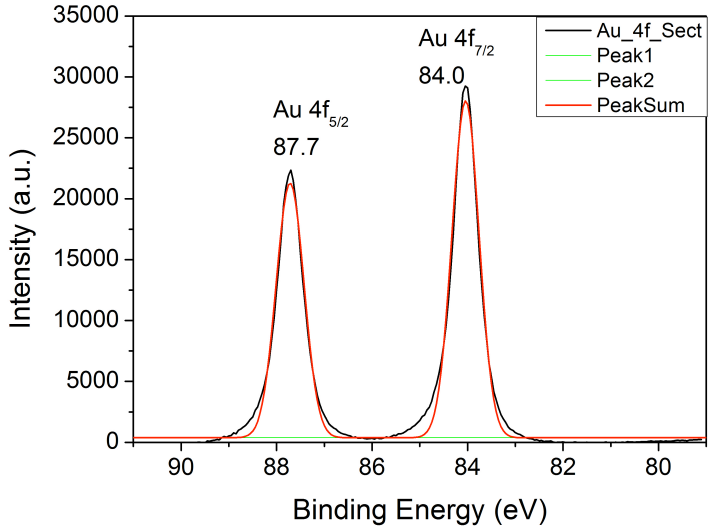

Figure 2.9 XPS scan of a standard Au foil, showing the 4f peaks that are used for XPS calibration.

For UPS calibration, the clear cut-off at the Fermi level is aligned to the zero binding energy position. Fig. 2.10 shows the UPS spectrum of the plasma cleaned standard gold foil, using He I radiation with a photon energy of 21.2 eV. A bias of -2 V is applied between the sample and the analyzer. The front cutoff is determined at 16.7 eV. By using the equation (2.4), the work function of the spectrometer Φ_A is calibrated to be 3.5 eV.

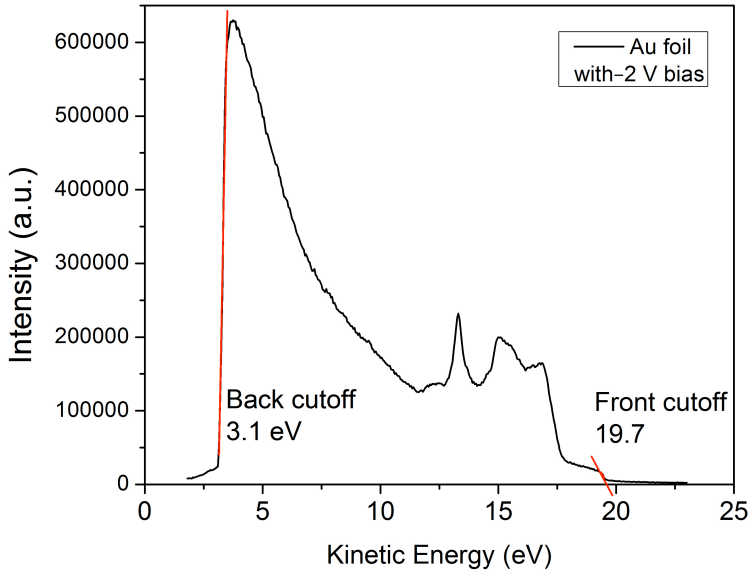

Figure 2.10 UPS scan of a standard Au foil with -2V bias. The high energy cut-off at 19.7 eV is referred to the Fermi level for UPS calibration.

2.6 Characterization with Photoelectron Spectroscopy

2.6.1 Film Composition

When the material is homogeneous and its thickness is at least several times of the electron mean free path, the intensity of spectral peaks should be given by, [12]

$I = nf\sigma y\phi AT\lambda$, (2.5)

where I is the peak area, n is the number of atoms per cubic centimeter, f is the X-ray flux, σ is the photoelectric cross-section, y is a photoelectric ground state efficiency factor ϕ is an angular correction factor, A is the area in which photoelectrons are detected, T is the detection efficiency of the analyzer at a specific photoelectron energy, and λ is the electron mean free path. By using the definition of the atomic sensitive factor S, the intensity of spectral peaks is given by,

$I = nS$, (2.6)

where S is a product of f, σ, y, ϕ, A, T, and λ. The film composition can be determined from the relative intensities of the core levels. The fraction of each element is given by the following equation,

$C_x = \frac{I_x}{S_x} / \sum_i \frac{I_i}{S_i}$, (2.7)

where C_x is the fraction of a specific element, I is the core level intensity and S is the atomic sensitive factory of the respective core level.

When a substrate is beneath a thin film, the intensity of the substrate is attenuated by the surface layer. The intensity of the substrate is reduced according to Beer Lambert's law,

$I_S = I_O e^{-\frac{d}{\lambda}}$, (2.8)

where I_s is the detected core level intensity of the substrate, I_o is the original intensity of the core level, d is the thickness of the surface layer, and λ is the effective attenuation length, which is usually related to the free mean path of the respective core level electrons.

2.6.2 Band Banding

The band bending (BB) of a substrate can be determined by the core level positions as shown in Fig. 2.11. The BB is given by

$BB = (E_{CL} - E_V)_{substrate} + E_g - E_{CL} + E_C$, (2.9)

where E_{CL} is the core level position, E_g is the band gap of the material, E_C is the position of the conduction band minimum (CBM), and $(E_{CL}\text{-}E_V)_{substrate}$ is the binding energy

difference from the respective core level to the valence band maximum (VBM). This equation applies to materials with low doping concentration, in which the area of the depletion region is significantly larger than the sampling depth. When the doping concentration is high, the quadratic nature of the depletion region should be considered.

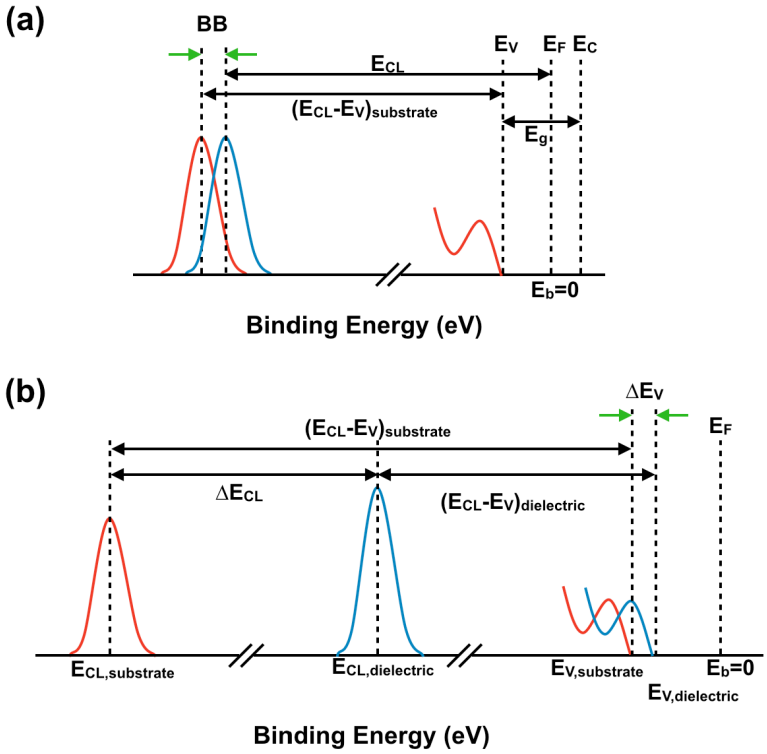

Figure 2.11 Demonstration of how (a) the band bending and (b) the VBO at an interface between the substrate (red line) and the dielectric (blue line) are calculated from core level and VBM measurements.

2.6.3 Band Alignment

The band alignment of a heterostructure can be determined from XPS and UPS spectra. By using the method proposed by Waldrop and Grant, [6] and Kraut *et al.*, [7] the

valence band offset (VBO) between substrate and dielectric layer can be calculated using the following equation, [13]

$$\Delta E_V = (E_{CL} - E_V)_{substrate} - (E_{CL} - E_V)_{dielectric} + \Delta E_{CL}$$, (2.10)

where ΔE_V represents the VBO; E_{CL} is the binding energy of the XPS core level; E_V is the valence band maximum (VBM); $(E_{CL}\text{-}E_V)_{substrate}$ and $(E_{CL}\text{-}E_V)_{dielectric}$ are the binding energy difference from the VBM to the respective core level and are constants which are virtually independent of band bending; and ΔE_{CL} is the binding energy difference between the substrate and dielectric core levels measured at the interface ($E_{CL}^{substrate}$-$E_{CL}^{dielectric}$). The conduction band offsets (CBO) can be derived from the VBO and the band gaps of the substrate and dielectric layers,

$$\Delta E_C = E_{g,dielectric} - E_{g,substrate} - \Delta E_V$$, (2.11)

where $E_{g,dielectric}$ and $E_{g,substrate}$ is the band gap of dielectric and substrate, respectively.

2.6.4 Electron Affinity

The electron affinity (EA) is defined as the energy required to remove an electron from the conduction band minimum (CBM) of a semiconductor into vacuum. For a surface exhibiting positive electron affinity (PEA), the value of EA can be determined from the UPS spectrum:

$$E_{ea} = h\nu - W - E_g$$, (2.12)

where hν is the incident photon energy, W is the bandwidth of the UPS spectrum, obtained from a linear extrapolation of the low- and high-kinetic energy cutoffs, and Eg is the material band gap. For a surface exhibiting negative electron affinity (NEA), the

value of EA cannot be determined from UPS spectrum. [14] The spectrum width W, the incident photon energy hν and the material band gap E_g are correlated as following:

$W = h\nu - E_g$. (2.13)

2.7 Hall Effect Measurement

The Hall effect measurement in this research is accomplished with a Van der Pauw structure. In this configuration, the four probes are placed at the corners of a square sample. To obtain the sheet resistance, a current is caused to flow along one edge of the sample and the voltage across the opposite edge is measured. A resistance can be found using Ohm's law. By assuming the sample surface is uniform, the sheet resistance can be estimated by [15]

$R_s = \frac{\pi R}{\ln 2}$, (2.14)

where R is the average of four edge resistances.

To characterize the sheet carrier concentration and mobility, a current is caused to flow across the diagonal of the sample, then an external magnetic field is applied perpendicular to the direction of current flow, and the resulted Hall voltage is measured across the other diagonal. The overall Hall voltage is obtained by switching the directions of magnetic field and current and averaging. The sheet density is given by

$n_s = \frac{IB}{q|V_H|}$, (2.15)

where n_s is the sheet carrier density, I is the drive current, B is the strength of the magnetic field, q is the elementary charge, and $|V_H|$ is the overall Hall voltage. The

majority carrier mobility, μ, can be derived from the previously calculated sheet resistance, R_s, and sheet density, n_s, as

$\mu = \frac{1}{qn_sR_S}$. (2.16)

The Hall effect measurement is accomplished with an HMS-3000 Hall measurement system from Ecopia. The precise constant current source can vary from 1 nA to 20 mA. The diamond samples are mounted on the spring clip board with four gold plated tips as shown in Fig. 2.12, and placed in a 0.55 T permanent magnet with a 26 mm pole gap. The measurements are taken at room temperature. The ohmic contacts required in Van der Pauw method are verified by I-V measurements.

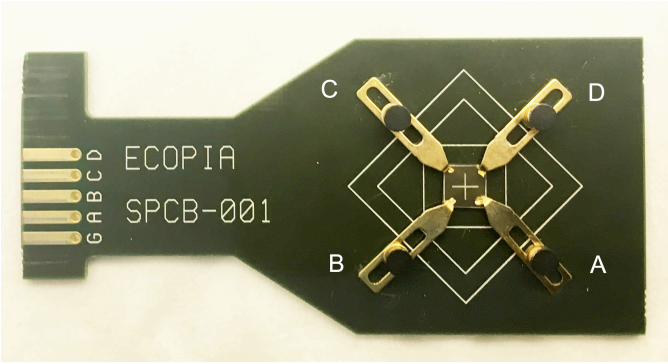

Figure 2.12 Photograph of a 5×5 mm^2 diamond mounted on clip board for sheet resistance and Hall effect measurement.

Reference

[1] Thomas P. Schneider, Ph.D. thesis, Hydrogen Plasma Interaction with Silicon Surfaces, North Carolina State University (1994).

[2] R.L. Puurunen, Journal of Applied Physics **97**, 121301 (2005).

[3] M. Ritala, M. Leskela, E. Nykanen, P. Soinien, and L. Niinisto, Thin Solid Films **225**, 228 (1993).

[4] A. Yamada, B.S. Sang, and M. Konagai, Applied Surface Science **112**, 216 (1997).

[5] E.B. Yousfi, J. Fouache, and D. Loncot, Applied Surface Science **153**, 223 (2000).

[6] J.W. Lim and S. Yun, Electrochemical and Solid-State Letters **7**, F45 (2004).

[7] J. Yang, B.S. Eller, M. Kaur, and R.J. Nemanich, Journal of Vacuum Science & Technology A **32**, 021514 (2014).

[8] E. Langereis, M. Creatore, S.B.S. Heil, M.C.M. van de Sanden, and W.M.M. Kessels, Applied Physics Letters **89,** 081915 (2006).

[9] J. Koo, S. Kim, S. Jeon, H. Jeon, Y. Kim, and Y. Wen, Journal of Korean Physical Society **48**, 131 (2006).

[10] W.E. Spicer, Physics Review **112**, 114 (1958).

[11] S. Hüfner, *Photoelectron Spectroscopy: Principles and Applications* (Springer, Berlin, 2003).

[12] C.D. Wagner, Journal of Electron Spectroscopy and Related Phenomena **32**, 99 (1983).

[13] J. R. Waldrop and R. W. Grant, Applied Physics Letters **68**, 2879 (1996).

[14] R.J. Nemanich, P.K. Baumann, M.C. Benjamin, O. –H Nam, A.T. Sowers, B.L. Ward, H. Ade, and R.F. Davis, Applied Surface Science **130**, 694 (1998).

[15] L.J. Van der Pauw, Philips Research Reports **20**, 220 (1958).

CHAPTER 3

AL2O3 DIELECTRIC LAYERS ON H-TERMINATED DIAMOND: CONTROLLING SURFACE CONDUCTIVITY

3.1 Abstract

This study investigates how the surface conductivity of H-terminated diamond can be preserved and stabilized by using a dielectric layer with an *in situ* post-deposition treatment. Thin layers of Al_2O_3 were grown by plasma enhanced atomic layer deposition (PEALD) on H-terminated undoped diamond (100) surfaces. The changes of the hole accumulation layer were monitored by correlating the binding energy of the diamond C 1s core level with electrical measurements. The initial PEALD of 1 nm Al_2O_3 resulted in an increase of the C 1s core level binding energy consistent with a reduction of the surface hole accumulation and a reduction of the surface conductivity. A hydrogen plasma step restored the C 1s binding energy to the value of the conductive surface, and the resistance of the diamond surface was found to be within the range for surface transfer doping. Further PEALD growth did not appear to degrade the surface conductive layer according to the position of the C 1s core level and electrical measurements. This work provides insight into approaches to establish and control the two-dimensional hole-accumulation layer of H-terminated diamond and improve the stability and performance of H-terminated diamond electronic devices.

(In collaboration with Franz A. Koeck, Maitreya Dutta, Xingye Wang, Srabanti Chowdhury, and Robert J. Nemanich)

3.2 Introduction

Diamond is an ultra wide band gap semiconductor with properties appropriate for high-frequency and high-power electronic devices; its wide band gap (5.47 eV) will sustain a high breakdown field; its high hole-mobility (3800 $cm^2/(V•s)$) results in a low forward resistance; its high saturated drift velocity (1×10^7 cm/s) supports high frequency operation, and its high thermal conductivity (22 W/(cm•K)) enables high power operation. [1] However, due to the large activation energies of dopants, specifically 0.37 eV for p-type doping with boron, the activation fraction of boron in diamond is less than $1/10^4$ at room temperature. [2] Recent research employing dielectric layers on H-terminated diamond has shown breakthroughs in high voltage and high frequency field effect transistor (FET) operation. [3-6] As an alternative doping strategy, studies have employed charge transfer on H-terminated diamond surfaces to form a surface conductive layer with a high density of holes. With air exposure, holes accumulate at the H-terminated diamond surface achieving a hole density of 10^{12}-10^{13} cm^{-2} and hole mobility of 50-150 $cm^2/(V•s)$. [7]

Several mechanisms have been proposed to explain how H-termination enables the surface hole accumulation layer that leads to the surface conductivity. The electrochemical surface transfer doping model is now well accepted over other competing models. In this model, after charge transfer, the Fermi level of the adsorbate layer and diamond are aligned, resulting in a layer of accumulated holes at the diamond surface and an equal density of compensating negative charges in the adsorbates. [8] However, there is still disagreement on the specific molecules that are the most effective in forming the air-induced surface conductivity. There is upward band bending in the diamond, and the

Fermi level is near the valence band maximum (VBM) at the surface. Changes in band bending correspond to changes in the surface transfer doping. Furthermore, the surface hole density will be reflected in the relative position of the C 1s core level binding energy determined by XPS. [9]

Although surface transfer doping can enable high performance diamond FET operation, the surface conductivity of the air-exposed H-terminated diamond surface is not thermally stable above ~190 °C in vacuum. [10] The atmospheric adsorbates desorb from the surface during heating above room temperature, resulting in a drop of the hole concentration. [11] For electronic device applications, the stability of H-terminated diamond FETs needs to be improved.

Kawarada *et al.* have reported the formation of a surface hole accumulation after Al_2O_3 atomic layer deposition (ALD) on diamond surfaces preheated to 450 °C. They suggest that the ambient adsorbates that are removed, [12] and that the air exposure process is apparently not necessary to obtain surface conductivity in the H-terminated diamond/Al_2O_3 structure. Apparently dielectric layers, like Al_2O_3, can enable surface conductivity on H-terminated diamond without molecular adsorbates. An indication that this process differs from the air-exposed, H-terminated surface is that the surface conductivity of the dielectric/diamond interface is retained at high temperature (>400 °C).

Various dielectric layers including SiO_2, [13] Al_2O_3, [14] AlN, [15] HfO_2, [16] $LaAlO_3$, [17] MoO_3, [18] and V_2O_5, [19] which have been used as insulators on the H-terminated diamond surface, have been deposited by thermal evaporation, thermal atomic layer deposition (ALD), or metal organic chemical vapor deposition (MOCVD).

Plasma enhanced ALD (PEALD) is an energy-enhanced ALD method that has been used to form high quality dielectric layers for semiconductor devices. By using activated oxygen species (e.g., O_2*, O*, O) generated by a plasma, PEALD enables conformal and uniform amorphous Al_2O_3 film growth with atomic scale thickness control, a decreased deposition temperature and impurity density, and also an increase of the growth rate and film density compared with chemical vapor deposition (CVD) or thermal ALD. [20,21] However, there have been few results on H-terminated diamond because the oxygen plasma step is thought to degrade the 2D hole accumulation layer in H-terminated diamond. [22] Consequently, we are motivated to investigate how the surface conductivity of H-terminated diamond can be preserved and stabilized by using a dielectric passivation layer with an *in situ* post-deposition treatment.

3.3 Experimental

Thin layers of Al_2O_3 were deposited on commercially obtained optical grade 4×4 mm^2 type IIa CVD single crystalline undoped diamond (100) substrates and 3×3 mm^2 type IIa CVD single crystalline diamond (100) substrates with lightly boron doped epitaxial layers. The boron doped layer prepared by Fraunhofer USA was used to mitigate charging shifts during X-ray photoemission spectroscopy (XPS). The boron concentration was estimated using Fourier transform infrared spectroscopy (FTIR) to be around 5-10 $\times 10^{17}$ cm^{-3}. The thickness of the epitaxial layer was ~6-10 μm.

H-terminated diamond surfaces were achieved in a hydrogen plasma excited with 1000 W microwave input for 15 min at ~800 °C (measured with an optical pyrometer). The chamber pressure was maintained at ~50 Torr with a H_2 flow rate of 400 standard

cubic centimeters per minute (sccm). After cool down the H-terminated diamond surface was exposed to air for ~12 h to obtain the atmospheric adsorbates responsible for surface conductivity.

Al_2O_3 films were deposited by remote PEALD. The precursor was dimethylaluminum isoproxide (DMAI, $[(CH_3)_2AlOCH(CH_3)_2]_2$), and oxygen plasma was the oxidizer. The PEALD growth rate was ~1.5 Å/cycle at a substrate temperature of 100 °C. Similarly prepared Al_2O_3 films were shown to be amorphous. [21]

After Al_2O_3 deposition, the surface was processed with a hydrogen plasma post-deposition treatment for 30 min at ~500 °C. The post-deposition hydrogen plasma was excited by a radio frequency (rf) source (100 W, 13.56 MHz) applied to a helical copper coil wrapped around a ~32 mm diameter quartz tube located ~25 cm above the sample. The chamber pressure was maintained at 100 mTorr with a constant gas flow of 20 sccm controlled by a throttle valve in front of the turbo pump.

The hole accumulation layer and the band bending of the diamond surface region was further corroborated using the binding energy of the C 1s core-level. The *in situ* XPS measurements were performed after each process step using a monochromated Al K_α X-ray source (hν = 1486.6 eV) with a bandwidth of 0.2 eV and a R3000 Scienta analyzer with a resolution of 0.1 eV. All core level spectra were recorded with a 0.05 eV step and the peak positions can be resolved to ~±0.05 eV by curve fitting.

The method proposed by Waldrop and Grant, [23] and Kraut *et al.* was used [24] for determining the valence band offset (VBO). The method is represented in the following equation:

$$\Delta E_V = (E_{CL} - E_V)_{Diamond} - (E_{CL} - E_V)_{Al_2O_3} - \Delta E_{CL} \text{ , (3.1)}$$

where ΔE_V represents the VBO; E_{CL} is the binding energy of the XPS core level; E_V is the valence band maximum (VBM); $(E_{CL}\text{-}E_V)_{Diamond}$ or $(E_{CL}\text{-}E_V)_{Al2O3}$ are the binding energy difference from the VBM to the respective core level; and ΔE_{CL} is the binding energy difference between the diamond and Al_2O_3 core levels measured at the interface ($E_{CL}^{C\ 1s}$ - $E_{CL}^{Al\ 2p}$).

The surface conductivity was characterized on 4×4 mm^2 type IIa undoped single crystalline diamond (100) substrates by measuring the diagonal resistance and the position of the corresponding C 1s core level. The distance between the two probes was ~5.5 mm. A small piece of gold foil was used under each probe tip to increase the contact area.

3.4 Results

3.4.1 PEALD Al_2O_3 deposition and hydrogen plasma treatment

For the H-terminated diamond surface after air exposure, the C 1s core level binding energy was measured at 284.1 eV. The O 1s core level showed features at 530.4 eV and 532.1 eV, which may originate from C-O bonds and adsorbates, respectively. After deposition of ~1 nm Al_2O_3 on boron doped diamond, the Al 2p core level was clearly observed at 73.7 eV, indicating that a thin Al_2O_3 layer was successfully formed on the diamond. However, the C 1s peak shifted to a higher binding energy of 285.1 eV, indicating a transition from upward band bending to downward band bending and a reduction of the surface hole accumulation density. After hydrogen plasma, the C 1s binding energy was restored to the same level as the conductive diamond surface, while the Al 2p and O 1s core levels shifted to lower binding energy by 1.7 eV and 1.5 eV,

respectively. We note that while H-diffusion may occur through the thin film and weak points, the XPS results indicate the surface is uniformly affected. With the deposition of an additional ~2 nm Al_2O_3, the C 1s remained at 284.1 eV, which is characteristic of the surface conductive state. The C 1s peak was not affected by further Al_2O_3 deposition.

With the application of a hydrogen plasma to the 20 nm Al_2O_3 layer, the Al 2p peak was fit with two peaks at 73.8 eV and 75.1 eV. The double peak was ascribed to Al_2O_3 layers at different depths. This result indicates that the hydrogen plasma treatment affected the surface of the Al_2O_3 layer. Evidently at different depths the Al_2O_3 layers had different levels of included charge. Fig. 3.1 shows the C 1s, Al 2p and O1s core levels of the (100) B-doped diamond surface after each process. The XPS core level binding energies are summarized in Table 3.1.

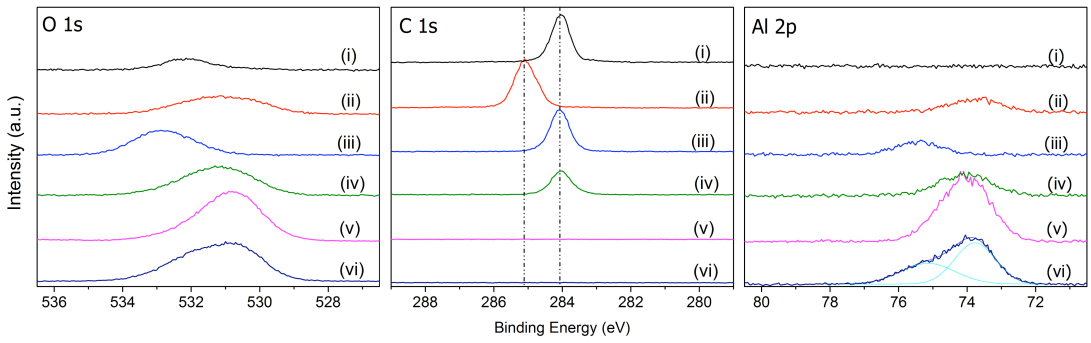

Figure 3.1 The respective XPS scans of the O 1s, C 1s and Al 2p core levels of (i) H-terminated diamond surface with air exposure, (ii) after 1 nm Al_2O_3 deposition, (iii) 500 °C H-plasma treatment, (iv) after 2 nm Al_2O_3 deposition, (v) after 20 nm Al_2O_3 deposition, and (vi) 500 °C H-plasma treatment. (For different elements, the intensity scales are adjusted for better visibility.)

TABLE 3.1 XPS of C 1s, Al 2p and O 1s core levels results for boron-doped diamond. All values are in units of eV and have an uncertainty of ±0.1 eV.

Process	C 1s	O 1s	Al 2p
H-plasma & Air exposure	284.1	530.6 & 532.1	--
1 nm Al_2O_3 deposition	285.1	531.1	73.7
H-plasma	284.1	532.6	75.4
2 nm Al_2O_3 deposition	284.0	521.2	74.1
20 nm Al_2O_3 deposition	--	530.6 &531.4	74.1
H-plasma	--	530.4 & 531.5	73.8 & 75.1

A control experiment was carried out to establish the necessity of the ambient exposure before dielectric layer deposition. A hydrogen plasma process at 500 °C was applied to hydrogenated undoped diamond to remove air-induced adsorbates without destroying the H-termination. After the *in situ* 500 °C, hydrogen plasma process, the C 1s core level shifted from 284.0 eV to 284.2 eV, indicating a change in the band bending which is presumed to correspond to the removal of air-induced surface conductivity. After 2 nm Al_2O_3 deposition, the C 1s shifted to 285.0 eV. A hydrogen plasma post-deposition process was able to restore the C 1s core level to 284.0 eV. This indicates that air induced adsorbates are not necessary to achieve the surface conductivity of the H-terminated diamond/Al_2O_3 structure.

3.4.2 Correlation of binding energy and surface resistance

Fig. 3.2 shows the C 1s core level binding energy and the surface resistance of the 4×4 mm^2 undoped diamond after each process. Initially, the H-terminated diamond surface after air exposure showed a surface resistance of ~30 kΩ which is consistent with the formation of a surface conductive layer. [25] The corresponding C 1s core level was measured at 284.1 eV. We have observed a small variation of ±0.1 eV in the C 1s core level binding energy of the H-terminated diamond surface with air-induced adsorbates. This variation may relate to the bulk Fermi level of the different diamond substrates. After the first PEALD Al_2O_3 deposition, which employed an oxygen plasma, the surface resistance increased to ~3 MΩ, and the C 1s core level shifted to a higher binding energy of 286.3 eV, indicating removal of the upward band bending and the surface hole accumulation layer. With hydrogen plasma treatment, the C 1s core level was restored to 284.1 eV, and the diagonal surface resistance decreased to ~20 kΩ. The hydrogen plasma process was able to restore the upward band bending that was apparently removed during the oxygen plasma process. With further PEALD Al_2O_3 deposition, the C 1s core level was not affected, and the surface conductivity was not obviously degraded.

3.4.3 Plasma effects

The oxygen coverage was estimated from the XPS spectra shown in Fig. 3.3, using the following equation: [26]

$$\Theta_O = \frac{I_O}{S_O} / \frac{I_C}{S_C} \times \sum_{n=0}^{\infty} exp\left[\frac{-n*d_{Diamond}}{\lambda_{Diamond}*cos(\varphi)}\right], \quad (3.2)$$

where Θ_O, the coverage in monolayers (ML), is the number of absorbed O atoms per unit area (atoms/cm^2) divided by the number of surface C atoms per unit area (atoms/cm^2). I_O and I_C are the integrated intensities of the O 1s and C 1s peaks from Fig. 3.3. The S_O and S_C are the atomic sensitivity factors for the O 1s and C 1s photoelectrons; $d_{Diamond}$ is the spacing between two (100) planes, which is 3.57 Å. $\lambda_{Diamond} \approx 18.9$ Å is the inelastic mean free path of C 1s electrons with kinetic energies of ~1200 eV; [27] φ is the angle between the normal direction and the XPS energy analyzer, which is 0º for this setup.

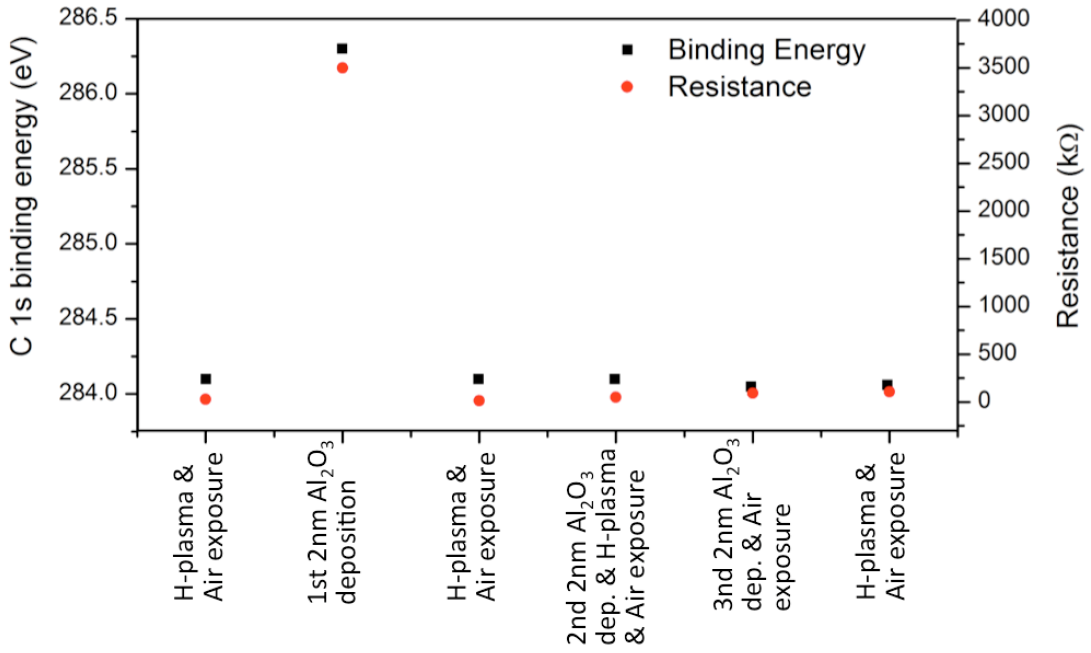

Figure 3.2 The C 1s binding energy and resistance of the diamond surface for the different process steps.

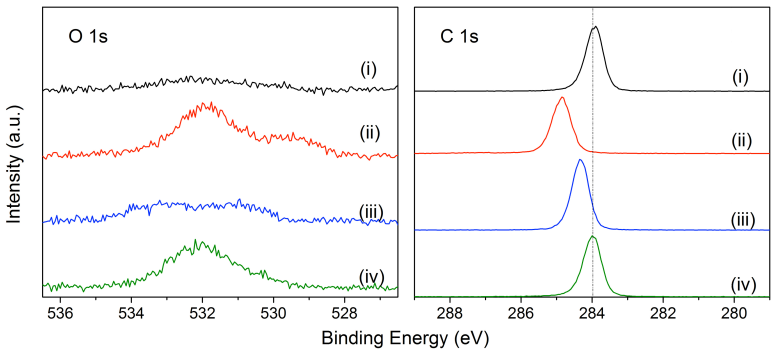

Figure 3.3 XPS scans for O 1s and C 1s core levels of (i) H-terminated diamond surface with air exposure, (ii) after oxygen plasma treatment, (iii) after hydrogen plasma treatment and (iv) air exposure. (For different elements, the intensity scales are adjusted for better visibility.)

To determine the effects related to oxygen or hydrogen plasma, the processes were successively applied to an H-terminated undoped diamond surface. The oxygen plasma used the chamber for PEALD Al_2O_3 deposition. The oxygen coverage increased from 0.15 ML for an atmosphere exposed H-terminated diamond surface to 0.55 ML after oxygen plasma. The C 1s core level shifted from 283.9 eV for the atmosphere exposed H-terminated surface to 284.3 eV, and the diagonal resistance increased to > 1 MΩ. The surface conductivity was apparently destroyed by the oxygen plasma process as reported previously. [22] A 500 °C hydrogen plasma treatment identical to that used in the post-deposition treatment was then applied to the air-exposed oxidized surface. A fraction of the oxygen was removed, and the oxygen coverage decreased to ~0.25 ML. The surface conductivity was restored as indicated by the C 1s core level which shifted to 284.0 eV and the diagonal resistance which was reduced to 31.7 kΩ, a value within the range for surface conductive diamond. The hydrogen plasma process was able to remove

a fraction of the oxygen atoms at the diamond surface and restore the surface conductivity.

3.4.4 Oxide charge state

This section addresses the band shifts that occur in the oxide after various processing steps. The presumption is that charge in the oxide is changed due to diffusion of atoms or molecules into/out of the dielectric layer or due to changing the charge state of diffused species or defects.

For an H-terminated diamond surface with a thin (~2 nm) layer of Al_2O_3 and 500 °C hydrogen plasma treatment, further PEALD Al_2O_3 deposition did not change the C 1s core level. However, with annealing at 500 °C, the Al 2p and O 1s core levels shifted 0.6 eV together to higher binding energy, indicating a downward band shifting of the oxide layer. This result suggests the charge induced by the oxygen plasma could be removed by annealing to 500 °C. With a further 500 °C hydrogen plasma process, the Al 2p and O 1s core levels shifted another 0.6 eV towards higher binding energy further increasing the downward band shifting. The results of the Al 2p, C 1s and O 1s core levels are shown in Fig. 3.4. The oxygen plasma and hydrogen plasma processes have apparently induced opposite charge into the oxide layer, which resulted in different band shifting.

We now consider the effect of a 500 °C H-plasma process followed by a 500 °C anneal. A diamond surface with an 8 nm Al_2O_3 layer was processed with a 500 °C H-plasma. The C 1s, O 1s and Al 2p core levels are shown in Fig. 3.5. After the 30 min 500 °C anneal process, the C 1s was maintained at ~283.9 eV indicating surface

conductivity. The O 1s and Al 2p core levels were not affected by the anneal indicating that charges in the oxide layer induced by hydrogen plasma were not affected by the anneal process. The anneal results established that the hydrogen plasma processed interface was apparently thermally stable at 500 °C. This is a notable difference from an air exposed, H-terminated diamond surface.

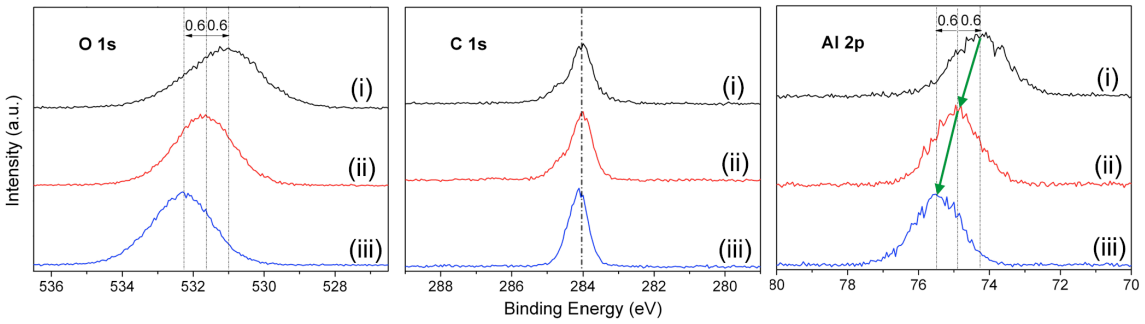

Figure 3.4 XPS scans of a diamond surface with a 2 nm layer of Al_2O_3 and hydrogen plasma treatment, showing the O1s, C 1s and Al 2p core levels after (i) an additional 2nm PEALD Al_2O_3 deposition (this surface is essentially the same as scan (iv) in Fig. 1), (ii) 500 °C vacuum anneal, and (iii) 500 °C hydrogen plasma process. (For different elements, the intensity scales are adjusted for better visibility.)

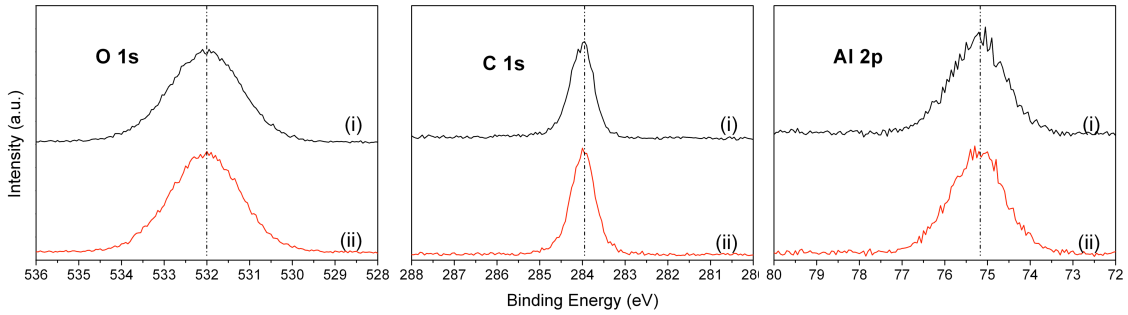

Figure 3.5 XPS scans of a diamond surface with a thin layer of Al_2O_3 ~8 nm and hydrogen plasma treatment, showing the O1s, C 1s and Al 2p core levels (i) before and (ii)

after thermal anneal at 500 °C. (For different elements, the intensity scales are adjusted for better visibility.)

3.5 Discussion

3.5.1 Interface model

An interface layer is used to explain the effects of the first and second PEALD Al_2O_3 deposition on the diamond surface conductivity, and post-deposition hydrogen plasma treatment. The effect of the initial H-termination and air exposure was apparently removed by the oxygen plasma during the PEALD process. With post-deposition hydrogen plasma treatment, the surface conductivity is restored. Presumably, hydrogen atoms can diffuse and incorporate into the diamond/Al_2O_3 interface to modify the interface, such that electron transfer is promoted from the diamond valence band into the interface layers. Within this model, the interface layer is charged, as indicated by the large shifts of the C 1s and Al 2p core levels. During the following PEALD process, the interface layer is apparently protected by the initial dielectric layers, and the charge transfer layers are not destroyed by the oxygen plasma during the further PEALD cycles.

The air exposure process is apparently not necessary to obtain surface conductivity in the H-terminated diamond/Al_2O_3 structure, as indicated by the results in section A. This is consistent with the results of Kawarada *et al.* that showed surface hole accumulation after Al_2O_3 ALD on a diamond surface preheated to 450 °C. In the post-deposition hydrogen plasma treatment, hydrogen atoms may form interface bonding similar to that of ALD Al_2O_3 on diamond where H_2O is used as oxidant.

3.5.2 Band alignment schematics

For application as an FET, it is necessary to obtain interface carrier confinement properties, which are determined by the band offsets. According to Fig. 3.4, oxygen plasma induced charge resulted in a 0.6 eV shift of the Al 2p core level towards lower binding energy. The VBO between as-grown Al_2O_3 and diamond was determined to be 2.7 eV by using Eq. (3.1) and taking account of the plasma effects (i.e. 0.6 eV shift observed after thermal annealing). The value of $(E_{CL}\text{-}E_V)_{Al2O3}$ was 70.6±0.1 eV [21] and $(E_{CL}\text{-}E_V)_{Diamond}$ was 284.1±0.1 eV. The diamond value was based on the assumption that the VBM is at the Fermi level for the surface conductive state. This band offset value is consistent with other reported results. [28] The band gaps of Al_2O_3 and diamond (5.47 eV) are necessary to calculate the conduction band offset (CBO). A previous study from our group reported the band gap of PEALD Al_2O_3 as 6.7 ± 0.1 eV, [21] which was determined from the energy loss spectrum associated with the XPS O 1s core level. Using 6.7 eV as the band gap of the Al_2O_3 films, the Al_2O_3 CBM is calculated to be 1.5 eV below the diamond CBM. The deduced band alignment diagram of Al_2O_3 on diamond is shown in Fig. 3.6(ii). The diagram shows that Al_2O_3 is able to confine holes but fails to confine electrons for surface conductive diamond.

Considering a charged interface layer and accounting for the effects of hydrogen and oxygen plasma, the band diagram and charge transfer for each process step are summarized in Fig. 3.6. In Fig. 3.6(i), for air-exposed, H-terminated diamond, electrons transfer from the valence band into the adsorbate layer, leaving an equal density of holes in the diamond valence band.

After a thin PEALD Al_2O_3 layer, the diamond upward band bending and the hole accumulation was reduced, resulting in the loss of surface conductivity, as shown in Fig. 3.6(ii). Furthermore, during PEALD, the oxygen plasma process introduces a concentration of defects or interstitial oxygen atoms, which act as electron traps or acceptors in the oxide layer. [21][29] These defects are compensated by ionized impurities or defects in the interface layer. This charge/dipole layer leads to an upward band shift across the interface layer, as shown in Fig. 3.5(ii). An anneal to 500 °C reduces the upward band shift, which may be due to diffusion and desorption of excess oxygen.

The charge distribution after the post deposition 500 °C hydrogen plasma treatment is shown in Fig. 3.6(iii). The hydrogen plasma process modifies the interface layer and restores the surface hole accumulation. Electron transfer from diamond into the interface layer results in a negatively charged interface layer. The holes and electrons at the interface result in upward band bending of the diamond valence band. Moreover, a large downward shift of the oxide core levels is observed. A 500 °C anneal does not reduce this downward band shift. Evidently, the hydrogen plasma process affects the oxide layer oppositely compared to an oxygen plasma. A possible explanation is that the hydrogen plasma introduces donor-like defects into the oxide near the interface layer. These defects contribute negative charge into the interface layer and positively charged donor states contribute to a dipole layer that accounts for the shift of the Al_2O_3 bands. It is notable that this configuration is stable during a 500 °C anneal indicating that the diamond/Al_2O_3 interface is more thermally stable compared to the charges trapped in air-induced adsorbates on diamond.

After additional PEALD Al_2O_3, the donor-like defects induced by the hydrogen plasma are removed and replaced with acceptor-like defects. Also the negative charges that compensate the donor-like defects are removed and replaced by positively charged compensating acceptor-like defects. This resulted in a 1.2 eV shift of the Al 2p core level towards lower binding energy. However, the C 1s core level did not change. Apparently the initial Al_2O_3 layers prevent interface reactions during the oxygen plasma process. The conductivity of the diamond surface may slightly degrade due to the changes of the charge transfer state within the oxide and interface layers. The charge configuration and band alignment after additional PEALD Al_2O_3 deposition is presented in Fig. 3.6(iv).

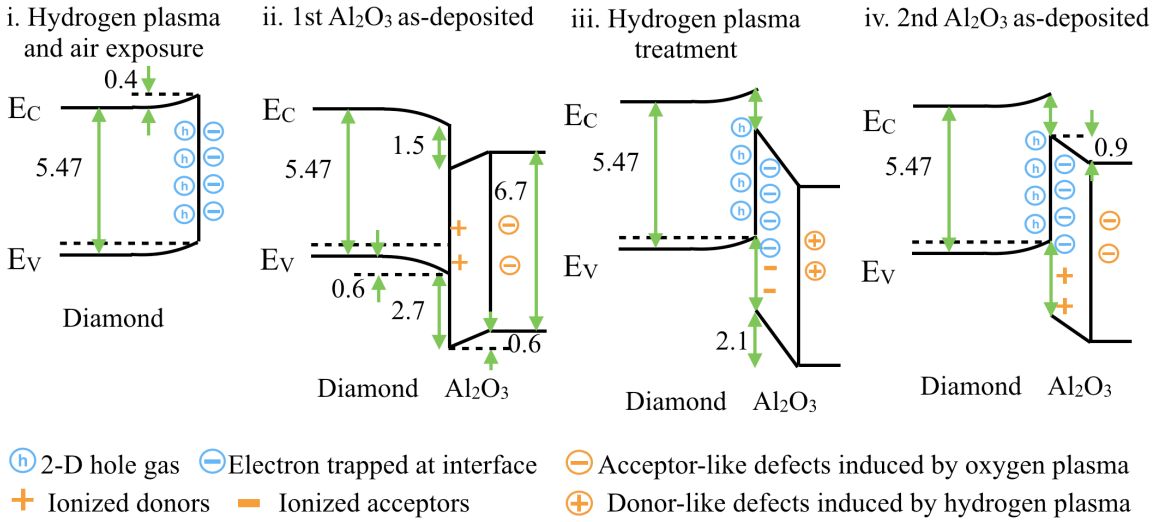

Figure 3.6 Interface band diagrams of Al_2O_3 on diamond showing band bending and possible charged states distributions after each process: (i) hydrogen terminated diamond with air exposure, (ii) 1st PEALD Al_2O_3 deposition ~1 nm, (iii) hydrogen plasma treatment at 500 °C and (iv) 2nd PEALD Al_2O_3 deposition ~2 nm. The charges in the schematic diagram indicate their spatial position, not their energy relative to the band gap.

3.6 Conclusion

In this research, surface conductive diamond was achieved with Al_2O_3 employed as a dielectric layer deposited by PEALD with a post-deposition hydrogen plasma treatment. The change of surface conductivity is monitored *in situ* using the C 1s core level and *ex situ* by electrical measurements. The VBO between Al_2O_3 and diamond is determined to be 2.7 eV, and the CBO is determined to be -1.5 eV. The Al_2O_3 is able to confine holes for surface conductive diamond, enabling a diamond based FET. However, Al_2O_3 is not able to confine electrons on H-terminated diamond. Post-deposition hydrogen plasma treatment significantly affects the surface conductivity of diamond by changing the interface structure and interface charge state. Moreover the interface band alignment is thermally stable during an anneal at 500 °C suggesting a charge configuration that differs from air exposed H-terminated diamond. It is proposed that a charged interface layer plays a critical role in the surface conductivity of diamond and the band alignment of the diamond/ Al_2O_3 interface.

Acknowledgments

This research was supported by a grant from MIT -Lincoln Laboratories and the NSF through grant DMR - 1710551. We gratefully acknowledge helpful discussion from Dr. Michael Geis, Dr. Mark Hollis and Dr. Travis Wade of MIT-Lincoln Laboratories and Professor Timothy Grotjohn of Michigan State University.

References

[1] J.Y. Tsao, S. Chowdhury, M.A. Hollis, D. Jena, N.M. Johnson, K.A. Jones, R.J. Kaplar, S. Rajan, C.G. Van de Walle, E. Bellotti, C.L. Chua, R. Collazo, M.E. Coltrin, J.A. Cooper, K.R. Evans, S. Graham, T.A. Grotjohn, E.R. Heller, M. Higashiwaki, M.S. Islam, P.W. Juodawlkis, M.A. Khan, A.D. Koehler, J.H. Leach, U.K. Mishra, R.J. Nemanich, R.C.N. Pilawa-Podgurski, J.B. Shealy, Z. Sitar, M.J. Tadjer, A.F.Witulski, M. Wraback, and J.A. Simmons, Advanced Electronic Materials **4**, 1600501 (2018).

[2] N. Fujimori, H. Nakahata, and T. Imai, Japanese Journal of Applied Physics **29**, 824 (1990).

[3] H. Sato and M. Kasu, Diamond and Related Materials **31**, 47 (2013).

[4] C. Pietzka, J. Scharpf, M. Fikry, D. Heinz, K. Forghani, T. Meisch, Diemant, R.J. Behm, J. Bernhard, J. Biskupek, U. Kaiser, F. Scholz, and E. Kohn, Journal of Applied Physics **114**, 114503 (2013).

[5] S.A.O. Russell, S. Sharabi, A. Tallaire, and D.A.J. Moran, IEEE Electron Device Letters **33**, 1471 (2012).

[6] H. Kawarada, Japanese Journal of Applied Physics **51**, 090111 (2012).

[7] C. Verona, W. Ciccognani, S. Colangeli, E. Limiti, M. Marinelli, and G. Verona-Rinati, Journal of Applied Physics **120**, 025104 (2016).

[8] D. Takeuchi, M. Riedel, J. Ristein, and L. Ley, Physical Review B **68**, 41304 (2003).

[9] M.T. Edmonds, C.I. Pakes, S. Mammadov, W. Zhang, A. Tadich, J. Ristein, and L. Ley, Applied Physics Letters **98**, 102101 (2011).

[10] M. Riedel, J. Ristein, and L. Ley, Physical Review B **69**, 125338 (2004).

[11] M. Kasu, M. Kubovic, A. Aleksov, N. Teofilov, Y. Taniyasu, R. Sauer, E. Kohn, T. Makimoto, and N. Kobayashi, Diamond and Related Materials **13**, 226 (2004).

[12] A. Daicho, T. Saito, S. Kurihara, A. Hiraiwa, and H. Kawarada, Journal of Applied Physics **115**, 223711 (2014).

[13] M.W. Geis, Proceedings of the IEEE **79**, 669 (1991).

[14] K. Hirama, H. Sato, Y. Harada, H. Yamamoto, and M. Kasu, IEEE Electron Device Letters **33**, 1111 (2012).

[15] D. Kueck, P. Leber, A. Schmidt, G. Speranza, and E. Kohn, Diamond and Related Materials **19**, 932 (2010).

[16] J.W. Liu, M.Y. Liao, M. Imura, H. Oosato, E. Watanabe, and Y. Koide, Applied Physics Letters **102**, 112910 (2013).

[17] J.W. Liu, M.Y. Liao, M. Imura, H. Oosato, E. Watanabe, A. Tanaka, H. Iwai, and Y. Koide, Journal of Applied Physics **114**, 84108 (2013).

[18] S.A.O. Russell, L. Cao, D. Qi, A. Tallaire, K.G. Crawford, A.T.S. Wee, and D.A.J. Moran, Applied Physics Letters **103**, 202112 (2013).

[19] K.G. Crawford, L. Cao, D. Qi, A. Tallaire, E. Limiti, C. Verona, A.T.S. Wee, and D.A.J. Moran, Applied Physics Letters **108**, 42103 (2016).

[20] J.W. Lim and S.J. Yun, Electrochemical and Solid-State Letters **7**, 45 (2004).

[21] J. Yang, B.S. Eller, M. Kaur, and R.J. Nemanich, Journal of Vacuum Science & Technology A **32**, 21514 (2014).

[22] H. Nakahata, T. Imai and N. Fujimori, Proc. 2nd Int. Symp. Diamond Material, p.487 (1991).

[23] J.R. Waldrop and R.W. Grant, Applied Physics Letters **68**, 2879 (1996).

[24] E.A. Kraut, R.W. Grant, J.R. Waldrop, and S.P. Kowalczyk, Heterojunction Band Discontinuities: Physics and Device Applications, edited by F. Capasso and G. Margaritondo (Elsevier, New York, 1987).

[25] F. Maier, M. Riedel, B. Mantel, J. Ristein, and L. Ley, Physics Review Letters **85**, 3472 (2000).

[26] V.M. Bermudez, Journal of Applied Physics **80**, 1190 (1996).

[27] S. Tanuma, C.J. Powell, and D.R. Penn, Surface and Interface Analysis **43**, 689 (2011).

[28] J.W. Liu, M.Y. Liao, M. Imura, and Y. Koide, Applied Physics Letters **101**, 252108 (2012).

[29] Y. Yang, T. Sun, J. Shammas, M. Kaur, M. Hao, and R.J. Nemanich, Journal of Applied Physics **118**, 165310 (2015).

CHAPTER 4

SURFACE TRANSFER DOPING OF DIAMOND/MOO_3 WITH AN AL_2O_3 INTERFACE LAYER

4.1 Abstract

A thin layer of Al_2O_3 was employed as an interfacial layer between surface conductive hydrogen-terminated (H-terminated) diamond and MoO_3 to increase the distance between the hole accumulation layer in diamond and negatively charged states in the acceptor layer, and thus reduce the Coulomb scattering and increase the hole mobility. The valence band offsets are found to be 2.7 and 3.1 eV for Al_2O_3/H-terminated diamond and MoO_3/diamond, respectively. Compared to the H-terminated diamond/MoO_3 structure, a higher hole mobility was achieved with Al_2O_3 inserted as an interface layer. This work provides a strategy to achieve increased hole mobility of surface conductive diamond by using optimal interlayers with high electron affinity surface acceptor materials.

(In collaboration with Xingye Wang, Yichen Yao, Franz A. Koeck, and Robert J. Nemanich)

4.2 Introduction

Diamond is a promising candidate for high frequency and high-power electronic devices due to its high thermal conductivity, wide band gap, high carrier mobility and high-saturated drift velocity. A p-type surface conducting layer on diamond can be readily achieved by surface transfer doping, with the following properties: sheet

resistance of 5-20 kΩ/sq, hole density of 10^{12}-10^{13} cm^{-2} and hole mobility of 10-150 $cm^2/(V•s)$. [1] Surface transfer doping provides an alternative strategy to enable high power and high frequency diamond field effect transistor (FET) operation.

Hydrogen-terminated (H-terminated) diamond (Eg=5.47 eV) exhibits a negative electron affinity (NEA) of -1.1 to -1.3 eV. [2] Consequently, the valence band maximum (VBM) of the H-terminated diamond is ~4.3 eV below the vacuum level. Materials with sufficiently high electron affinity (χ>4.3 eV), such as MoO_3, V_2O_5, WO_3, could align with their conduction band minimum (CBM) below the VBM of H-terminated diamond. Electron transfer would then be energetically favorable from the diamond to the transition metal oxides. Compared with the air-exposed H-terminated surface, a higher hole concentration and lower sheet resistance may be achieved with high electron affinity metal oxides on H-terminated diamond. [3, 4]

While surface conductive diamond may be enabled by high electron affinity metal oxides, an intimate correlation is often observed between hole concentration and mobility where an increase in carrier concentration is associated with a mobility decrease or vice versa. [1] One possibility is that in the case of charge transfer doping, the negatively charged sites are not distributed homogenously in the oxide, but instead accumulate in a layer adjacent to the hole accumulation layer in the diamond. [5] Those negatively charged states give rise to Coulomb scattering in the hole accumulation layer. For bulk-doping in semiconductors, the scattering of free charge carriers at low temperatures is dominated by Coulomb scattering from ionized impurities. With the Brooks-Herring and Conwell-Weisskopf approximations, the mobility is described by [6]

$$\mu_I = \frac{8\sqrt{2}}{q^3}\left(\frac{k}{\pi}\right)^{\frac{3}{2}}\frac{\varepsilon_r^2 T^{3/2}}{(m^*)^{0.5} N_I f}, \qquad (4.1)$$

where k is the Boltzmann constant, q is the electron elementary charge, ε_r is the relative permittivity, m^* is the effective mass, N_I is the concentration of ionized impurities and f is the screening factor. The Coulomb scattering mechanism results in the carrier mobility being inversely proportional to the density of charged scattering centers. For charge transfer doping, the results from Hall effect measurement also confirm this. [5] As the amount of negatively charged states in the adsorbate layer is approximately equal to the hole sheet concentration in the diamond, an increase in the hole sheet concentration is associated with an increase of the negatively charged states in the adsorbate layer. Furthermore, the increased negatively charge concentration resulted in a reduction of the hole mobility which was attributed the Coulomb scattering. On the other hand, the potential of the charged scattering center v(r) is ~1/|r|. When the negatively charged states accumulate adjacent to the hole accumulation layer, the effect of Coulomb scattering is significant and limits the hole mobility.

We propose to employ a thin layer of Al_2O_3 as an interface layer between diamond and MoO_3 to increase the distance between the hole accumulation layer in diamond and the negatively charged states in the acceptor layer, and thus to reduce the Coulomb scattering and increase the hole mobility.

4.3 Experiment

The diamond substrates used in this study are 5×5 mm^2 type IIa chemical vapor deposited single crystalline undoped diamond (100) substrates. A hydrogen plasma treatment was applied to obtain H-terminated surface. The hydrogen plasma was performed with a microwave power of 1000 W, H_2 pressure of 50 Torr, a H_2 gas flow of

400 standard cubic centimeters per minute (sccm), and diamond substrate at ~800 °C for 15min.

The Al_2O_3 deposition was accomplished by remote PEALD. The precursor used was dimethylaluminum isoproxide (DMAI, $[(CH_3)_2AlOCH(CH_3)_2]_2$) and an O_2 plasma was used as the oxidizer. The DMAI bubbler was maintained at 90 °C to provide sufficient vapor pressure for PEALD deposition. The delivery line temperature was maintained at ~20 °C higher than that of the bubbler to prevent precursor condensation. The oxygen plasma was excited with 30 W rf power and a O_2 flow rate of 35 sccm. The growth rate was ~1.5 Å/cycle at a substrate temperature of 100 °C.

After Al_2O_3 deposition, the surface was processed with a hydrogen plasma post-deposition treatment for 30 min at ~500 °C. The hydrogen plasma was excited by a radio frequency (rf) input power of 100 W. The chamber pressure was maintained at 100 mTorr with a constant H_2 gas flow of 20 sccm controlled by a throttle valve in front of the turbo pump. Additional details are presented in our previous work. [7]

Molybdenum oxides were deposited in a reactive electron beam deposition (EBD) system, which has a base pressure of 1×10^{-8} Torr. Molybdenum pellets with a purity of 99.99% were evaporated using an e-beam. After deposition the substrates were transferred to a remote plasma enhance atomic layer deposition (PEALD) system and an O-plasma process was employed. The MoO_3 (+6) oxidation state was achieved using a 5 min oxygen plasma treatment at ambient temperature. The remote plasma was generated by 30 W rf excitation. The 100 mTorr oxygen pressure was maintained with a gas flow rate of 30 sccm. The oxidation state of molybdenum oxide is examined with XPS.

The hole accumulation layer is associated with upward band bending in the diamond near surface region. Consequently, the surface conducting state can be indicated by measuring the binding energy of the C 1s core level. After each process (Al_2O_3 deposition, hydrogen plasma, Mo deposition, oxygen plasma), the surface was characterized using *in situ* XPS, which employed a monochromated Al K_α X-ray source ($h\nu$ = 1486.6 eV) with a bandwidth of 0.2 eV and a R3000 Scienta analyzer with a resolution of 0.1 eV. All core level spectra were recorded with a 0.05 eV step, and the peak positions can be resolved to ~±0.05 eV by curve fitting.

Ex-situ Hall effect measurements were performed using an Ecopia HMS-3000 Hall measurement system. The diamond was mounted on a Van der Pauw-Hall probe. A ~0.5 mm^2 of gold foil was used under each probe tip to increase the contact area. The surface resistance, carrier density, and carrier mobility were measured with a 0.51 T permanent magnet at room temperature.

4.4 Results

4.4.1 Photoelectron spectroscopy (PES) characterization

Diamond samples using MoO_3 as acceptor layer were prepared with 0, 2 nm, and 4 nm Al_2O_3 interface layers. For the H-terminated diamond surface with air exposure, the C 1s core level was located at a characteristic position 284.1 eV, indicating the surface conductive state. [7] After 2 nm MoO_3 deposition by EBD, the Mo $3d_{3/2}$ and $3d_{5/2}$ core level binding energies corresponded to metallic molybdenum. After the oxygen plasma process, the Mo $3d_{3/2}$ and $3d_{5/2}$ core levels shifted to higher binding energies of 235.7 eV and 232.5 eV, indicating the Mo was in the +6 state. The C 1s core level was not affected

by the MoO_3 deposition. Fig. 4.1 shows the C 1s, O 1s, and Mo 3d core levels of the diamond surface after each process.

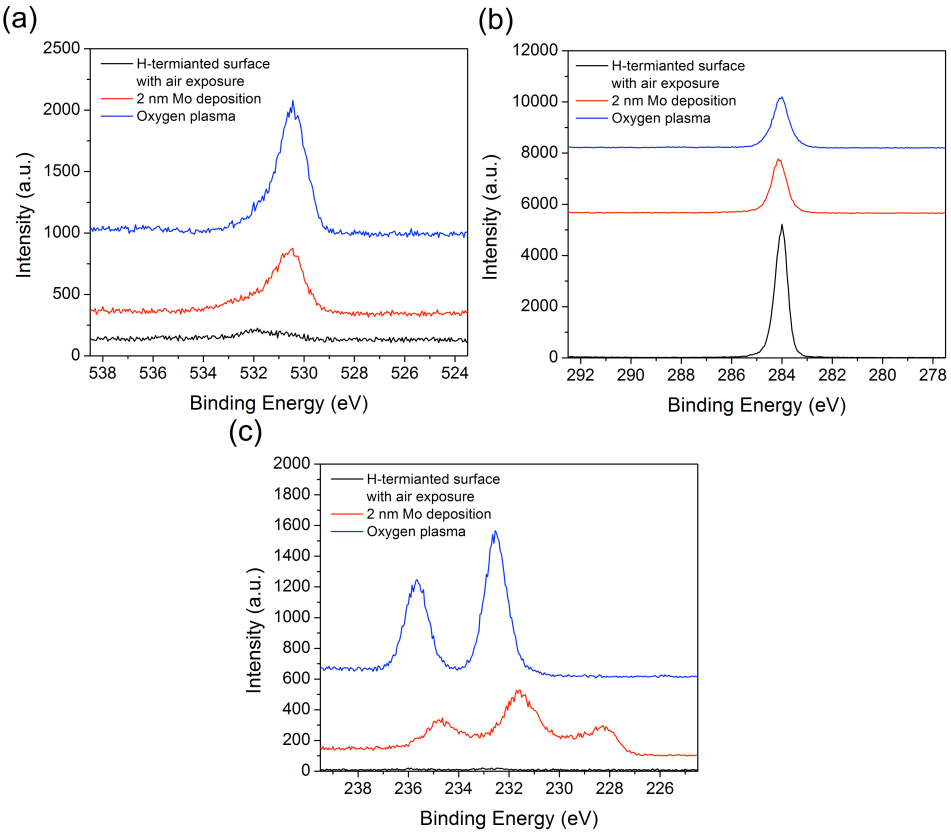

Figure 4.1 XPS scans of diamond/0 nm Al_2O_3/MoO_3 after each process, showing the (a) O 1s, (b) C 1s, and (c) Mo 3d core level peaks.

For the diamond samples that employed 2 nm Al_2O_3 interfacial layers, the C 1s core level shifted to higher binding energy after Al_2O_3 PEALD, as shown in Fig. 4.2. With a hydrogen plasma post-deposition treatment, the C 1s core level was restored to 284.0 eV, the surface conducting characteristic position, consistent with our previous study. [7] The Al 2p core level shifted 2.1 eV to a binding energy, indicating that the hydrogen plasma process not only restored the hole accumulation layer in diamond, but

also resulted in a negatively charged layer at the interface. The negatively charged interfacial layer, which was adjacent to the diamond hole accumulation layer, would induce the Coulomb scattering of the holes, limiting the hole mobility. After MoO_3 deposition, the Al 2p core levels shifted 0.9 eV to lower binding energy, indicating a reduced density of negative charges close to diamond surface. Apparently, the Coulomb scattering due to the negatively charged interfacial layer was reduced. The C 1s core level position of the diamond was not affected by the MoO_3 deposition, indicating the diamond surface remained conductive.

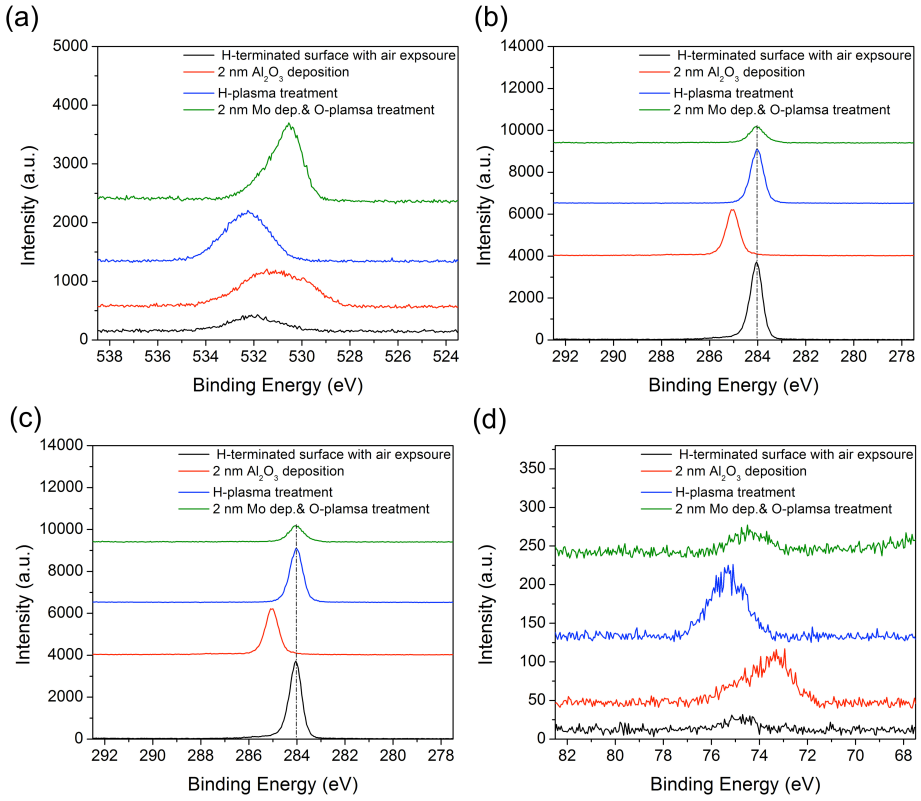

Figure 4.2 XPS scans of diamond/2 nm Al_2O_3/MoO_3 after each process, showing the (a) O 1s, (b) C 1s, (c) Mo 3d, and (d) Al 2p core level peaks.

For the diamond samples with a 4 nm Al_2O_3 interfacial layer, after hydrogen plasma treatment, the C 1s core level (measured at 284.2 eV) was not fully restored to the surface conducting value, as shown in Fig. 4.3. This may be due to the thicker Al_2O_3 layers which reduced the interaction of the hydrogen plasma and the diamond interface. With the deposition of 2 nm MoO_3 deposited, the C 1s core level shifted from 284.2 eV to 284.0 eV, indicating electrons transferred from diamond to the acceptor layer.

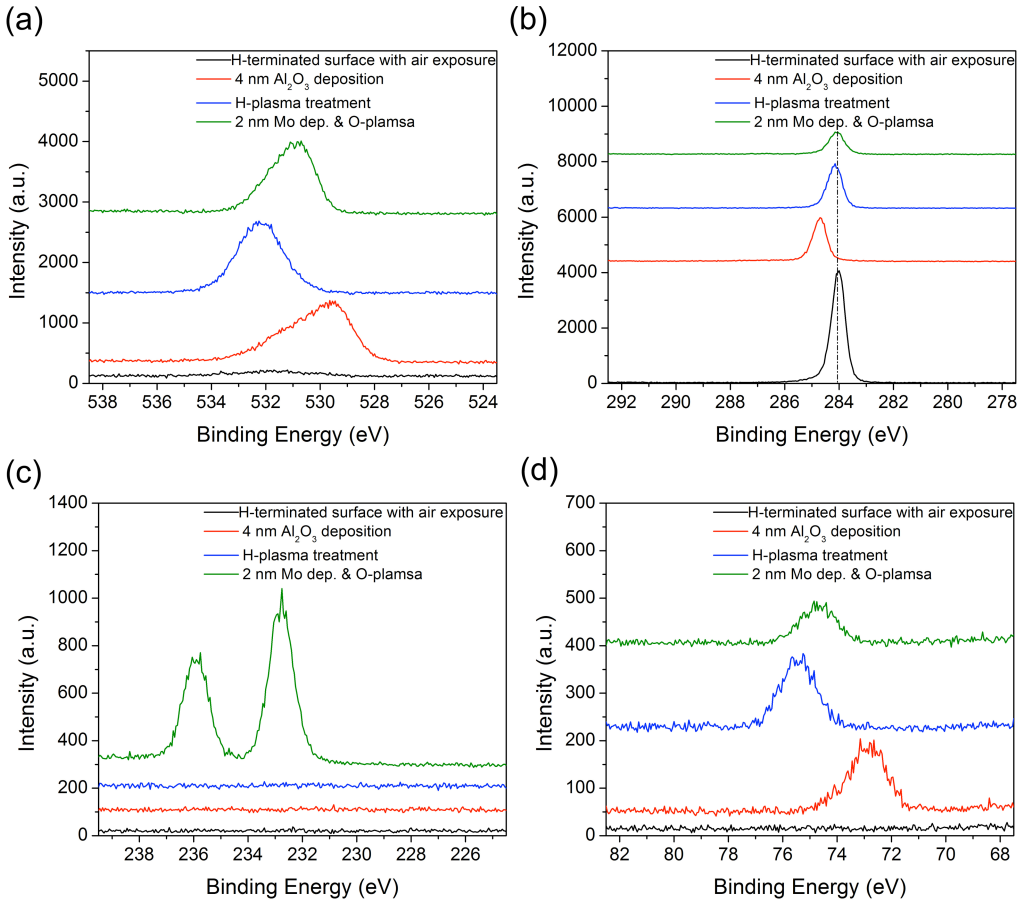

Fig. 4.3 XPS scans of diamond/4 nm Al_2O_3/MoO_3 after each process, showing the (a) O 1s, (b) C 1s, (c) Mo 3d, and (d) Al 2p core level peaks.

4.4.2 Hall electrical characterization

Table 4.1 summarizes the change of sheet resistance, hole concentration and hole mobility of H-terminated diamond with MoO_3 as acceptor layer and Al_2O_3 as an interface layer. For the sample without Al_2O_3, the surface conductivity of diamond was achieved with MoO_3 as an acceptor layer. After MoO_3 deposition and oxidation, the sheet resistance increased to 6.9 kΩ/sq, and remained under 10 kΩ/sq. The hole concentration remained the same as the H-terminated surface while the hole mobility decreased to 8.9 $cm^2/(Vs)$. For the samples with an Al_2O_3 interface layer, the surface conductivity was achieved with the diamond/Al_2O_3/MoO_3 structure. The sheet resistance increased similarly as without Al_2O_3 to 5.9 kΩ/sq and 14.0 kΩ/sq, and the hole concentration decreased to $9.4\times10^{12}/cm^2$ and $3.5\times10^{12}/cm^2$, for the sample with 2 nm and 4 nm Al_2O_3, respectively. The hole mobility increased significantly to >100 $cm^2/(Vs)$. For the different process steps, the change of sheet resistance, hole concentration and hole mobility for the different structures with processes are plotted in Fig. 4.4(a), and the hole concentration and mobility of the different structures are compared in Fig. 4.4(b).

TABLE 4.1 Hall measurement sheet resistance, carrier concentration and carrier mobility of diamond surfaces using MoO_3 as acceptor layer with 0, 2, and 4 nm Al_2O_3 interfacial layers.

Sample	Process	Sheet Resistance (kΩ/sq)	Carrier Concentration /cm^2	Carrier Mobility $cm^2/(Vs)$
0 nm Al_2O_3 interfacial layer	H-terminated surface	1.8	1.0×10^{14}	18.4
	After molybdenum dep.	3.6	1.3×10^{14}	13.5
	Oxidation by plasma	6.9	1.0×10^{14}	8.9

	H-terminated surface	2.3	7.0×10^{14}	3.94
2 nm Al_2O_3 interfacial layer	2 nm Al_2O_3 dep. & Hydrogen plasma	2.0	6.4×10^{14}	4.94
	Molybdenum dep. & Oxidation by plasma	6.2	9.4×10^{12}	100.7
	H-terminated surface	5.9	4.6×10^{13}	22.9
4 nm Al_2O_3 interfacial layer	4 nm Al_2O_3 dep. & Hydrogen plasma	11.5	6.7×10^{13}	8.1
	Molybdenum dep. & Oxidation by plasma	14.0	3.5×10^{12}	125.9

4.5 Discussion

4.5.1 Band alignment of H-terminated diamond/Al_2O_3/MoO_3

The valence band offset (ΔE_V) between diamond and Al_2O_3 can be calculated using the following equation: [8,9]

$$\Delta E_V = (E_{CL} - E_V)_{Diamond} - (E_{CL} - E_V)_{Al_2O_3} - \Delta E_{CL}, \quad (4.2)$$

where E_{CL} is the binding energy of the XPS core level; E_V is the valence band maximum (VBM); (E_{CL}-E_V) is the binding energy difference from the VBM to the respective core level; and ΔE_{CL} is the binding energy difference between the diamond and Al_2O_3 core levels measured at the interface ($E_{CL}^{C\ 1s}$ - $E_{CL}^{Al\ 2p}$). The measured value of $(E_{CL}\text{-}E_V)_{Al2O3}$ was 70.6±0.1 eV [10] and $(E_{CL}\text{-}E_V)_{Diamond}$ was 284.1±0.1 eV. The diamond value was based on the assumption that the VBM is at the Fermi level for the surface conductive state. The VBO between Al_2O_3 and diamond was determined to be 2.6 eV using Eq. (1), taking account of band bending of 1.2 eV, which resulted from a concentration of defects or interstitial oxygen atoms in Al_2O_3 introduced by oxygen plasma. The ΔE_V between

diamond and MoO_3 was calculated to be 3.1 eV by using Eq. (1), where $(E_{CL}\text{-}E_V)_{MoO3}$ was 229.5 eV as the Fermi level of MoO_3 is located close to its conduction band minimum (CBM).

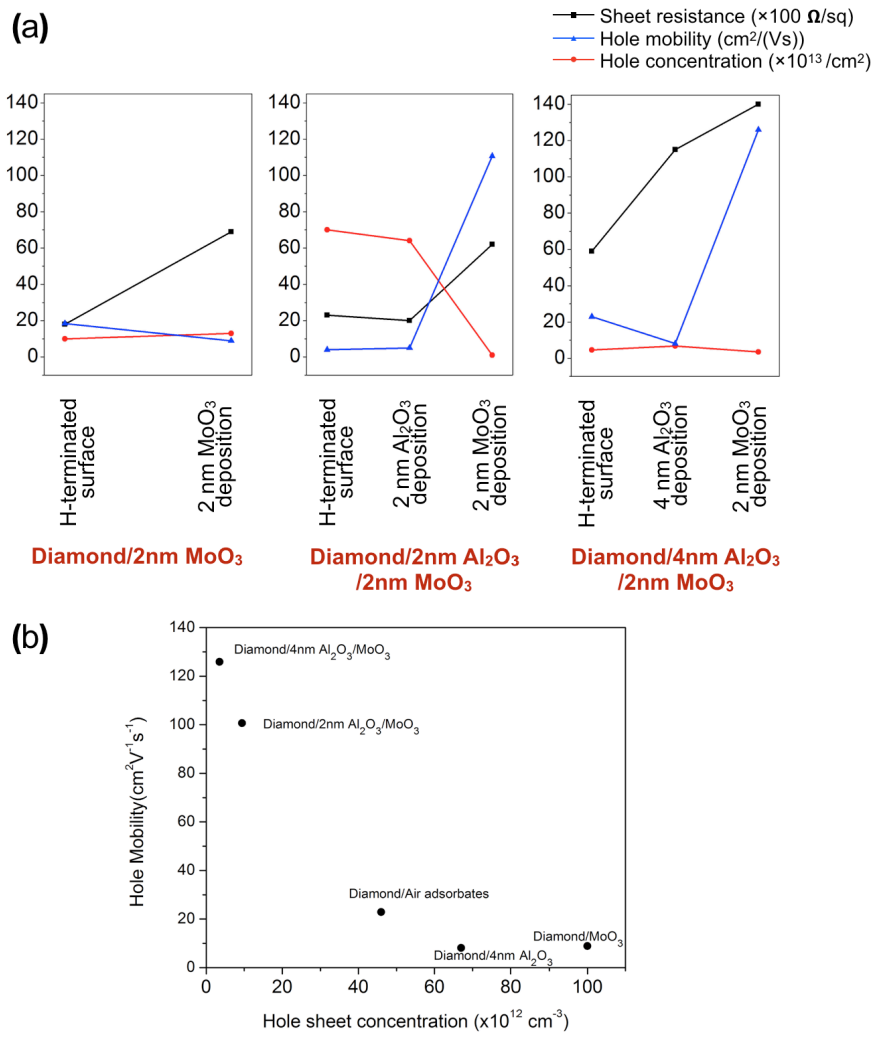

Figure 4.4 (a) The change of sheet resistance, hole concentration and hole mobility with processes for diamond/MoO_3 with 0/2/4 nm Al_2O_3 interfacial layers. (b) The hole concentration and mobility of different structures.

The band diagrams of diamond/Al_2O_3 and diamond/Al_2O_3/MoO_3 are shown in Fig. 4.5. The charge at the H-terminated diamond and Al_2O_3 interface is represented by a decrease of the band. After MoO_3 is deposited on Al_2O_3, the Al 2p core level shifted to lower binding energy. The distribution of negative charges changed and a fraction of negative charges originally close to diamond interface transferred into the MoO_3.

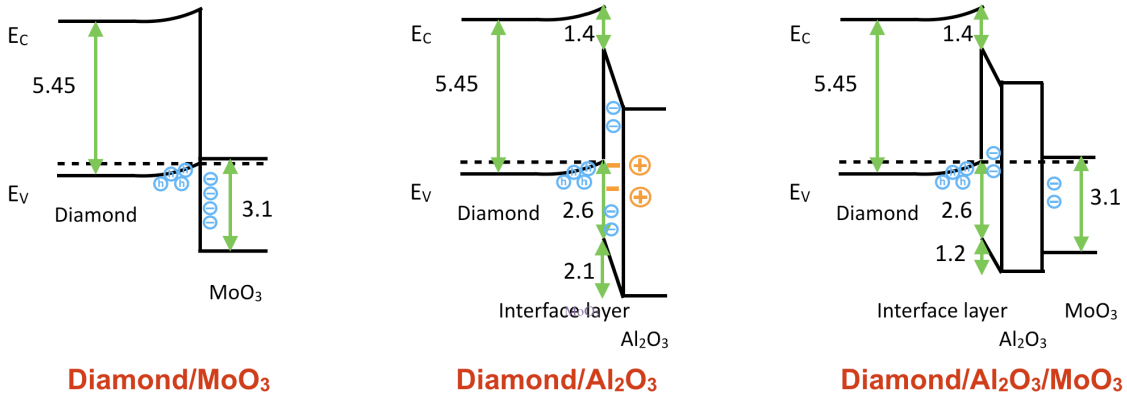

Fig. 4.5 The band diagrams of diamond/MoO_3 and diamond/Al_2O_3/MoO_3 before and after MoO_3 deposition.

4.5.2 Effect of the Al_2O_3 interfacial layer thickness

According to the position of the Al 2p core level, the distribution of negative charge changes with the increase of the Al_2O_3 layer thickness. As the charge transfer doping is driven by the energy level difference between the diamond VBM and the acceptor level, the sheet concentration and mobility of the hole accumulation layer are related to the oxide electron affinity. A higher electron affinity of the acceptor material corresponds to a larger energy difference with the diamond valence band. Evidently, high electron affinity oxides on diamond result in a higher sheet hole concentration and a

lower hole mobility. Without the Al_2O_3 interfacial layer, the sheet concentration and mobility of the hole accumulation layer achieved with MoO_3, are mainly determined by its electron affinity. With a thin Al_2O_3 interfacial layer, the MoO_3 acts as an additional acceptor layer, where a fraction of the negative charges are located at the diamond/Al_2O_3 interface and additional negative charges are distributed in the MoO_3.

When the Al_2O_3 is thick enough that it is the same as using Al_2O_3 as passivation layer, there is a highly negatively charged interfacial layer and the hole mobility is limited by Coulomb scattering.

For the Al_2O_3 thicknesses measured from 0 to 4 nm, the hole concentration decreases and mobility increases. The decrease of hole concentration is related to the increase of the distance between the diamond and acceptor layer, while the energy difference between diamond and MoO_3 is unchanged, which is determined by the oxide work function. If the charge distribution is simplified to all holes accumulated at the interface of diamond/ Al_2O_3 and all negative charged states accumulated at the interface of Al_2O_3/ MoO_3, the hole concentration in diamond can be estimated by an ideal capacitor, as following:

$$Q = CV = \frac{\varepsilon A}{d} V, \qquad (4.3)$$

where C is the capacitance, ε is the dielectric constant, A is the area of diamond and Al_2O_3 interface, d is the thickness of Al_2O_3, and V is the energy difference between diamond and MoO_3 vacuum level. In this case, an increase of Al_2O_3 thickness results in a decrease of hole concentration. Although in the diamond/Al_2O_3/MoO_3 structure, the negatively charged states was distributed between the diamond/Al_2O_3 interface and the MoO_3, the increase of the distance between diamond and MoO_3 results in a decrease of

the driving force for charge transfer doping between diamond and MoO_3 and lower charge transfer efficiency.

The increase of hole mobility may be attributed to reduced Coulomb scattering which results from the increase of the distance between the hole accumulation layer and the negative charged states. With the increase of the thickness of Al_2O_3 layer, at a certain point, the hole concentration is expected to increase and hole mobility is supposed to decrease, so that the interface turns into the case of Al_2O_3 as a passivation layer.

4.6 Conclusion

In this work, surface conductivity was achieved with the diamond/Al_2O_3/MoO_3 structure. The VBO for Al_2O_3/H-terminated diamond and MoO_3/diamond was found to be 2.6 and 3.1 eV, respectively. The diamond sheet resistance and the hole concentration and mobility were characterized for diamond/MoO_3 with Al_2O_3 interfacial layers of different thickness, 0, 2, 4 nm. By combining two oxides (Al_2O_3 and MoO_3), the hole mobility and concentration were modulated by altering the thickness of the interfacial layer. The mobility of the hole accumulation layer was improved by inserting an interfacial layer which was ascribed to a reduction of Coulomb scattering on diamond.

Acknowledgments

This research was supported by a grant from MIT -Lincoln Laboratories and the NSF through grant DMR - 1710551.

References

[1] C. Verona, W. Ciccognani, S. Colangeli, E. Limiti, M. Marinelli, and G. Verona-Rinati, Journal of Applied Physics **120**, 025104 (2016).

[2] D. Takeuchi, H. Kato, G. S. Ri, T. Yamada, P. R. Vinod, D. Hwang, C. E. Nebel, H. Okushi, and S. Yamasaki, Applied Physics Letters **86**, 152103 (2005).

[3] S.A.O. Russell, L. Cao, D. Qi, A. Tallaire, K.G. Crawford, A.T.S. Wee, and D.A.J. Moran, Applied Physics Letters **103**, 202112 (2013).

[4] K.G. Crawford, L. Cao, D. Qi, A. Tallaire, E. Limiti, C. Verona, A.T.S. Wee, and D.A.J. Moran, Applied Physics Letters **108**, 42103 (2016).

[5] C.E. Nebel, New Diamond and Frontier Carbon Technology **15**, 5 (2005).

[6] K. Somogyi, Diamond and Related Materials **11**, 686 (2002).

[7] Y.Yang, F.A. Koeck, M. Dutta, X. Wang, S. Chowdhury, and R.J. Nemanich, Journal of Applied Physcis **122**, 155304 (2017).

[8] J.R. Waldrop and R.W. Grant, Applied Physics Letters **68**, 2879 (1996).

[9] E.A. Kraut, R.W. Grant, J.R. Waldrop, and S.P. Kowalczyk, Heterojunction Band Discontinuities: Physics and Device Applications, edited by F. Capasso and G. Margaritondo (Elsevier, New York, 1987).

[10] J. Yang, B.S. Eller, M. Kaur, and R.J. Nemanich, Journal of Vacuum Science & Technology A **32**, 21514 (2014).

CHAPTER 5

ELECTRON AFFINITY OF CUBIC BORON NITRIDE TERMINATED WITH VANADIUM OXIDE

5.1 Abstract

A thermally stable negative electron affinity (NEA) for a cubic boron nitride (c-BN) surface with vanadium-oxide-termination is achieved, and its electronic structure was analyzed with *in-situ* photoelectron spectroscopy. The c-BN films were prepared by electron cyclotron resonance plasma-enhanced chemical vapor deposition (ECR-PECVD) employing BF_3 and N_2 as precursors. Vanadium layers of ~0.1 and 0.5 nm thickness were deposited on the c-BN surface in an electron beam deposition system. Oxidation of the metal layer was achieved by an oxygen plasma treatment. After 650 ºC thermal annealing, the vanadium oxide on the c-BN surface was determined to be VO_2, and the surfaces were found to be thermally stable, exhibiting an NEA. In comparison, the oxygen-terminated c-BN surface, where B_2O_3 was detected, showed a positive electron affinity (PEA) of ~1.2 eV. The B_2O_3 evidently acts as a negatively charged layer introducing a surface dipole directed into the c-BN. Through the interaction of VO_2 with the B_2O_3 layer, a B-O-V layer structure would contribute a dipole between the O and V layers with the positive side facing vacuum. The lower enthalpy of formation for B_2O_3 is favorable for the formation of the B-O-V layer structure, which provides a thermally stable surface dipole and an NEA surface.

(In collaboration with Tianyin Sun, Joseph Shammas, Manpuneet Kaur, Mei Hao, Robert J. Nemanich)

5.2 Introduction

A number of wide band gap semiconductors (diamond, boron nitride, aluminum nitride, etc.) have attracted research interest for electron emission applications because of their abilities to exhibit a low or negative electron affinity (NEA). For NEA materials, the vacuum level lies below the conduction band minimum (CBM). Electrons can leave an NEA surface without encountering a barrier, leading to a strong emissivity.

In the case of diamond, a wide band gap material with E_G ~5.5 eV, an NEA can be readily achieved with hydrogen-termination. [1-3] Recently, nitrogen- and phosphorus-doped NEA diamond films have shown a low effective work function, enabling thermionic electron emission at or below 500ºC, which leads to promising applications in thermionic and photon-enhanced thermionic energy conversion devices. [4, 6] Cubic boron nitride (c-BN) has a wide band gap of ~ 6.1-6.4 eV, [7-9] is isoelectronic to diamond, and owns similar properties to various aspects of diamond. The hydrogen-terminated c-BN surface has also been reported to exhibit an NEA. [9-12] Our group has successfully employed plasma-enhanced chemical vapor deposition (PECVD) with fluorine chemistry to prepare c-BN films, which could serve as an alternative material for energy-related applications. [9]

For thermionic energy converters (TECs), a high operation temperature is desired for high conversion efficiency, yet desorption of hydrogen from the diamond and c-BN surfaces at temperatures above 800°C has limited the performance of TECs based on these NEA materials. [3,11,12] In addition, the hydrogen-termination surface is more easily destroyed by annealing in the air, or with an oxygen plasma or other oxidation processes. [13-15] It is therefore worthwhile to investigate alternative surface termination approaches

for providing a more thermally stable NEA. Metal oxides have been reported to induce an NEA on materials such as GaAs [16] and diamond. [17-20] Recently, theoretical and experimental studies have indicated that transition metal oxides are stable and can significantly influence the electronic properties of diamond. [21] However, there have been few reports of experimental results of similar effects on c-BN. Vanadium oxide (VO_2) is a narrow band gap material (Eg=0.7 eV). [22] For metal oxide coatings with the same electron affinity, a smaller band gap will more likely lead to an effective NEA. And for small band gap materials such as VO_2, the electrons emitted from c-BN can be transmitted through real states, instead of tunneling through in-gap states. Vanadium oxides have also attracted interest for their moderate temperature insulator-to-metal transition (IMT), [23, 24] and are considered for applications in electronic and optoelectronic devices. We have obtained preliminary results indicating that vanadium-oxide-termination of boron-doped diamond surfaces exhibit an NEA. [25] These results have motivated us to investigate how the vanadium-oxide-termination changes the electron affinity of the c-BN surface where we have employed *in-situ* photoelectron spectroscopy to establish the electronic properties of the surfaces after various processing steps.

5.3 Experiment

The vanadium-oxide-termination was achieved with two approaches. One was to deposit a thin layer of vanadium metal on the c-BN film, which was followed by an oxygen plasma process to oxidize the film. Samples obtained from this approach are labeled as BN-1. The second method involved terminating the c-BN films with oxygen

first, and then depositing the vanadium layer. Samples processed in this way are labeled as BN-2 and BN-3.

The experiments were accomplished *in situ* in an integrated ultrahigh vacuum (UHV) system which was maintained at a base pressure of ~1×10^{-9} Torr. In this UHV system, different processing and characterization chambers are connected by a ~20 m long linear transfer line. The systems utilized in the experiments were as follows: an electron cyclotron resonance (ECR) PECVD system for deposition of the c-BN films, a reactive electron beam deposition system for deposition of the vanadium films, a remote oxygen plasma system for oxidation of the vanadium layers and the c-BN surfaces, an X-ray photoelectron spectroscopy (XPS) system for core level analysis, and an ultraviolet photoelectron spectroscopy (UPS) system for characterization of the electronic structure of the sample.

The c-BN films were prepared in the ECR-PECVD system employing fluorine chemistry. [9] The substrates were 25 mm diameter, heavily phosphorus-doped ([P]>10^{19} cm^{-3}), single side polished silicon (100) wafers. Before deposition the sample underwent a 15 min *in-situ* plasma cleaning process at 780 °C, which employed a He-Ar-N_2 gas mixture, with flow rates of 35, 2.5 and 12.5 standard cubic centimeters per minute (sccm) respectively, a microwave input of 1.4 kW, and an applied bias of -60 V. The deposition process was initiated by introducing H_2 and BF_3 at flow rates of 1 and 4 sccm respectively, into the He-Ar-N_2 gas mixture with the same parameters of bias, temperature and input power. The deposition process lasted for approximately 4 hours and resulted in BN films of ~0.1 μm thick.

The vanadium films were deposited using a reactive electron beam deposition system, with vanadium metal of 99.8% purity and an alumina crucible. Vanadium films with thickness of ~0.1 nm for samples BN-1 and BN-2, or ~0.5 nm for BN-3, were deposited on the c-BN sample at ambient temperature and an oxygen chamber pressure of $\sim 1\times10^{-7}$ Torr. A growth rate of ~0.01 nm/s was obtained, which was monitored and maintained by a quartz crystal microbalance (QCM).

Oxidation of the metal layer and formation of the O-termination on c-BN films were achieved using an oxygen plasma treatment. The remote plasma was generated by 30W of RF excitation with the sample at ambient temperature. The 100 mTorr oxygen pressure was maintained with a gas flow rate of 30 sccm. The oxidation process lasted for ~1 min.

In order to remove excess oxygen from the sample surface, a 30 min 650°C UHV annealing process was initiated using a tungsten irradiation heater coil beneath the sample holder. The temperature of the sample was controlled by a thermocouple positioned behind the center of the sample, and calibrated with a Mikron M90Q infrared pyrometer.

After each processing step, samples were characterized by *in-situ* XPS and UPS. The XPS analysis was performed using the 1486.6 eV Al Kα line of a VG XR3E2 dual anode source (Mg and Al) and a VG microtech Clam II analyzer. The analyzer was operated at a pass energy of 20 eV and a resolution of ~ 1.0 eV. The binding energy position of the core levels can be further resolved to ~ ±0.1 eV by curve fitting the core level peaks. The XPS was calibrated with a standard gold foil, by aligning the Au 4f7/2 peak to 84.0 eV.

The UPS spectra were obtained using a system equipped with a VSW HA50 hemispherical analyzer and VSW HAC300 controller, operated at a pass energy of 15 eV, giving a resolution of ~0.15 eV. The photon source was optimized for He I radiation (hν=21.2 eV), which is generated from a He discharge lamp operated at ~ 600 V with a discharge current of 200 mA. An -8.0 V bias was applied to the substrate to overcome the work function of the analyzer. To avoid photo-induced charging, the samples were heated to ~280 °C, which was controlled by a thermocouple behind the sample. The UPS system was calibrated against a gold foil, and the Fermi level was regarded as the reference energy.

5.4 Results

5.4.1 Cubic BN with O-termination

As a control experiment, a c-BN film deposited under the same conditions was treated with an oxygen plasma and annealed at 650 °C. XPS and UPS results from the control experiment are shown in Fig. 5.1. Gaussian curve fitting was employed to determine the positions of the XPS peaks. After oxygen plasma treatment, the O 1s signal increased significantly, indicating the c-BN surface had adsorbed oxygen. The B 1s peak shifted 0.6 eV towards lower binding energy, from 191.6±0.1 eV to 191.0±0.1 eV, while the N 1s core level shifted from 399.1±0.1 eV to 398.6±0.1 eV. The shift of the N 1s peak corresponded to the shift of the B 1s peak within the resolution of the XPS system. The 30 min 650°C annealing process restored the B and N 1s core levels to the positions before oxidation. After annealing, the O 1s peak shifted 0.7 eV to a higher binding energy of 532.9eV, which is consistent with the reported value for B_2O_3. [26]

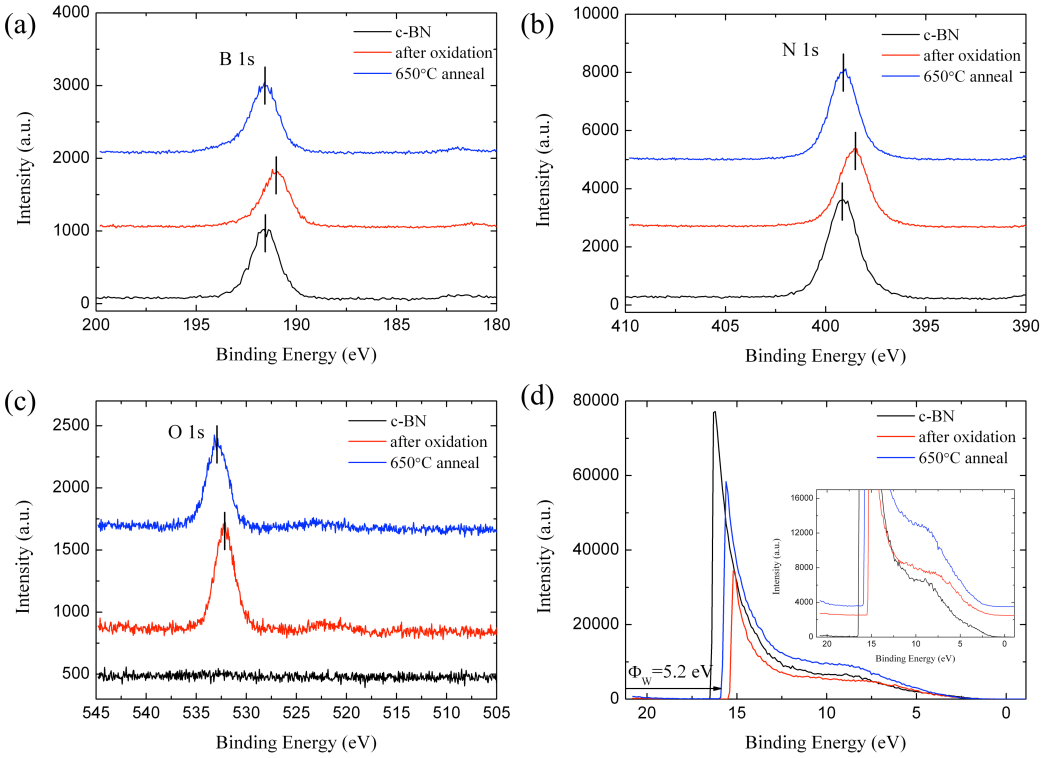

Figure 5.1 (Color online) XPS scans of the O-terminated c-BN sample, showing the (a) B 1s, (b) N 1s, (c) O 1s core level peaks, and (d) the UPS SCANS. The work function variations are indicated in the UPS scans.

The c-BN surface is presumed to be hydrogen-terminated after the ECR-PECVD deposition. [9] The UPS scans of as-grown c-BN showed a 1.7 eV front cutoff and 16.5 eV back cutoff (relative to the Fermi level). With a He I photon energy of 21.2 eV, the CBM position for hydrogen-terminated c-BN was deduced to be 4.7 eV. The sum of the CBM 4.7±0.15 eV and valence band maximum (VBM) 1.7±0.15 eV relative to the Fermi level is ~ 6.4±0.2 eV, which is within the reported range of the c-BN band gap. This result indicates that the as-grown c-BN likely exhibited an NEA. The oxidation process increased the c-BN work function to 5.7 eV, and the VBM shifted to 2.5 eV below the

Fermi level. The spectral width is ~14.8 eV, indicating that O-terminated c-BN exhibits a PEA [27]. While the annealing process was able to reduce the work function to a lower value of ~5.2 eV, combined with the VBM position which is at 2.4 eV, the results still suggest that the c-BN exhibits a PEA before and after annealing. By applying the same band gap of 6.4 eV, a PEA of 1.2±0.2 eV was deduced for the O-terminated c-BN films.

The measured binding energies of the B 1s, N 1s, O 1s core levels, the work function and the VBM for the O-terminated c-BN film are summarized in Table 5.1.

TABLE 5.1 B 1s, N 1s, O 1s core levels, effective work function (Φ_W) and VBM for O-terminated c-BN relative to the Fermi level, in eV.

Process	B 1s	N 1s	O 1s	Φw	VBM
H-termination	191.6	399.1	—	4.7	1.7
Oxidation	191.0	398.6	532.2	5.7	2.5
650°C annealing	191.6	399.1	532.9	5.2	2.4

5.4.2 BN-1

XPS and UPS scans after each preparation step for sample BN-1 are shown in Fig. 5.2. The deposition of vanadium films on the c-BN surface did not lead to a change in the positions of the B and N core levels. After vanadium deposition, the V $2p_{3/2}$ core level could be clearly observed at a binding energy of 516.4 eV, indicating that a vanadium layer was successfully formed on the c-BN surface. A small amount of oxygen was incorporated during vanadium deposition due to the oxygen background in the chamber, which is more significant for the very thin layer deposition. After plasma oxidation, the B

1s peak shifted 0.7 eV towards lower binding energy, and the N 1s peak exhibited a similar shift. Compared with O-terminated c-BN, the vanadium deposition and oxidation appeared to affect the B and N core levels differently from the V core level. The V $2p_{3/2}$ core level shifted 1.1 eV to higher binding energy, while the O 1s peak was observed at a lower binding energy of 531.4 eV, resulting in a reduction of ~1.7 eV in the V-O binding energy difference. The annealing process restored the B and N peaks to the original positions. The vanadium peak was determined to be at 516.9 eV, and the binding energy of the O 1s core level increased by 1.3 eV to 532.7 eV, resulting in a ~1.9 eV increase of the V-O binding energy difference.

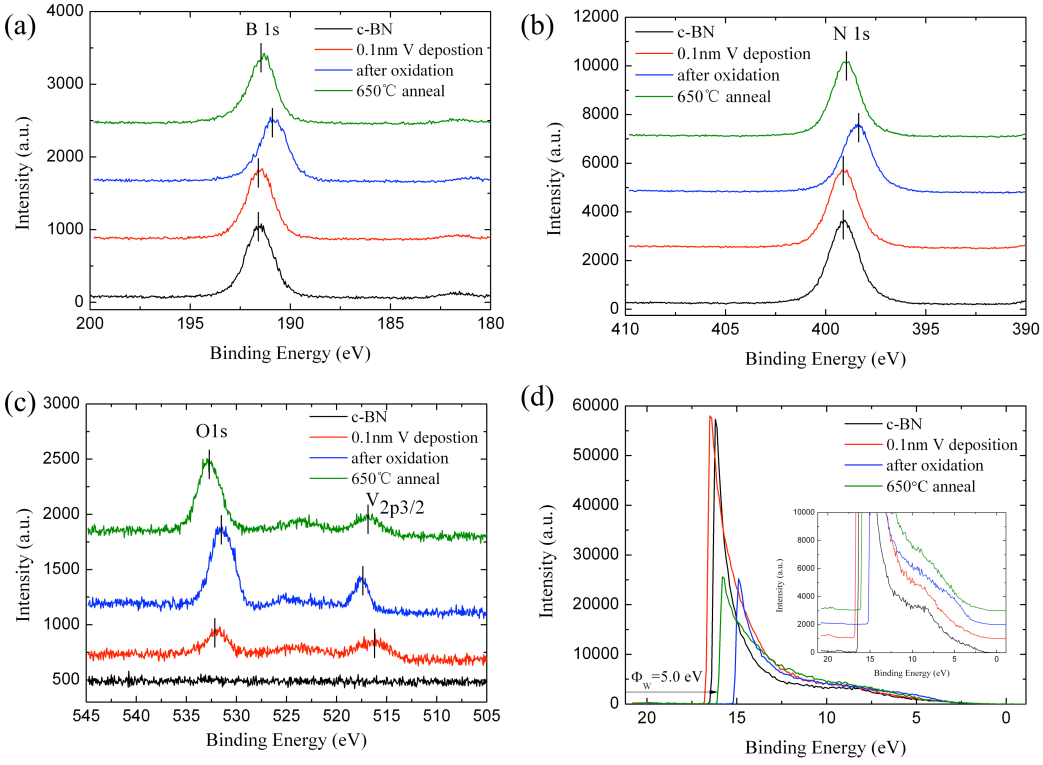

Figure 5.2 (Color online) XPS scans of the BN-1 sample, showing the (a) B 1s, (b) N 1s, (c) O 1s core level peaks, and (d) the UPS scans.

After the vanadium deposition, the back cutoff of the spectrum was at 16.8 eV. Combined with the photon energy of 21.2 eV, the work function of the surface corresponded to the work function of vanadium (Φ_W=4.3 eV [28]) or the work function of V_2O_3 (Φ_W=4.4 eV [29]) within the experimental uncertainty. An oxygen plasma treatment has been reported to increase the work function of diamond surfaces. [30] This was also observed in this experiment. The back cutoff of the UV-photoemission spectra shifted 1.6 eV to lower binding energy after exposure to an O-plasma, corresponding to an increase of the work function. Annealing at 650°C in UHV reduced the surface work function by ~ 1.0 eV. With the band gap of ~6.1-6.4 eV for c-BN, the spectral width, which is ~15.1 eV, implies that BN-1 exhibits an NEA [27].

The measured binding energies of the B 1s, N 1s, O 1s and V $2p_{3/2}$ core levels, the work function and the VBM of BN-1 are summarized in Table 5.2.

TABLE 5.2 B 1s, N 1s O 1s, V $2p_{3/2}$ core levels, effective work function (Φ_W) and VBM for BN-1 relative to the Fermi level, in eV.

Process	B 1s	N 1s	O 1s	V $2p_{3/2}$	Φw	VBM
H-termination	191.5	399.1	—	—	4.7	1.6
Vanadium depostion	191.5	399.1	532.0	516.4	4.4	1.8
Oxidation	190.8	398.4	531.4	517.5	6.0	1.1
650°C annealing	191.4	399.0	532.7	516.9	5.0	1.0

5.4.3 BN-2

Spectroscopic results from sample BN-2 are shown in Fig. 5.3. After oxidation, the B and N 1s core levels were observed to shift towards lower binding energy by 0.4 eV. The deposition of the vanadium layer restored the positions of the B and N 1s peaks, and significantly reduced the work function from 6.2 eV to 4.5 eV. Similar to sample BN-1, thermal annealing changed the binding energy difference between the V and O core levels, indicating a change in the vanadium-oxide bonding. The final position of the O 1s is the same as that of BN-1, while the final binding energy of the V $2p_{3/2}$ core level is 0.3 eV higher. The UPS spectral width is ~15.2 eV, indicating that BN-2 exhibits an NEA [27]. The measured binding energies of the B 1s, N 1s, O 1s and V $2p_{3/2}$ core levels, the work function and the VBM for BN-2 are summarized in Table 5.3.

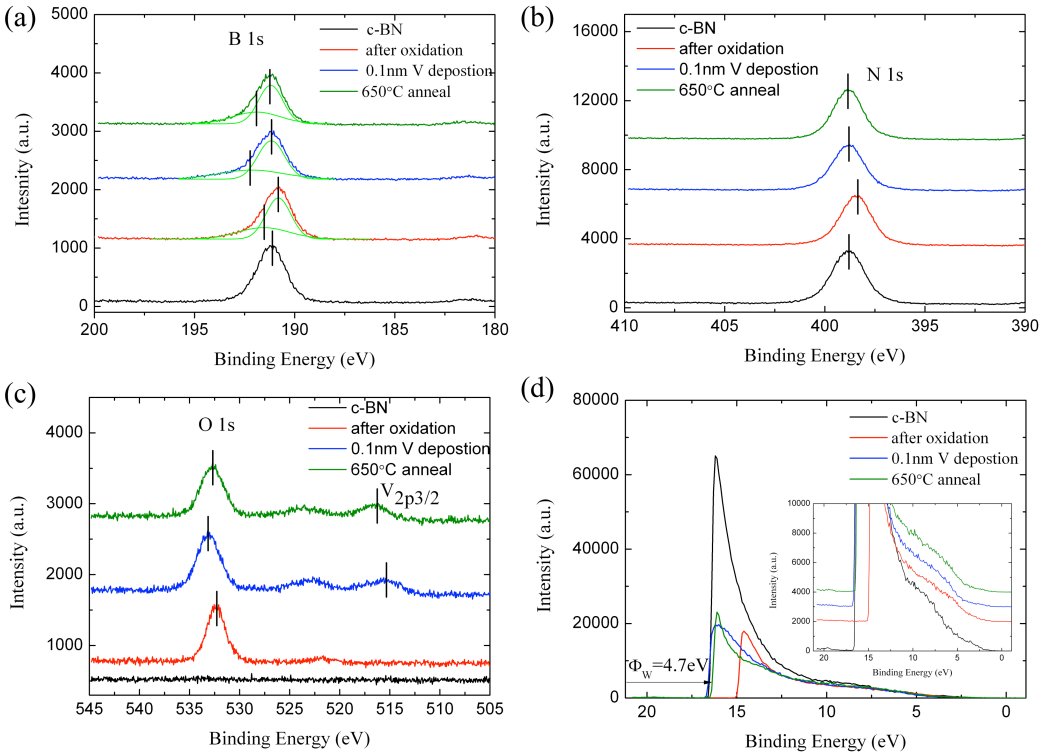

Figure 5.3 (Color online) XPS scans of BN-2, showing the (a) B 1s, (b) N 1s, (c) O 1s and V $2p_{3/2}$ core level peaks, and (d) the UPS scans.

TABLE 5.3 B 1s, N 1s O 1s, V $2p_{3/2}$ core levels, effective work function (Φ_W) and VBM for BN-2 relative to the Fermi level, in eV.

Process	B 1s	N 1s	O 1s	V $2p_{3/2}$	Φw	VBM
H-termination	191.2	398.8	—	—	4.6	1.5
Oxidation	190.8	398.4	532.3	—	6.2	1.8
Vanadium depostion	191.2	398.8	533.1	515.7	4.5	1.1
650°C annealing	191.2	398.8	532.7	516.6	4.7	1.3

5.4.4 BN-3

Spectroscopic results from sample BN-3 are shown in Fig. 5.4. Compared with BN-2, a thicker 0.5 nm vanadium film was deposited on O-terminated c-BN and compared with BN-2. After annealing, the V $2p_{3/2}$ peaks were detected with stronger intensity at 513.2 eV and 515.3 eV. Observing the V $2p_{3/2}$ core level at 515.3 eV has been suggested to indicate V_2O_3 [31]. Moreover, 513.2 eV corresponds to the core level of metallic vanadium, indicating there was excess vanadium that was not fully involved in forming V-O bonds. The O 1s peak was detected at 531.4 eV, 1.3 eV lower than that in samples BN-1 and BN-2, implying a larger contribution of vanadium oxide to the oxides on the c-BN surface compared with BN-1 and BN-2. In addition, the back cutoff of the UPS spectrum was at the same position as sample BN-2. However, the front cutoff was at the position of the Fermi level, within the experimental uncertainty, indicating metallic surface character, which is attributed to either metallic vanadium or the metallic phase of V_2O_3. The measured binding energies of the B 1s, N 1s, O 1s and V $2p_{3/2}$, core levels, the work function and the VBM for BN-3 are summarized in Table 5.4.

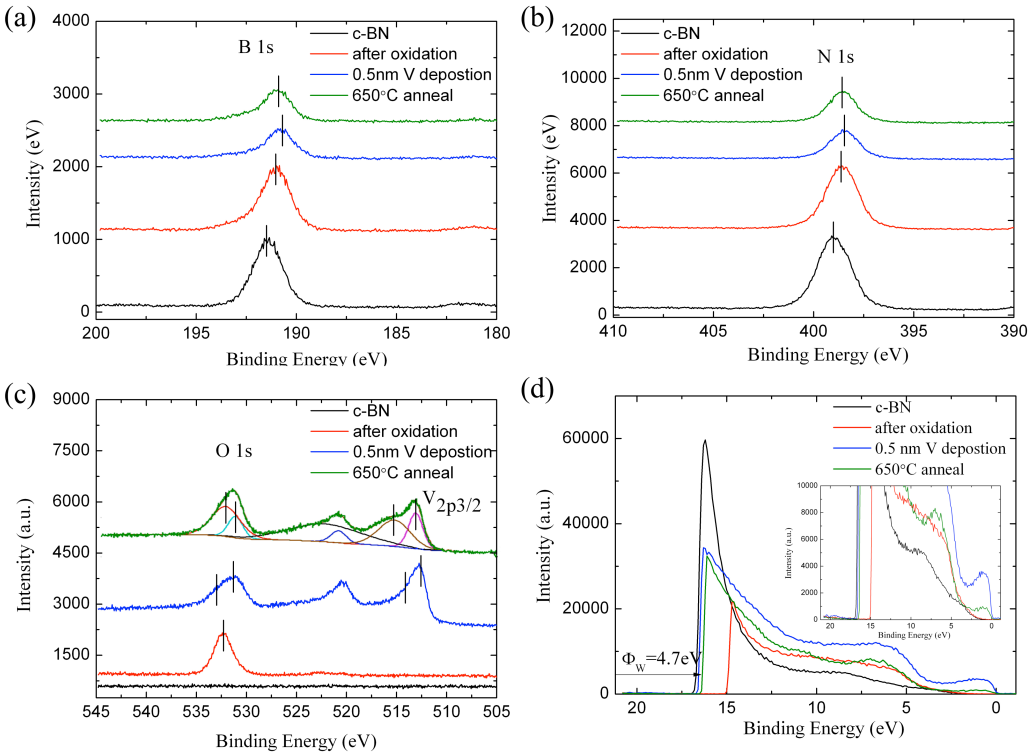

Figure 5.4 (Color online) XPS scans of BN-3, showing the (a) B 1s, (b) N 1s, (c) O 1s and V $2p_{3/2}$ core level peaks, and (d) the UPS scans.

TABLE 5.4 B 1s, N 1s O 1s, V $2p_{3/2}$ core levels, effective work function (Φ_W) and VBM for BN-3 relative to the Fermi level, in eV.

Process	B 1s	N 1s	O 1s	V $2p_{3/2}$	Φw	VBM
H-termination	191.4	399.0	--	--	4.3	1.8
Oxidation	191.0	398.6	532.5	--	6.1	1.9
Vanadium depostion	190.8	398.5	531.5/534.0	512.7/514.1	4.5	-0.2
650°C annealing	190.9	398.6	531.4/533.0	513.2/515.3	4.7	-0.1

5.5 Discussion

5.5.1 Surface and Interface Composition

Previous research indicated that boron nitride films synthesized by ECR-PECVD employing fluorine chemistry are composed of hexagonal boron nitride (h-BN) near the substrate and c-BN on the surface [32]. An absence of a π-plasmon peak in the XPS B 1s and N 1s spectra indicates that h-BN is not detected and c-BN predominates at the sample surface.

It is necessary to determine the specific atoms bonded to oxygen, after oxidation of the c-BN films. In Fig. 5.3(a) a shoulder is observed at 193.2 eV near the B 1s core level main peak, which is close to the B 1s core level in B_2O_3 [31]. Additionally, the O 1s peak is located at 532.7 eV, which is close to the reported binding energy of B-O bands [31]. In contrast, no distinguishable N-O shoulder was evident around the N 1s main peak after the oxygen plasma process. The surface B:N atomic ratios can be estimated from an XPS stoichiometry analysis. In this case, the B:N atomic ratio can be approximately calculated using the following equation:

$$B{:}N\ atomic\ ratio = \frac{I_B/S_B}{I_N/S_N}, \qquad (5.1)$$

where I_B and I_N are the integrated intensities of the B 1s and N 1s peaks from Fig. 5.3(a) and 5.3(b). The S_B and S_N are the atomic sensitivity factors for the B 1s and N 1s peaks, which are 0.159 and 0.477, respectively [33]. The B:N atomic ratio of the surface increased ~4% after oxidation, indicating that nitrogen atoms were removed during the oxidation process. Therefore, the oxygen atoms tended to bond with boron to form B-O bonds at the c-BN surface.

The amount of vanadium covering the surface of the sample is estimated from the XPS spectra using following equation: [34]

$$\Theta_V = \frac{I_V}{S_V} / \left(\frac{I_B}{S_B} + \frac{I_N}{S_N}\right) * \sum_{n=0}^{\infty} exp\left[\frac{-n*d_{BN}}{\lambda_{BN}*cos(\varphi)}\right], \qquad (5.2)$$

where Θ_V, the coverage in monolayers (ML), is the number of absorbed V atoms per unit area (atoms/cm^2) divided by the number of B and N atoms per unit area (atoms/cm^2) on the surface. I_V, I_B and I_N are the integrated intensities of the V $2p_{3/2}$, B 1s and N 1s peaks from Fig. 5.1(c). The S_V, S_B and S_N are the atomic sensitivity factors for the V $2p_{3/2}$, B 1s and N 1s photoelectrons; d_{BN} is the average spacing between *c*-BN planes, which is 1.28 Å, where we assume polycrystalline c-BN surface is comprised of <100>, <110>, and <111> planes; $\lambda_{BN} \approx 31.6$ Å [9] is the inelastic mean free path of electrons in c-BN, which is approximated by the average of the inelastic mean free paths of B 1s and N 1s electrons; φ is the angle between the normal direction and the XPS energy analyzer, which is 0º for this setup. The vanadium coverage on the c-BN surface was calculated to be ~0.26 ML. The coverage of oxygen on the c-BN surface can be similarly calculated using equation (5.2) and after annealing it was found to be ~3.0 ML.

Here we consider that the oxide on the c-BN samples is composed of B_2O_3 and vanadium oxides. For the BN-1 sample, after annealing, the V $2p_{3/2}$ core level was 516.9 eV, which has been suggested to indicate the presence of VO_2. [31] Here we have taken into account a ~0.8 eV downward band bending that resulted from photo-induced charging. Considering the relative amount of vanadium and oxygen, VO_2 is calculated to contribute ~24% of the oxide on the c-BN surface, and the remaining oxide is B_2O_3. For BN-2, with the same amount of vanadium deposited on the O-terminated c-BN surface, the vanadium coverage was calculated to be ~ 0.39 ML using equation (5.2), and the

oxygen coverage is ~ 3.3 ML. After annealing the V $2p_{3/2}$ core level was 516.6 eV, which indicates VO_2 [31]. The VO_2 accounted for ~31% of the oxide on the c-BN surface. A similar composition of oxides formed on the c-BN surface while controlling the amount of vanadium deposited. It appears that B_2O_3 is always formed regardless of the oxidation process sequence, which may be explained by the lower enthalpy of formation of B_2O_3 (ΔH_{B2O3}=-1273 cal/mol, ΔH_{VO2}=-713 cal/mol).

For BN-3, with 0.5 nm vanadium deposited onto the O-terminated c-BN, after annealing the V $2p_{3/2}$ core level was observed at 515.3 eV, which corresponds to V_2O_3 [31]. In this case, the O 1s peak can be resolved into components for B_2O_3 and V_2O_3. The composition of the oxide was estimated by fitting the O 1s peak, which is shown in Fig. 5.4(c). The V_2O_3 accounted for ~26% of the oxide on the c-BN surface. The vanadium film was not completely oxidized. However, consistent with results of BN-1 and BN-2, a fraction (~30%) of sites with V-O-termination is apparently sufficient to change the electron affinity of the surface.

5.5.2 Plasma and Annealing Effects

The results indicate a decrease in binding energy of the core levels after oxygen plasma treatment, which suggests upward band bending. It is likely that the oxygen plasma process introduces a concentration of defects or interstitial oxygen atoms, which act as electron traps or acceptors. A prior study on transition-metal oxides (TiO_2, ZrO_2, HfO_2) suggested that oxygen can diffuse into the transition metal oxide layer during plasma processing, and the excess oxygen can be removed by vacuum annealing to ~550 °C. [35] These defects are compensated by ionized impurities or defects in the c-BN

films, resulting in a negatively charged layer in the oxide and a positively charged layer in the c-BN. This dipole layer results in an outward directed electrical field, which leads to upward band bending.

Annealing is apparently able to eliminate this kind of upward band bending presumably by removing the defects or interstitial oxygen atoms in the oxide. Since the oxide layer is at the surface, the O 1s peak is expected to shift more than the B 1s and N 1s peaks. For example, in O-terminated c-BN, the B and N core levels shifted ~0.6 eV to lower binding energy after oxygen plasma treatment. Annealing restored the B and N 1s peaks, while the O 1s peak shifted ~0.7 eV in the same direction.

5.5.3 Electronic properties

Two models, namely the interface barrier model and the surface dipole model, have been suggested to describe the mechanism of inducing an NEA by metal or metal oxide thin films. [36, 37] The band schematics of the two models are shown in Fig. 5.5. For the interface barrier model, if the c-BN surface is coated with a thin layer of metal or metal oxide, the vacuum level for this thin layer will effectively describe the electron affinity and potentially enable electron emission into vacuum. If the vacuum level of the surface oxide layer lies beneath the CBM of c-BN, an NEA is achieved on the surface. The surface dipole model considers that the metal-oxide bonds at the c-BN surface form a layer of dipoles that creates a surface electrical field. If the dipole is directed away from the surface, the vacuum level can be shifted to a position lower than the CBM, leading to an NEA.

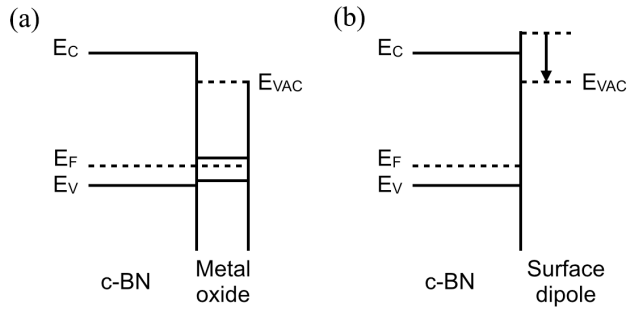

Figure 5.5 Band schematics of the two models: (a) interface barrier model, and (b) surface dipole model.

The vanadium-oxide-terminated c-BN films exhibit an NEA, regardless of the sequence, whether introducing vanadium first followed by oxidization, or vice versa. One possible explanation is that the vanadium-oxide dipoles on the c-BN films act as a metal-oxide layer. The configuration is described by two interfaces, the semiconductor/metal-oxide interface and the metal-oxide/vacuum interface. The thin oxide layer introduces an energy barrier at the oxide/c-BN interface, lowering the electron emission threshold and resulting in an NEA surface condition. The effect of the metal-oxide layer is apparently independent of how this layer is formed. Another possibility is that, in the annealing process, the vanadium and oxygen atoms were activated for diffusion, and structural changes occurred at the surface of c-BN films. The same surface dipole layer could be formed after annealing, leading to a similar state of the surface.

During the oxidation of vanadium, a layer of B_2O_3 is introduced adjoining the c-BN. When the c-BN surface is terminated with B_2O_3, the surface exhibits a PEA. According to the surface dipole model, it appears that the B_2O_3 acts as an acceptor layer on the c-BN surface, and is compensated by a positively charged layer at the c-BN surfaces. This

charge transfer can be explained by the difference of the electronegativities of the two atoms (X_B=2.04, X_O=3.44 [28]). This dipole layer results in an outward electrical field, which shifts the vacuum level to a higher position, leading to a PEA. According to previous studies, hydrogen atoms are mostly involved in N-H bonds, promoting an NEA [9]. Comparing O-terminated c-BN with H-terminated c-BN, the surface dipoles, which determine the electron affinity of c-BN surfaces, changed from N-H to B-O. During the oxidation process, not only the surface termination atoms changed, but also the active surface atoms of the c-BN changed. The change of the surface dipole leads to the change of the electron affinity.

In contrast with O-terminated c-BN, the vanadium-oxide termination leads to an NEA, indicating that the vanadium-oxide layer can act as a donor layer. According to the data of BN-2, the B 1s and N1s core levels of c-BN were not affected by the annealling process. The binding energy is the same as that of H-terminated c-BN, indicating there is essentially no band bending in c-BN introduced by VO_2 and B_2O_3. In this model, the charges are at the interface of B_2O_3 and VO_2. Therefore, VO_2 on a B_2O_3 terminated c-BN surface changes the surface dipole from the O-terminated c-BN. The negative charge in the B_2O_3 layer is not balanced by an ionized layer in c-BN, but by the positive charge in the VO_2 layer. A thin VO_2 layer on the B_2O_3 terminated c-BN surface forms a B-O-V structure, which introduces an inward electric field and results in a reduction of the work function. The changes of the vacuum level due to the surface dipoles are shown in Fig. 5.6 and are similar to the model presented for GaAs surfaces, which showed an effective NEA activated by (Cs, O) layers. [16]

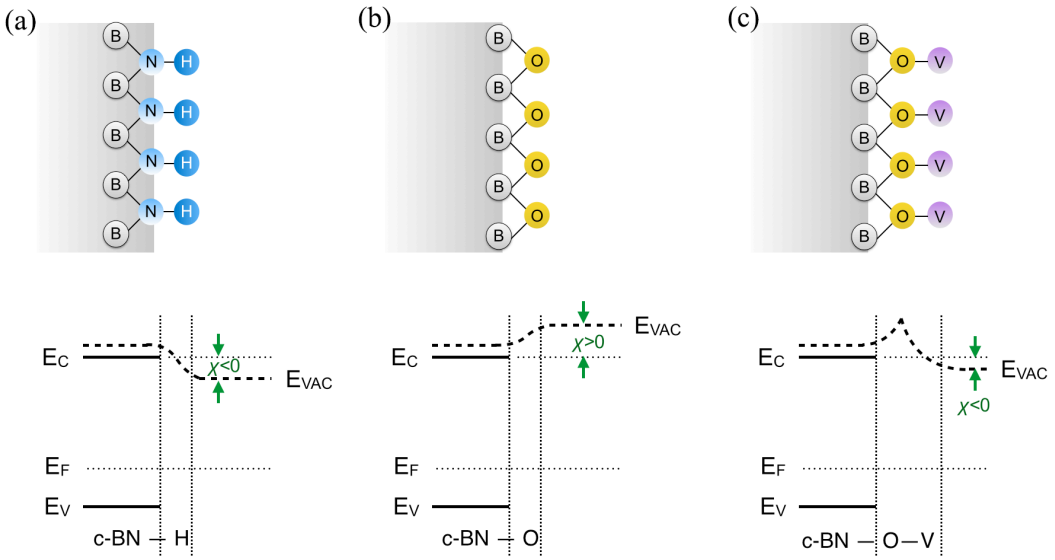

Figure 5.6 (Color online) Schematic diagrams of surface dipoles and corresponding band diagrams for (a) H-terminated c-BN, (b) O-terminated c-BN and (c) vanadium-oxide-terminated c-BN. The changes of the vacuum level due to surface dipoles are profiled.

Although the results presented here establish an NEA for the VO_2 terminated surfaces, the value of the NEA and the value of the work function, which are both important for electron emission, cannot be directly determined from these photoemission measurements. To determine these values it is necessary to locate the position of the vacuum level within the bandgap, but this was not possible in these measurements since emission was not detected from states below the CBM. To approximate the value of the NEA, a reported value of the work function of VO_2, 4.9 eV,[38] is used. Combined with the measured values of the CBM positions, a 0.1 eV NEA on BN-1 and a small PEA ~0.2 eV on BN-2 would be expected. In these two cases, the emission barrier is nearly zero for electrons approaching the surface at the CBM. The discrepancy between the spectral

results and the calculated results may result from the fact that the actual work function of this thin VO_2 layer varies from the reported value due to its very small thickness. The band diagram configurations in the region close to the c-BN surface for O-terminated c-BN, BN-1 and BN-2 are illustrated in Fig. 5.7. The shifts of the position of the Fermi level within the c-BN band gap for the different configurations is attributed to band bending, which occurs in the film beyond the region indicated in the figure.

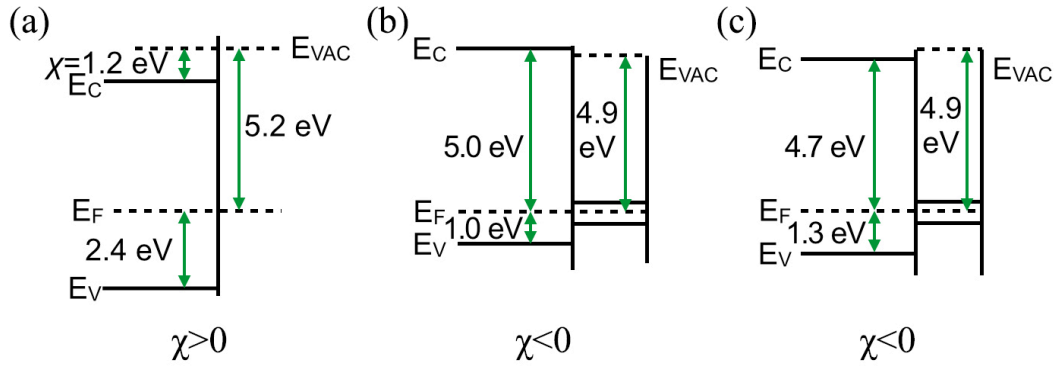

Figure 5.7 Band schematics near the c-BN surface of (a) O-terminated c-BN, (b) BN-1, and (c) BN-2.

5.6 Conclusion

Thin layers of vanadium-oxide were formed on c-BN surfaces, and the resulting electronic structure was examined by *in-situ* XPS and UPS. An NEA was observed on the vanadium-oxide-terminated c-BN sample, while the O-terminated c-BN without vanadium showed a PEA. We propose that the B_2O_3 layer is favorable for the formation of the B-O-V layer structure, which provides a thermally stable surface dipole. The results show that the surface condition (i.e., work function, electron affinity) of c-BN can be modified in a controlled way by careful choice of metal-oxide-termination. The results also indicated that a thermally stable NEA surface on c-BN could be achieved through

vanadium-oxide-termination, which leads to possible applications in energy conversion devices.

Acknowledgment

This work is supported through the Office of Naval Research under Grant # N00014-10-1-0540, and the National Science Foundation under Grant # DMR-1206935.

References

[1] F.J. Himpsel, J.A. Knapp, J.A. VanVechten, and D.E. Eastman, Physics Review B **20**, 624 (1979).

[2] B.B. Pate, Surface Science **165**, 83 (1986).

[3] J. van der Weide, Z. Zhang, P.K. Baumann, M.G. Wensell, J. Bernholc, and R.J. Nemanich, Physics Review B **50**, 5803 (1994).

[4] F.A.M. Koeck, and Robert J. Nemanich, Diamond and Related Materials **18**, 232-234 (2009).

[5] F.A.M. Koeck, R.J. Nemanich, and A. Lazea, K. Haenen, Diamond and Related Materials **18**, 789 (2009).

[6] T. Sun, F.A.M. Koeck, A. Rezikyan, M.M.J. Treacy, and R.J. Nemanich, Physics Review B **90**, 121302(R) (2014).

[7] C.B. Samantaray, and R.N. Singh, International Materials Reviews **50**, 313 (2005).

[8] R.M. Chrenko, Solid State Communication **14**, 511 (1974).

[9] J. Shammas, T. Sun, F.A.M. Koeck, A. Rezikyan, and R.J. Nemanich, Diamond and Related Materials **56**, 13 (2015).

[10] M.J. Powers, M.C. Benhamin, L.M. Porter, R.J. Nemanich, R.F. Davis, J.J Cuomo, G.L. Doll, and S. J. Harris, Applied Physics Letters **67**, 3912 (1995).

[11] K.P. Loh, K. Nishitani-Gamo, I. Sakaguchi, T. Taniguchi, and T. Ando, Applied Physics Letters **72**, 3023 (1998).

[12] K.P. Loh, I. Sakaguchi, M. Nishitani-Gamo, T. Taniguchi, and T. Ando, Diamond and Related Materials **8**, 781 (1999).

[13] M. I. Landstrass, and K.V. Ravi, Applied Physics Letters **55**, 975 (1989).

[14] H. Nakahata, T. Imai, and N. Fujimori, Proceedings of the 2nd International Symposium on Diamond Materials 487 (1991).

[15] S. Ri, C.E. Nebel, D. Takeuchi, B.Rezek, N. Tokuda, S. Yamasaki, and H. Okushi, Diamond and Related Materials **15**, 692(2006).

[16] C.Y. Su, W.E. Spicer, and I. Lindau, Journal of Applied Physics **54**, 1413 (1983).

[17] K.P. Loh, X.N. Xie, S.W. Yang, J.S. Pan, P. Wu, Diamond and Related Materials **11**, 1379 (2002).

[18] C. Bandis, D. Haggerty and B. B. Pate, Materials Research Society Symposia Proceedings (2nd edn.) **339**, 75 (1994).

[19] K.M. O'Donnell, M. T. Edmonds, J. Ristein, A. Tadich, L. Thomsen, Qi-Hui Wu, C. I. Pakes and L. Ley, Advanced Functional Materials **23**, 5608 (2013).

[20] K.M. O'Donnell, T.L. Martin, M.T. Edmonds, A. Tadich, L. Thomsen, J. Ristein, C.I. Pakes, N.A. Fox and L. Ley, Physica Status Solidi A **211**, 2209 (2014).

[21] A.K. Tiwari, J. P. Goss, P. R. Briddon, A. B. Horsfall, N. G. Wright, R. Jones, M. J. Rayson, Europhysics Letters **108**, 46005 (2014).

[22] C.N. Berglund, H. J. Guggenheim, Physical Review **185**, 1022 (1969).

[23] F.J. Morin, Physics Review Letters **3**, 34 (1959).

[24] K. Kosuge, Journal of Physics and Chemistry of Solids **28**, 1613 (1967).

[25] Sun, Tianyin. 2013. *Combined Photo- and Thermionic Electron Emission from Low Work Function Diamond Films*. PhD dissertation, Arizona State University. Ann Arbor: ProQuest/UMI. (Publication No. AAT 3605487.)

[26] X. Gouin., P. Grange, L. Bois, P. L'Haridon, Y. Laurent, Journal of Alloys and Compounds **224**, 22 (1995).

[27] R.J. Nemanich, P.K. Baumann, M.C. Benjamin, S.W. King, J. van der Weide, R.F. Davis, Diamond and Related Materials **5**, 790 (1996).

[28] W.M. Haynes, *CRC Handbook of Chemistry and Physics, 94th edition* (Boca Raton: CRC Press, 2013-2014).

[29] K.E. Smith, V.E. Henrich, Surface Science **225**, 47 (1990).

[30] P.Baumann, R.J. Nemanich, Surface Science **409**, 320 (1998).

[31] S. Surnev, M.G. Ramsey, F.P. Netzer, Progress in Surface Science **73**, 117 (2003).

[32] W.J. Zhang, S. Matsumoto, K. Kurashima, Y. Bando, Diamond and Related Materials **10**, 1881 (2001).

[33] Casa Software Ltd., "CasaXPS Manual 2.3.15 Spectroscopy" (Pressed by Casa Software Ltd.)

[34] V.M. Bermudez, Journal of Applied Physics **80**, 1190 (1996).

[35] C.C. Fulton, G. Lucovsky, R.J. Nemanich, Applied Physics Letters **84**, 580 (2004).

[36] P.K. Baumann, S.P. Bozeman, B.L. Ward, R.J. Nemanich, Diamond and Related Materials **6**, 398 (1997).

[37] K. M. O'Donnell, T. L. Martin, N. A. Fox, and D. Cherns, Physics Review B **82**, 115303 (2010).

[38] C. Zhu, M. Kaur, F. Tang, X. Liu, D.J. Smith, R.J. Nemanich, Journal of Applied Physics **112**, 084105 (2012).

CHAPTER 6

SUMMARY AND FUTURE WORK

6.1 Summary

The research presented in this dissertation focused on using *in situ* photoelectron spectroscopy (PES) to characterize the interface electronic states of dielectrics on ultra wide band gap materials, diamond and c-BN and relate the material properties with interface electronic states. The results can be summarized in three aspects.

Surface conductive diamond was achieved with Al_2O_3 employed as a dielectric layer deposited by plasma enhance atomic layer deposition (PEALD). This configuration was stable during a 500 °C anneal indicating that the diamond/Al_2O_3 interface was more thermally stable compared to the charges trapped in air-induced adsorbates on diamond. The challenge of applying the PEALD process on H-terminated diamond is that the oxygen plasma step is thought to degrade the 2D hole accumulation layer. In this work, it was overcome by a post-deposition hydrogen plasma treatment. The hydrogen plasma treatment significantly affected the surface conductivity of diamond by changing the interface structure and the interface charge state. It may also provide a method to restore damaged regions of the Al_2O_3/diamond interface. The hydrogen plasma and oxygen plasma treatment were found to introduce opposite charges into the dielectric layer. The valence band offset (VBO) between Al_2O_3 and diamond is determined to be 2.7 eV, and the conduction band offset (CBO) is determined to be -1.5 eV. The Al_2O_3 is able to confine holes on surface conductive diamond, enabling a diamond based FET.

By combining two oxides (Al_2O_3 and MoO_3), the hole mobility and concentration of p-type surface conductive diamond were modulated by altering the thickness of the interfacial layer. With an interfacial layer, the distribution of negatively charged states in the oxide was changed. The Al_2O_3 interfacial layer was prepared to increase the distance between the hole accumulation layer and the acceptor layer, and reduce the ionic scattering on the hole accumulation layer, resulting in an increase of hole mobility. The hole concentration and mobility achieved on H-terminated diamond can be changed not only by a selection of material with different work function, but also by using a combination of different oxides. The VBO is found to be 2.6 eV or 3.1 eV for Al_2O_3/H-terminated diamond or MoO_3/diamond, respectively.

A negative electron affinity (NEA) was observed on a vanadium-oxide-terminated c-BN sample, while an O-terminated c-BN surface without vanadium showed a positive electron affinity (PEA). The surface condition (i.e., work function, electron affinity) of c-BN can be modified in a controlled way by careful choice of termination. The B_2O_3 evidently acts as a negatively charged layer introducing a surface dipole directed into the c-BN. Through the interaction of VO_2 with the B_2O_3 layer, a B-O-V layer structure would contribute a dipole between the O and V layers with the positive side facing vacuum. This dipole formed on the c-BN surface, results in a stronger reduction of the work function. The order of vanadium deposition and oxidation process does not change the structure of the surface dipoles after thermal annealing. The lower enthalpy of formation for B_2O_3 is favorable for the formation of the B-O-V layer structure, which provides a thermally stable surface dipole.

In general, the results discussed in this dissertation have involved the interface electronic states and the material related properties of diamond and c-BN. The results demonstrate the potential of ultra wide band gap material leading to applications in high power and high frequency transistor, thermionic emission, and energy conversion devices.

6.2 Future Work

6.2.1 Surface condition enabling surface conductivity

It is considered that the charge transfer in surface conductive diamond is driven by the energy level difference between the diamond VBM and the acceptor level. Therefore, an NEA surface with relatively lower ionization potential will benefit charge transfer. The H-termination is widely used to achieve surface conductivity on diamond and considered to be necessary. Charge transfer doping has not been reported on the O-terminated diamond surface. The electron affinities of diamond with various terminations have been widely investigated. An NEA has been achieved on O-terminated surfaces with various metal oxide termination, such as cesium oxide (Cs-O), [1] oxygenated lithium (Li-O), [2] or titanium monoxide (Ti-O). [3] The role of H-termination in p-type surface conductivity is not fully understood. Also, it is worthy to investigate other surface condition that could enable surface conductivity. Termination with different adhesion properties may favor device fabrication.

6.2.2 Metal-oxide-semiconductor field effect transistors (MOSFETs) based on surface conductive diamond

The surface conductive layer of H-terminated diamond has advantageous properties for the channel of field effect transistors (FETs), such as high breakdown field (10^7 V/cm), high carrier concentration (~10^{13}/cm^2), and shallow carrier profiles (carriers are concentrated less than 10 nm from the surface). [4] A schematic of a circular FET based on surface conductive diamond is shown in Fig. 6.1. The surface conductive layer will be prepared with a diamond/Al_2O_3 structure studied in chapter 3. The source and drain electrodes will be deposited by Ti/Pt/Au to obtain Ohmic contacts and the gate electrode will be formed with Al to obtain Schottky characters. The circular structure is designed to obtain isolation between the source and drain. The gate length will be around 5μm, the gate width will be around 150 μm, and the source-gate and gate-drain spacing will be around 10 μm. The specific value used should be adjusted according to the modeling results. The capacitance-voltage (C-V) and current-voltage (I-V) measurements will be performed to characterize the MOSFET based on H-terminated diamond/Al_2O_3.

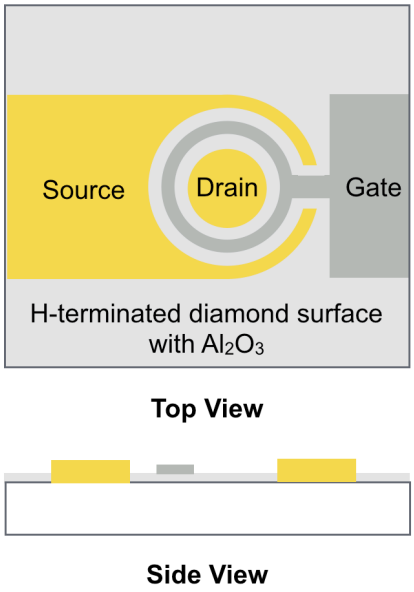

Figure 6.1 Schematic of H-terminated diamond circular surface-channel FET.

6.2.3 Electron affinity of n-type c-BN surface

For an NEA material, the position of the vacuum level is below the conduction band minimum (CBM). Consequently, the effective work function of an NEA material, Φ_W, is defined as the energy difference between its CBM and the Fermi level, instead of that between the vacuum level and Fermi level for the more common positive electron affinity (PEA) materials. Therefore, n-type doping is essential to obtain low effective work function material. N-type c-BN can be achieved by S or Si doping. To obtain high efficient electron emission from c-BN, it is necessary to further investigate the surface condition of n-type c-BN. The electronic properties of S-doped c-BN are not as good as those of Si-doped cBN. [5] Nevertheless, incorporating Si during deposition of c-BN using PECVD or PVD did not result in n-type doped films. [6, 7] An alternative method such as ion implantation should be considered. Then a careful choice of termination should be able to modify the work function and electron affinity of c-BN.

Reference

[1] K.P. Loh, X.N. Xie, S.W. Yang, J.S. Pan, P. Wu, Diamond and Related Materials **11**, 1379 (2002).

[2] K.M. O'Donnell, M. T. Edmonds, J. Ristein, A. Tadich, L. Thomsen, Qi-Hui Wu, C. I. Pakes, and L. Ley, Advanced Functional Materials **23**, 5608 (2013).

[3] C. Bandis, D. Haggerty and B. B. Pate, Mat. Res. Soc. Symp. Proc. (2nd edn.), 339, 75 (1994).

[4] D. Takeuchi, M. Riedel, J. Ristein, and L. Ley, Physics Review B **69**, 125338 (2004).

[5] T. Taniguchi, T. Teraji, S. Koizumi, K. Watanabe, and S. Yamaoka, Japan Journal of Applied Physics **41**, 109 (2002).

[6] J. Shammas, "Characterization of Cubic Boron Nitride Interfaces with *in situ* Photoelectron Spectroscopy, Ph.D dissertation", Arizona State University, 2016.

[7] C. Ronning, A.D. Banks, B.L. McCarson, R. Schlesser, Z. Sitar, and R.F. Davis, Journal of Applied Physics **84**, 5046 (1998).

REFERENCES

W.E. Spicer, Physics Review **112**, 114 (1958).

L.J. Van der Pauw, Philips Research Reports **20**, 220 (1958).

F.J. Morin, Physics Review Letters **3**, 34 (1959).

J. J. Sheer and J. van Laar, Solid State Communications **3**, 189 (1965).

K. Kosuge, Journal of Physics and Chemistry of Solids **28**, 1613 (1967).

A. A. Turnbull and G. B. Evans, Br. Journal of Applied Physics **1**, 155 (1968).

C.N. Berglund, H. J. Guggenheim, Physical Review **185**, 1022 (1969).

G. A. Slack, Journal of Physics and Chemistry of Solids **34**, 321 (1973).

R.M. Chrenko, Solid State Communications **14**, 511 (1974).

F.J. Himpsel, J.A. Knapp, J.A. VanVechten, and D.E. Eastman, Physics Review B **20**, 624 (1979).

C.Y. Su, W.E. Spicer, and I. Lindau, Journal of Applied Physics **54**, 1413 (1983).

C.D. Wagner, Journal of Electron Spectroscopy and Related Phenomena **32**, 99 (1983).

B.B. Pate, Surface Science **165**, 83 (1986).

O. Mishima, J. Tanaka, S. Yamaoka, and O. Fukunaga, Science 238, 181 (1987).

E.A. Kraut, R.W. Grant, J.R. Waldrop, and S.P. Kowalczyk, Heterojunction Band Discontinuities: Physics and Device Applications, edited by F. Capasso and G. Margaritondo (Elsevier, New York, 1987).

M.I. Landstrass, K.V. Ravi, Applied Physics Letters **55**, 975 (1989).

M.I. Landstrass, K.V. Ravi, Applied Physics Letters **55**, 1391 (1989).

N. Fujimori, H. Nakahata, and T. Imai, Japanese Journal of Applied Physics **29**, 824 (1990).

K.E. Smith, V.E. Henrich, Surface Science **225**, 47 (1990).

M.W. Geis, Proceedings of the IEEE **79**, 669 (1991).

H. Nakahata, T. Imai, and N. Fujimori, Proceedings of the 2nd International Symppsium on Diamond Materials 487 (1991).

T. Maki, S. Shikama, M. Komori, Y. Sakaguchi, K. Sakuta, T. Kobayashi, Japanese Journal of Applied Physics **31**, 1446 (1992).

J. van der Weide and R.J. Nemanich, Journal of Vacuum Science & Technology B **10**, 1940 (1992).

T. Tachibana, B.E. Williams, and J.T. Glass, Physics Review B **45**, 11968(1992).

M. Ritala, M. Leskela, E. Nykanen, P. Soinien, and L. Niinisto, Thin Solid Films **225**, 228 (1993).

J. van der Weide, Z. Zhang, P.K. Baumann, M.G. Wensell, J. Bernholc, and R.J. Nemanich, Physics Review B **50**, 5803 (1994).

J. van der Weide and R.J. Nemanich, Physics Review B **49**, 13629 (1994).

C. Bandis, D. Haggerty and B. B. Pate, Material Research Society Symposium Proceedings (2nd edn.), **339**, 75 (1994).

R.S. Gi, T. Mizumasa, Y. Akiba, Y. Hirose, T. Kurosu, M. Iida, Japanese Journal of Applied Physics **34**, 5550 (1995).

M.J. Powers, M.C. Benhamin, L.M. Porter, R.J. Nemanich, R.F. Davis, J.J Cuomo, G.L. Doll, and S. J. Harris, Applied Physics Letters **67**, 3912 (1995).

X. Gouin., P. Grange, L. Bois, P. L'Haridon, Y. Laurent, Journal of Alloys and Compounds **224**, 22 (1995).

K. Hayashi, S. Yamanaka, H. Okushi, K. Kajimura, Applied Physics Letters **68**, 376 (1996).

R.J. Nemanich, P.K. Baumann, M.C. Benjamin, S.W. King, J. van der Weide, R.F. Davis, Diamond and Related Materials **5**, 790 (1996).

V.M. Bermudez, Journal of Applied Physics **80**, 1190 (1996).

J. R. Waldrop and R. W. Grant, Applied Physics Letters **68**, 2879 (1996).

K. Hayashi, S. Yamanaka, H. Watanabe, T. Sekiguchi, H. Okushi, K. Kajimura, Journal of Applied Physics **81**, 744 (1997).

R.S. Gi, T. Ishikawa, S. Tanaka, T. Kimura, Y. Akiba, M. Iida, Japanese Journal of Applied Physics **35**, 2057 (1997).

P.K. Baumann, S.P. Bozeman, B.L. Ward, R.J. Nemanich, Diamond and Related Materials **6**, 398 (1997).

A. Yamada, B.S. Sang, and M. Konagai, Applied Surface Science **112**, 216 (1997).

K.P. Loh, K. Nishitani-Gamo, I. Sakaguchi, T. Taniguchi, and T. Ando, Applied Physics Letters **72**, 3023 (1998).

P.K. Baumann and R.J. Nemanich, Journal of Applied Physics **83**, 2072 (1998).

P.Baumann, R.J. Nemanich, Surface Science **409**, 320 (1998).

C. Ronning, A.D. Banks, B.L. McCarson, R. Schlesser, Z. Sitar, and R.F. Davis, Journal of Applied Physics **84**, 5046 (1998).

R.J. Nemanich, P.K. Baumann, M.C. Benjamin, O. –H Nam, A.T. Sowers, B.L. Ward, H. Ade, and R.F. Davis, Applied Surface Science **130**, 694 (1998).

V.L. Solozhenko, V.Z. Turkevich, and W.B. Holzapfel, Journal of Physical Chemistry B **103**, 2904 (1999).

K.P. Loh, I. Sakaguchi, M. Nishitani-Gamo, T. Taniguchi, and T. Ando, Diamond and Related Materials **8**, 781 (1999).

F. Maier, M. Riedel, B. Mantel, J. Ristein, L. Ley, Physics Review Letters **85**, 3472 (2000).

E.B. Yousfi, J. Fouache, and D. Loncot, Applied Surface Science **153**, 223 (2000).

W. Mönch, Semiconductor Surfaces and Interfaces, 3rd ed. (Springer, Heidelberg, 2001).

W.J. Zhang, S. Matsumoto, K. Kurashima, Y. Bando, Diamond and Related Materials **10**, 1881 (2001).

L.G. Wang, A. Zunger, Physics Review B **66**, 161202 (2002).

T. Taniguchi, T. Teraji, S. Koizumi, K. Watanabe, and S. Yamaoka, Japan Journal of Applied Physics **41**, 109 (2002).

K.P. Loh, X.N. Xie, S.W. Yang, J.S. Pan, P. Wu, Diamond and Related Materials **11**, 1379 (2002).

K. Somogyi, Diamond and Related Materials **11**, 686 (2002).

D. Takeuchi, M. Riedel, J. Ristein, and L. Ley, Physical Review B **68**, 41304 (2003).

S. Surnev, M.G. Ramsey, F.P. Netzer, Progress in Surface Science **73**, 117 (2003).

S. Hüfner, *Photoelectron Spectroscopy: Principles and Applications* (Springer, Berlin, 2003).

M. Riedel, J. Ristein, and L. Ley, Physical Review B **69**, 125338 (2004).

M. Kasu, M. Kubovic, A. Aleksov, N. Teofilov, Y. Taniyasu, R. Sauer, E. Kohn, T. Makimoto, and N. Kobayashi, Diamond and Related Materials **13**, 226 (2004).

D. Takeuchi, M. Riedel, J. Ristein, and L. Ley, Physics Review B **69**, 125338 (2004).

C.C. Fulton, G. Lucovsky, R.J. Nemanich, Applied Physics Letters **84**, 580 (2004).

J.W. Lim and S. Yun, Electrochemical and Solid-State Letters **7**, F45 (2004).

K. Larsson, J. Ristein, Journal of Physical Chemistry B **109**, 10304 (2005).

C.E. Nebel, New Diamond and Frontier Carbon Technology **15**, 5 (2005).

C.B. Samantaray, and R.N. Singh, International Materials Reviews **50**, 313 (2005).

D. Takeuchi, H. Kato, G. S. Ri, T. Yamada, P. R. Vinod, D. Hwang, C. E. Nebel, H. Okushi, and S. Yamasaki, Applied Physics Letters **86**, 152103 (2005).

R.L. Puurunen, Journal of Applied Physics **97**, 121301 (2005).

S. Ri, C.E. Nebel, D. Takeuchi, B.Rezek, N. Tokuda, S. Yamasaki, and H. Okushi, Diamond and Related Materials **15**, 692(2006).

B. Rezek, H. Watanabe, and C. E. Nebel, Applied Physics Letters 88, 042110 (2006).

E. Langereis, M. Creatore, S.B.S. Heil, M.C.M. van de Sanden, and W.M.M. Kessels, Applied Physics Letters **89,** 081915 (2006).

J. Koo, S. Kim, S. Jeon, H. Jeon, Y. Kim, and Y. Wen, Journal of Korean Physical Society **48**, 131 (2006).

K. Hirama, H. Takayanagi, S. Yamauchi, J.H. Yang, H. Kawarada, H. Umezawa, Applied Physics Letters **92**, 112107 (2008).

T. Teraji, S. Koizumi, and Y. Koide, Journal of Applied Physics **104**, 016104 (2008).

F.A.M. Koeck, and Robert J. Nemanich, Diamond and Related Materials **18**, 232-234 (2009).

D. Kueck, P. Leber, A. Schmidt, G. Speranza, and E. Kohn, Diamond and Related Materials **19**, 932 (2010).

K. Hirama, K. Tsuge, S. Sato, T. Tsuno, Y. Jingu, S. Yamauchi, and H. Kawarada, Applied Physics Express **3**, 044001 (2010).

H. Guo, Y. Qi, and X. Li, Journal of Applied Physics **107**, 033722 (2010).

K. M. O'Donnell, T. L. Martin, N. A. Fox, and D. Cherns, Physics Review B **82**, 115303 (2010).

M.T. Edmonds, C.I. Pakes, S. Mammadov, W. Zhang, A. Tadich, J. Ristein, and L. Ley, Applied Physics Letters **98**, 102101 (2011).

S. Tanuma, C.J. Powell, and D.R. Penn, Surface and Interface Analysis **43**, 689 (2011).

K. Hirama, H. Sato, Y. Harada, H. Yamamoto, and M. Kasu, IEEE Electron Device Letters **33**, 1111 (2012).

M. Kasu, H. Sato, and K. Hirama, Appled Physics Express **5**, 025701 (2012).

C. Zhu, M. Kaur, F. Tang, X. Liu, D.J. Smith, R.J. Nemanich, Journal of Applied Physics **112**, 084105 (2012).

S.A.O. Russell, S. Sharabi, A. Tallaire, and D.A.J. Moran, IEEE Electron Device Letters **33**, 1471 (2012).

H. Kawarada, Japanese Journal of Applied Physics **51**, 090111 (2012).

J.W. Liu, M.Y. Liao, M. Imura, and Y. Koide, Applied Physics Letters **101**, 252108 (2012).

J.W. Liu, M.Y. Liao, M. Imura, H. Oosato, E. Watanabe, and Y. Koide, Applied Physics Letters **102**, 112910 (2013).

J.W. Liu, M.Y. Liao, M. Imura, H. Oosato, E. Watanabe, A. Tanaka, H. Iwai, and Y. Koide, Journal of Applied Physics **114**, 84108 (2013).

S.A.O. Russell, L. Cao, D. Qi, A. Tallaire, K.G. Crawford, A.T.S. Wee, and D.A.J. Moran, Applied Physics Letters **103**, 202112 (2013).

K.M. O'Donnell, M. T. Edmonds, J. Ristein, A. Tadich, L. Thomsen, Qi-Hui Wu, C. I. Pakes, and L. Ley, Advanced Functional Materials **23**, 5608 (2013).

H. Sato and M. Kasu, Diamond and Related Materials **31**, 47 (2013).

C. Pietzka, J. Scharpf, M. Fikry, D. Heinz, K. Forghani, T. Meisch, Diemant, R.J. Behm, J. Bernhard, J. Biskupek, U. Kaiser, F. Scholz, and E. Kohn, Journal of Applied Physics **114**, 114503 (2013).

Sun, Tianyin. 2013. *Combined Photo- and Thermionic Electron Emission from Low Work Function Diamond Films*. PhD dissertation, Arizona State University. Ann Arbor: ProQuest/UMI. (Publication No. AAT 3605487.)

W.M. Haynes, *CRC Handbook of Chemistry and Physics, 94th edition* (Boca Raton: CRC Press, 2013-2014).

K.M. O'Donnell, T.L. Martin, M.T. Edmonds, A. Tadich, L. Thomsen, J. Ristein, C.I. Pakes, N.A. Fox and L. Ley, Physica Status Solidi A **211**, 2209 (2014).

A.K. Tiwari, J. P. Goss, P. R. Briddon, A. B. Horsfall, N. G. Wright, R. Jones, M. J. Rayson, Europhysics Letters **108**, 46005 (2014).

A. Daicho, T. Saito, S. Kurihara, A. Hiraiwa, and H. Kawarada, Journal of Applied Physics **115**, 223711 (2014).

Robert J. Nemanich, John A. Carlisle, Atsushi Hirata, and Ken Haenen, MRS Bulletin **39**, 490 (2014).

J. Yang, B.S. Eller, M. Kaur, and R.J. Nemanich, Journal of Vacuum Science & Technology A **32**, 021514 (2014).

T. Sun, F.A.M. Koeck, A. Rezikyan, M.M.J. Treacy, and R.J. Nemanich, Physics Review B **90**, 121302(R) (2014).

W. Zhang, Y.M. Chong, B. He, I. Bello, and S.T. Lee, "3.24 – Cubic Boron Nitride Films: Properties and Applications", In "Comprehensive Hard Materials", edited by V. K. Sarin, Elsevier, Oxford, 2014, Pages 607-639.

J. Shammas, T. Sun, F.A.M. Koeck, A. Rezikyan, and R.J. Nemanich, Diamond and Related Materials **56**, 13 (2015).

Y. Jia, W. Zhu, E.G. Wang, Y. Huo, and Z. Zhang, Physics Review Letters **94**, 086101(2015).

J. Shammas, T. Sun, F.A.M. Koeck, A. Rezikyan, and R.J. Nemanich, Diamond and Related Materials **56**, 13 (2015).

Y. Yang, T. Sun, J. Shammas, M. Kaur, M. Hao, and R.J. Nemanich, Journal of Applied Physics **118**, 165310 (2015).

K.G. Crawford, L. Cao, D. Qi, A. Tallaire, E. Limiti, C. Verona, A.T.S. Wee, and D.A.J. Moran, Applied Physics Letters **108**, 42103 (2016).

C. Verona, W. Ciccognani, S. Colangeli, E. Limiti, M. Marinelli, and G. Verona-Rinati, Journal of Applied Physics **120**, 025104 (2016).

J. Shammas, "Characterization of Cubic Boron Nitride Interfaces with *in situ* Photoelectron Spectroscopy, Ph.D dissertation", Arizona State University, 2016.

Casa Software Ltd., "CasaXPS Manual 2.3.15 Spectroscopy" (Pressed by Casa Software Ltd.)

Y.Yang, F.A. Koeck, M. Dutta, X. Wang, S. Chowdhury, and R.J. Nemanich, Journal of Applied Physcis **122**, 155304 (2017).

J.Y. Tsao, S. Chowdhury, M.A. Hollis, D. Jena, N.M. Johnson, K.A. Jones, R.J. Kaplar, S. Rajan, C.G. Van de Walle, E. Bellotti, C.L. Chua, R. Collazo, M.E. Coltrin, J.A. Cooper, K.R. Evans, S. Graham, T.A. Grotjohn, E.R. Heller, M. Higashiwaki, M.S. Islam, P.W. Juodawlkis, M.A. Khan, A.D. Koehler, J.H. Leach, U.K. Mishra, R.J. Nemanich, R.C.N. Pilawa-Podgurski, J.B. Shealy, Z. Sitar, M.J. Tadjer, A.F.Witulski, M. Wraback, and J.A. Simmons, Advanced Electronic Materials **4**, 1600501 (2018).